

AD-769 343

SOLID SOLUTION SOFTENING (RHENIUM
DUCTILIZING EFFECT AND BUBBLE STRENGTH-
ENING IN TUNGSTEN-RHENIUM ALLOYS

Ronald P. Simpson

Air Force Materials Laboratory
Wright-Patterson Air Force Base, Ohio

September 1973

DISTRIBUTED BY:

NTIS

National Technical Information Service
U. S. DEPARTMENT OF COMMERCE
5285 Port Royal Road, Springfield Va. 22151

Reproduced From
Best Available Copy

AD-769343

UNCLASSIFIED

Security Classification		DOCUMENT CONTROL DATA - R & D	
(Security classification of title, body of abstract and indexing annotation must be entered when the overall report is classified)			
1. ORIGINATING ACTIVITY (Corporate author)		2a. REPORT SECURITY CLASSIFICATION	
Air Force Materials Laboratory Air Force Systems Command Wright-Patterson Air Force Base, Ohio 45433		UNCLASSIFIED	
3. REPORT TITLE		2b. GROUP	
SOLID SOLUTION SOFTENING (RHENIUM DUCTILIZING EFFECT) AND BUBBLE STRENGTHENING IN TUNGSTEN-RHENIUM ALLOYS			
4. DESCRIPTIVE NOTES (Type of report and inclusive dates)			
5. AUTHOR(S) (First name, middle initial, last name)			
Ronald P. Simpson			
6. REPORT DATE		7a. TOTAL NO. OF PAGES	7b. NO. OF REFS
September 1973		153 165	208
8a. CONTRACT OR GRANT NO.		8b. ORIGINATOR'S REPORT NUMBER(S)	
a. PROJECT NO. 7351		AFML-TR-73-235	
c. Task No. 735102		8d. OTHER REPORT NO(S) (Any other numbers that may be assigned this report)	
d.			
10. DISTRIBUTION STATEMENT			
Approved for public release; distribution unlimited.			
11. SUPPLEMENTARY NOTES		12. SPONSORING MILITARY ACTIVITY	
		Air Force Materials Laboratory (LLM) Air Force Systems Command Wright-Patterson AFB, Ohio 45433	
13. ABSTRACT			
<p>The effect of carbon additions to tungsten and tungsten-rhenium alloys was determined by anelastic relaxation, stress relaxation and mechanical property studies. The solid solubility of carbon is too low to allow a significant effect even at high rhenium concentrations. The thermal component of flow stress was determined in electron beam zone refined single crystal tungsten and tungsten-rhenium alloys by strain rate cycling measurements. Rhenium alone, rather than a combination of rhenium and interstitials, lowers the lattice friction stress (Peierls stress) and is responsible for the ductilizing effect in tungsten.</p> <p>Bubbles were identified at grain boundaries of recrystallized, doped tungsten and tungsten-rhenium alloys from scanning electron microscopy studies of intergranular fracture surfaces. Auger electron spectroscopy demonstrated that these bubbles are coated with potassium which is highly localized at grain boundaries. Varying concentrations of rhenium had no noticeable effect on fracture behavior, bubble size or distribution, or potassium segregation. The bubbles dramatically raise recrystallization temperature and control grain growth texture and are, therefore, responsible for the high temperature creep properties of "doped" tungsten and tungsten-rhenium alloys.</p>			
Reproduced by NATIONAL TECHNICAL INFORMATION SERVICE U S Department of Commerce Springfield VA 22151			

DD FORM 1 NOV 63 1473

UNCLASSIFIED
Security Classification

165

UNCLASSIFIED

Security Classification

14.	KEY WORDS	LINK A		LINK B		LINK C	
		ROLE	WT	ROLE	WT	ROLE	WT
	Solid Solution Softening Ductilizing Tungsten Rhenium Dislocation Dynamics Dope Additions Bubble Strengthening						

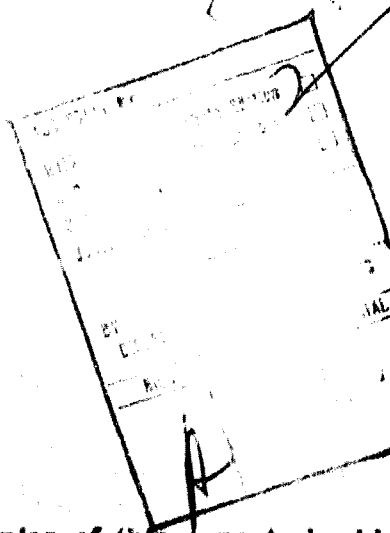
ia

UNCLASSIFIED

Security Classification

NOTICE

When Government drawings, specifications, or other data are used for any purpose other than in connection with a definitely related Government procurement operation, the United States Government thereby incurs no responsibility nor any obligation whatsoever; and the fact that the government may have formulated, furnished, or in any way supplied the said drawings, specifications, or other data, is not to be regarded by implication or otherwise as in any manner licensing the holder or any other person or corporation, or conveying any rights or permission to manufacture, use, or sell any patented invention that may in any way be related thereto.



Copies of this report should not be returned unless return is required by security considerations, contractual obligations, or notice on a specific document.

AIR FORCE/56780/26 October 1973 - 300

**SOLID SOLUTION SOFTENING (RHENIUM DUCTILIZING
EFFECT) AND BUBBLE STRENGTHENING
IN TUNGSTEN-RHENIUM ALLOYS**

RONALD P. SIMPSON, CAPTAIN, USAF

Approved for public release; distribution unlimited

ic

FOREWORD

This report was prepared by the Metals and Ceramics Division, Air Force Materials Laboratory, Air Force Systems Command, under Project 7351, "Metallic Materials," Task 735102, "Welding and Brazing of Metals Components for Military Aerospace Structures and Jet Engine." This research was conducted in the Metals and Processing Branch (AFML/LLM) by Captain Ronald P. Simpson.

This report covers work conducted from 15 October 1969 through 15 October 1972, and was a dissertation presented in partial fulfillment of the requirements for the degree of Doctor of Philosophy at Cornell University, Ithaca, New York. Professor Eraldus Scala was Special Committee Chairman and major advisor and Professor Walter Owen acted as major advisor during Professor Scala's absence. Professors Robert Fay and Lionel Weiss were minor members of the Special Committee and their interest and guidance are appreciated.

The author wishes to express his appreciation to a number of colleagues and friends for providing creative suggestions and comments throughout the course of this investigation. Dr. D. Robert Hay was instrumental in the formulation of the technical approach. In addition, important contributions to the experimental design and analysis of results were received from Dr. T.M.F. Ronald, Dr. J.C. M. Li, Dr. George J. Dooley II, Dr. T.W. Haas, Dr. Harry A. Lipsitt, and Dr. Prakash D. Parikh. Technical assistance was received from many people. Mr. B.F. Addis produced the single crystals, Mr. Bill B. Bowles and Mr. Jim E. Graf conducted the X-ray work, Mr. Russell Pence did the transmission and scanning electron microscopy, Mr. George Gilmore ran the heat treatments, Mr. C.E. Lowe did the photography and Mr. Charles D. Houston provided the chemical analysis. The personal interest and extensive contributions of Mr. Gary L. Teeters and Vincent T. Vidoni are greatly appreciated. Thanks are also due to Mrs Jean Gwinn for the extensive time and interest in typing the manuscript.

This technical report has been reviewed and is approved.



ROGER J. AUSTIN, Major, USAF
Acting Chief, Metals and Processing Branch
Metals and Ceramics Division
Air Force Materials Laboratory

ABSTRACT

The effect of carbon additions to tungsten and tungsten-rhenium alloys was determined by anelastic relaxation, stress relaxation and mechanical property studies. The solid solubility of carbon is too low to allow a significant effect even at high rhenium concentrations. The thermal component of flow stress was determined in electron beam zone refined single crystal tungsten and tungsten-rhenium alloys by strain rate cycling measurements. Rhenium alone, rather than a combination of rhenium and interstitials, lowers the lattice friction stress (Peierls stress) and is responsible for the ductilizing effect in tungsten.

Bubbles were identified at grain boundaries of recrystallized, doped tungsten and tungsten-rhenium alloys from scanning electron microscopy studies of intergranular fracture surfaces. Auger electron spectroscopy demonstrated that these bubbles are coated with potassium which is highly localized at grain boundaries. Varying concentrations of rhenium had no noticeable effect on fracture behavior, bubble size or distribution, or potassium segregation. The bubbles dramatically raise recrystallization temperature and control grain growth texture and are, therefore, responsible for the high temperature creep properties of "doped" tungsten and tungsten-rhenium alloys.

TABLE OF CONTENTS

CHAPTER		PAGE
I.	INTRODUCTION	1
II.	EXPERIMENTAL PROCEDURE	8
	1. Material	8
	2. Carburization	11
	3. Electrochemical Polishing	13
	4. Elastic Aftereffect	13
	5. Stress Relaxation (Dynamic Strain Aging)	15
	6. Metallographic Replication	16
	7. Chemical Analysis	16
	8. Auger Spectroscopy	19
	8.1 Recrystallization Technique	19
	8.2 Experimental Setup	20
	8.3 Auger Operation	20
	8.4 Sputtering	21
	8.5 SEM Fracture Characterization	22
	9. Compression Measurements	22
	9.1 Sample Growth and Preparation	22
	9.2 Microstrain Measurements	23
	9.3 Plastic Strain Rate Determination	26
	9.4 Anelastic Limit	26
	9.5 Strain Rate Cycling	28
	9.6 Thermal Cooling	28
	10. Slip System Determination	29
III.	RESULTS	31
	1. Material Characterization	31
	2. Carburized Alloy Behavior	33
	3. Auger Electron Spectroscopy of Recrystallized Alloy Fracture Surface	52
	4. Scanning Electron Microscopy of Recrystallized Alloy Fracture Surfaces	55
	5. Single Crystal Compression Measurements	65

CHAPTER		PAGE
IV.	DISCUSSION	84
	1. Rhenium Ductilizing Effect	84
	1.1 Role of Carbon (Interstitials)	84
	1.2 Role of Rhenium	90
	1.3 Similarities with Solid Solution Softening	94
	2. Source and Mechanism of Dope Effect	96
	2.1 Auger Electron Spectroscopy	97
	2.2 Scanning Electron Microscopy	99
V.	SUMMARY AND CONCLUSIONS	105
VI.	APPENDIX I	109
VII.	APPENDIX II	130
VIII.	REFERENCES	134

LIST OF TABLES

TABLE		PAGE
I.	Alloys Tested with Analyzed Rhenium Content	10
II.	Chemical Analysis Techniques	17
III.	Periodic Chart Arrangement of Elements Analyzed Chemically	17
IV.	Single Crystals Tested and Test Temperatures	30
V.	Metal Impurity Analysis of Starting Material	49
VI.	Metal Impurity Analysis of Electron Beam Recrystallized Material	50
VII.	Microhardness and Tensile Data	51
VIII.	Rhenium and Potassium Concentrations Before and After Heat Treatments	62
IX.	Average Interstitial Chemical Analysis Before and After Heat Treatments	63
X.	Characteristic Auger Electron Energies (eV) for Tungsten, Rhenium and Potassium	63
XI.	Potassium Coverages of Samples Following Fracture and Argon Ion Bombardment	64
XII.	Single Crystal Orientation and Test Temperature	67
XIII.	Strain Rate Cycling Data	72
XIV.	Effect of Rhenium on Single Crystal Hardness	72
XV.	Alloy Systems Found to Exhibit Solid Solution Softening	95

LIST OF ILLUSTRATIONS

FIGURE		PAGE
1.	Schematic of strain variation with time in a system undergoing a mechanical relaxation.	7
2.	Example tensile and torsion specimen with electrochemically polished gauge length.	14
3.	Extension apparatus for testing in heating or cooling liquid. Also shown is extra grip and typical specimen.	14
4.	Experimental set-up for compression microstrain measurements.	25
5.	Schematic layout of the load-elongation recording arrangement with superimposed timing pulse.	27
6.	Schematic layout of equipment arrangement for low temperature measurements.	27
7.	Photomicrograph of unalloyed tungsten a.) transverse section and b.) longitudinal section at 200X.	36
8.	Photomicrograph of W-1 $\frac{1}{2}$ w/o Re transverse section at 200X.	36
9.	Photomicrograph of W-3w/o Re transverse section at 200X.	36
10.	Photomicrograph of W-10w/o Re transverse section at 200X.	36
11.	Photomicrograph of W-25w/o Re transverse section at 200X.	36
12.	Photomicrograph of W-2w/o Re transverse section at 200X.	37
13.	Photomicrograph of W-2.75w/o Re transverse section at 200X.	37

FIGURE		PAGE
14.	Photomicrograph of W-3w/o Re transverse section at 200X.	37
15.	Photomicrograph of W-3.25w/o Re transverse section at 200X.	37
16.	Photomicrograph of W-5w/o Re transverse section at 200X.	37
17.	Effect of rhenium additions on the hardness of tungsten.	38
18.	Effect of rhenium additions on the yield strength of tungsten.	39
19.	Effect of rhenium additions on the ultimate strength of tungsten.	40
20.	Effect of rhenium additions on the tensile (Young's) modulus of tungsten.	41
21.	Effect of rhenium additions on the tensile ductility of tungsten.	42
22.	Schematic data curve for anelastic relaxation measurements.	43
23.	Schematic data curve representative of all stress relaxation measurements.	43
24.	Photomicrograph of W-3w/o Re after carburization, longitudinal section a.) unrecrystallized, b.) recrystallized grains at 200X.	44
25.	Photomicrograph of W-25w/o Re after carburization, longitudinal section showing crystallographic type precipitates at 200X.	45
26.	Photomicrograph of unalloyed tungsten after carburization a.) transverse section at 90X, b.) longitudinal section before polishing into center region of different structure at 200X, c.) longitudinal section showing center as well as outer microstructure at 200X.	46

FIGURE

PAGE

27. Electron microprobe carbon scan of the unalloyed tungsten microstructure shown in Figure 26c. 47
28. Transmission electron micrograph of carbon replica of polished and etched W-5w/o Re microstructure at 2500X. 48
29. Transmission electron micrograph of fracture surface carbon replica showing extracted precipitate like particles in unalloyed tungsten at 3400X. Electron diffraction identified them as tungsten. 48
30. Auger electron spectra of sample W-3.25w/o Re taken in situ immediately after intergranular fracture at room temperature.
- | | | |
|--------------------------------|---------------------|----|
| Primary electron beam voltage: | 3.0 K eV | |
| Modulating voltage | : 1 eV peak-to-peak | |
| Sample current | : 56 μ A | |
| Amplifier gain | : 100 μ V | |
| Y-axis recorder | : 1/2 V/in | |
| Electron multiplier voltage | : 1300 V | |
| Time constant | : off | 57 |
31. Auger electron spectra of sample W-3.25w/o Re grain boundary fracture surface taken in situ immediately following a 20 minute, 200 μ A current 500 eV ion, argon ion bombardment.
- | | | |
|--------------------------------|---------------------|----|
| Primary electron beam voltage: | 3.0 K eV | |
| Modulating voltage | : 1 eV peak-to-peak | |
| Sample current | : 50 μ A | |
| Amplifier gain | : 100 μ V | |
| Y-axis recorder | : 1/2 V/in | |
| Electron multiplier voltage | : 1300 V | |
| Time constant | : off | 58 |
32. Scanning electron micrograph of etched tungsten wire showing outer wire surface and intergranular fracture surface. 59
33. Scanning electron micrograph of bubbles on the intergranular fracture surface at doped W-3w/o Re. 59

FIGURE		PAGE
34.	Intergranular fracture surface of unalloyed tungsten.	60
35.	Unusually large potassium bubbles on the fracture surface of doped W-3.25w/o Re.	60
36.	Randomly distributed bubbles on the intergranular fracture surface of doped W-5w/o Re.	61
37.	Scanning electron micrograph showing occasional rows of bubbles on the intergranular fracture surface of W-5w/o Re.	61
38.	Orientation of single crystals used in compression measurements grown from: a.) $\langle 100 \rangle$ seed, b.) $\langle 110 \rangle$ seed.	66
39.	Shape change and slip system analysis for compression loaded $\langle 100 \rangle$ and $\langle 110 \rangle$ single crystals.	69
40.	Stress-strain curves for $\langle 100 \rangle$ tungsten crystal at increasing accumulated plastic strain levels.	73
41.	Stress-strain curves for $\langle 100 \rangle$ W-3w/o Re crystal at increasing accumulated plastic strain levels.	74
42.	Strain rate change data plotted according to equation 3.1 to give τ^* and m^* values for $\langle 100 \rangle$ W-1w/o Re.	75
43.	Strain rate change data plotted according to equation 3.1 to give τ^* and m^* values for $\langle 100 \rangle$ W-3w/o Re.	76
44.	Effect of rhenium additions to tungsten on the thermal component of flow stress, τ^* (effective stress).	77
45.	Hardness variations with rhenium additions to tungsten.	78
46.	Effect of rhenium additions to tungsten on the dislocation velocity exponent, m^* .	79

FIGURE		PAGE
47.	Activation volume changes with rhenium additions to tungsten.	80
48.	Variation in effective stress, τ^* , with temperature for $\langle 110 \rangle$ W-1w/o Re.	81
49.	Change in dislocation velocity exponent, m^* , with temperature for $\langle 110 \rangle$ W-1w/o Re.	82
50.	Change in activation volume, V^* , with temperature for $\langle 110 \rangle$ W-1w/o Re.	83
51.	Schematic representation of tetragonal interstitial site distortion from the unstrained condition (a) to the strained condition (b).	86
52.	Schematic representation of flow stress below $0.25 T_m$ for a thermally activated deformation process.	91

INTRODUCTION

Tungsten and its alloys have been the objects of considerable metallurgical interest in the past. In particular, alloying of tungsten with rhenium in varying amounts has found widespread utilization for thermocouples, lamp filaments, electronic applications, welding rods, etc. In virtually all these usages, tungsten is the major alloying constituent and rhenium is added because of its widely known ductilizing effect on materials such as tungsten and molybdenum. The majority of these uses are in high temperature environments where the high melting point and low vapor pressure properties of these alloys can be put to their best usage.

Geach and Hughes first reported that rhenium additions increased the ductility of tungsten and molybdenum in 1955⁽¹⁾.^{*} Their results were confirmed by Jaffee, et al.⁽²⁾ and Savitskii et al.⁽³⁾, and the phenomenon was shown to occur in all the Group VI A metals⁽⁴⁾.

A number of theories resulted from early studies which indicated that rhenium additions caused:

- 1) A change in intergranular oxide morphology and/or composition,
- 2) A reduction in the solubility of interstitial impurities (chiefly oxygen),

* A thorough review of all reported work on the "Rhenium Ductilizing Effect" and its relationship to solid solution softening in bcc alloys is presented in Appendix I.

- 3) A continuous eutectic-like grain boundary phase, accompanied with local rhenium segregation,
- 4) A reduction in the stacking fault energy resulting in easier twinning.

More recent theories consider that:

- 5) Rhenium increases dislocation mobility.

Grain boundary oxide morphology changes are now considered unimportant to the rhenium ductilizing effect since cracks in Group VIA metals are frequently initiated in clean regions of grain boundaries and propagate by intergranular cleavage⁽⁵⁻⁷⁾. In addition, the tendency for intergranular failure increases with rhenium content as demonstrated in tungsten-rhenium by Raffo⁽⁸⁾. A further contradictory observation was made by Allen^(9, 10) who showed that rhenium has no significant effect on surface tension of Group VIA metals.

Numerous studies have shown that rhenium does not decrease interstitial solubility^(7, 9-15) and may even increase it^(14, 15). It is now commonly accepted that rhenium increases interstitial solubility in all Group VIA metals. The occurrence of a grain boundary eutectic-like phase and accompanying local rhenium segregation (listed as item 3) has received little further attention since its early proposal⁽¹⁶⁾. It was observed in all three Group VIA alloys, but only at rhenium concentrations close to the solid solubility limit (Cr-35Re, Mo-35Re, W-25Re), which suggests that a sigma phase formed in the grain boundary of these

alloys and accounted for local chemical and microhardness inhomogeneities. This composition limitation, combined with the lack of any further evidence of the grain boundary eutectic-like phase, also eliminates it as a possible controlling mechanism.

Easier twinning or increased dislocation mobility remain as possible mechanisms for ductilizing. It is well established that rhenium promotes twinning in Group VIA alloys. At high solute concentrations the initial deformation of the ductile alloys is accompanied by twinning at temperatures below $0.25 T_m$ ⁽¹⁷⁾. Stephens and Klopp⁽¹⁸⁾ suggest twinning is important in relieving localized stress concentrations which might otherwise have led to fracture. In their mechanism, twinning arises from a stress-assisted precipitation of sigma phase from a metastable solid solution. The twinning only accounts for a minor fraction of the observed total deformation, usually at the onset of macroscopic strain, with slip accounting for the remainder. Several investigators have observed slip emanating from tips of $1/6 \langle 111 \rangle \{11\bar{2}\}$ twins terminating inside a crystal⁽¹⁹⁻²⁴⁾. The exact affect of twinning is not well understood and its relation to the rhenium ductilizing effect is questionable. With the possible exception of alloys near the solid solubility limit, it seems to be unimportant.

Klopp has shown⁽¹⁷⁾ that the lowered ductile to brittle transition temperature (DBTT) in Group VIA-Re alloys is not specific to rhenium but is also found in alloys with other solutes from Group VIIA and the early portion of Group VIIIA. The ability of a solute to promote the

rhenum ductilizing effect is related to its position in the periodic table. This factor influences the solubility relations, appearance and location of the sigma phase, hardening, twinning, and most likely the improved ductility associated with the rhenum ductilizing effect. The correlation of all these effects reflects the probability that each is controlled by the electronic features of the solute rather than being directly interrelated. It is interesting to note that the rhenum ductilizing effect is limited to Group VIA alloys systems. Both Cb-Re and Ta-Re systems, which contain sigma phases, do not exhibit the rhenum ductilizing effect⁽²⁵⁻²⁷⁾.

Klopp⁽¹⁷⁾ has also suggested that the rhenum ductilizing effect in relatively dilute alloys (up to 10 a/o Re) is a different phenomenon than that of the high rhenum concentrations (above 20 a/o Re). The behavior of the dilute alloys is very similar to the solid solution softening (SSS) found in other bcc transition metal alloy systems. More recently it has been suggested that the increased dislocation mobility causing the rhenum ductilizing effect results from a lowering of the lattice resistance to dislocation motion (Peierls-Nabarro stress)^(8, 17, 18, 28-33). This is consistent with the popular belief that solid solution softening is an intrinsic effect caused by a lowering of the lattice friction stress^(8, 17, 18, 28-41), and that the Peierls stress is dependent on the atomic force-distance relationship which is a function of the alloy electronic configuration. There is some evidence in Group V A alloys, however, that SSS is an extrinsic solute association process⁽⁴²⁻⁴⁸⁾. In these cases softening does not occur when interstitial

impurities are not present. This situation has never been found in iron and the effect of interstitials has not been determined in Group VIA alloys. Early work with Group VIA alloys considered oxygen to be important in the form of oxides, but the effect of oxygen in solution was not considered. Except for Hay⁽⁴⁹⁾ no one has studied the effect of carbon as related to the rhenium ductilizing effect.

One experimental technique used to study interstitial behavior in metals and alloys is internal friction. Generally a torsion pendulum of fixed frequency (1 cps) is used and the sample is cycled through a temperature range of interest. Snoek peaks occur when the interstitial jump frequency is similar to the pendulum frequency causing a maximum in energy damping rate. Complete peak characterization requires cycling 50-100°C either side of the maximum damping range. Internal friction studies of carbon, nitrogen, and oxygen in all Group VA metals have been performed primarily by Powers and Doyle⁽⁵⁰⁻⁵⁷⁾. Carbon solutions of these metals are notable for their instability causing a decline in internal friction peak height with time. This decline is attributed to the precipitation of a carbide second phase. The peak height falls during the course of taking internal friction measurements since this quantity depends on the concentration of carbon in solid solution. As a result of this aging, half-widths cannot be measured with sufficient precision to determine activation energies. Both the instability problem and very low interstitial solid solubility have prevented much use of this technique

with Group VIA metal-interstitial studies, although a few studies have been reported⁽⁵⁸⁻⁶⁰⁾.

An alternate approach is the elastic aftereffect technique where interstitial diffusion distances are drastically lower. In this case anelastic strain results from Snoek ordering of interstitials when a material is held at constant elastic strain long enough for very localized diffusion (one atomic jump). When the stress is removed, the elastic portion of strain is instantly removed while the anelastic portion decreases gradually with time (Figure 1). The rate of anelastic strain reduction at different temperatures allows the calculation of activation energies. If it is assumed that the strain decay is limited by interstitial diffusion then the activation energy is that of diffusion for the particular interstitial element.

In a different vein, Joshi and Stein⁽⁶¹⁾ have suggested that the brittle nature of tungsten is due to segregation of phosphorus to grain boundaries, and the DBTT is related to the concentration of phosphorus. This raises the question of what effect rhenium has on phosphorus morphology or distribution in tungsten. No previous work has been reported on this effect.

The addition of rhenium to tungsten decreases its ductile to brittle transition temperature (DBTT). Although this phenomenon has received considerable attention and extensive experimental data has been accumulated, no completely satisfactory explanation of the effects of rhenium

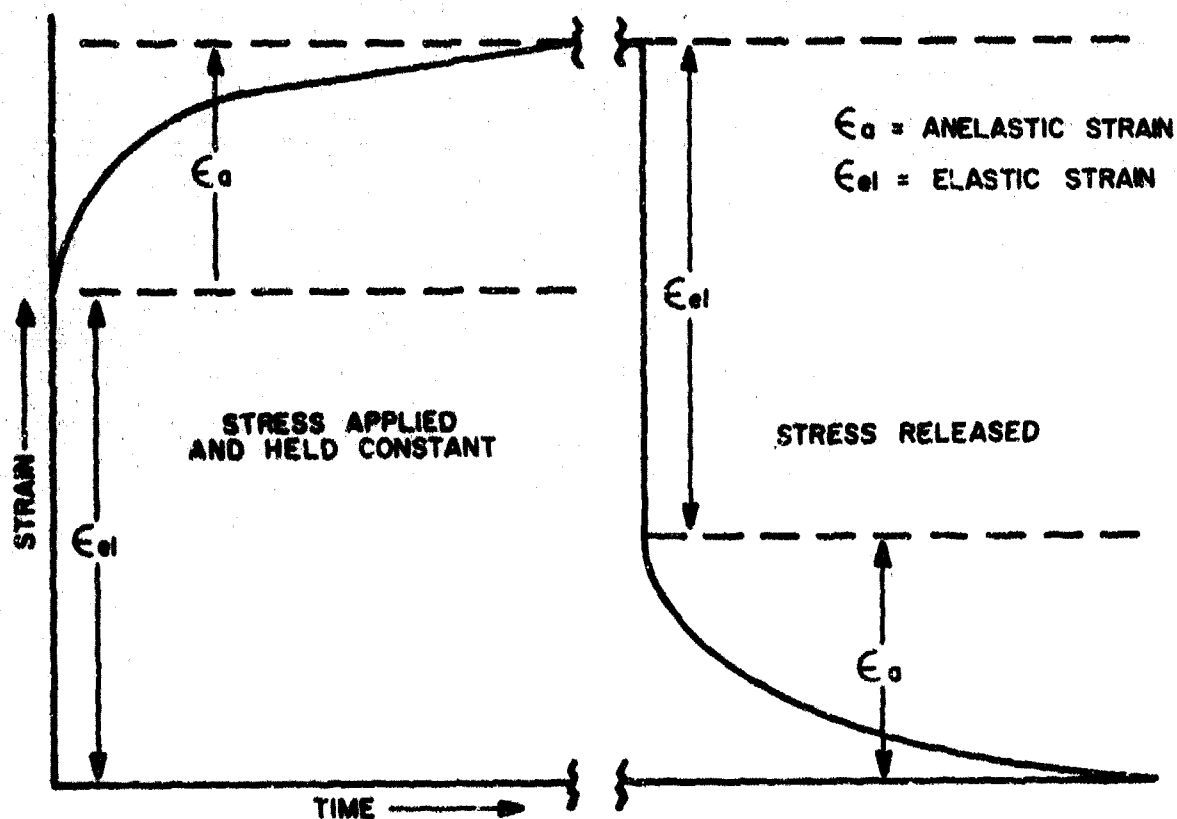


Figure 1. Schematic of strain variation with time in a system undergoing a mechanical relaxation⁽⁵⁰⁾.

in these alloys has yet been obtained. The present investigation examines the effect of rhenium on interstitial behavior, microstructure, plastic deformation and fracture behavior since changes in these properties could affect the DBTT.

EXPERIMENTAL PROCEDURE

It has been proposed that interstitials are related to the ductilizing effect of rhenium additions on tungsten. While the models relating their effect are unsatisfactory, the question of their importance is unresolved. Anelastic relaxation and dynamic strain-aging experiments were performed on carburized tungsten and various tungsten-rhenium alloys to study this interstitial effect. The strain-aging is studied with stress relaxation experiments. The role of interstitials and other impurity elements was further characterized by studying grain boundary chemistry with Auger electron spectroscopy. These results are correlated to fracture behavior with scanning electron microscopy studies. It is also necessary to consider that rhenium alone is responsible for the ductilizing effect. To pursue this possibility and the correlation of the rhenium ductilizing effect with solid solution softening, strain-rate cycling experiments were performed on ultra pure zone refined single crystals of tungsten and tungsten-rhenium. Measurements were made at room temperature and two cryogenic temperatures in compression.

2.1 Material

The tungsten 10 w/o and 25 w/o rhenium alloys used in this investigation were purchased from Cleveland Refractory Metals (CRM). All

other tungsten and tungsten-rhenium material was obtained from Sylvania*, much of it gratis. The polycrystalline material listed in Table I was received as 0.060" diameter drawn rods with a highly elongated grain structure. The unalloyed tungsten (class 1) was commercial welding rod material while the W-1 $\frac{1}{2}$ Re and W-3Re (class 2) were also shelf items. The class of five alloys W-2Re through W-5Re were one time special compositions prepared by Sylvania. The distinction is important since each class of materials (1-4) was prepared from a different master tungsten powder.

Class 1 material had potassium silicate and aluminum oxide dopent compounds added to control grain growth during processing. The compound chemistry, which is proprietary, varied slightly from that used in making lamp grade tungsten powder. The lamp grade dopents control grain growth and morphology during service as well as during processing. Class 2 and class 3 alloys were made from doped lamp grade tungsten powder. The Sylvania alloys are made by mechanically mixing tungsten and rhenium powders. The tungsten powders are doped during the oxide reduction process. The mechanical mixture is cold pressed and sintered by resistive heating at 2800°-3000°C for half an hour. Complete chemical homogenization occurs during the sintering process. The sintered material is hot swaged and drawn to final diameter. The CRM alloys are made by pressing and sintering prealloyed powders made by

* Chemical and Metallurgical Division, G. T. E. Sylvania, Towanda, PA 18848

TABLE I
ALLOYS TESTED WITH ANALYZED RHENIUM CONTENT

Class *	<u>Polycrystalline Rods</u>		<u>Single Crystals **</u>		
	Nominal Composition (Wt % Re)	Analyzed Composition (Wt % Re)	Source	Nominal Composition (Wt % Re)	Analyzed Composition (Wt % Re)
1	Unalloyed W	—	Sylvania	Unalloyed W	<100> — <110> —
2	W-1 Re	1.52	Sylvania	W-1 Re	0.94 0.99
2	W-3 Re	3.18	Sylvania	W-2 Re	1.78 1.60
3	W-2 Re	2.10	Sylvania	W-3 Re	3.10 2.91
3	W-2.75 Re	2.86	Sylvania	W-5 Re	4.61 4.50
3	W-3 Re	3.13	Sylvania	W-9 Re	8.97
3	W-3.25 Re	3.35	Sylvania		
3	W-5 Re	5.13	Sylvania		
4	W-10 Re	10.6	CRM		
4	W-25 Re	26.6	CRM		

* Class 1: Commercial (GTA) welding rod, "undoped" but potassium silicates and aluminum oxides added to restrict grain growth during processing.

Class 2: Commercial alloy rods made with doped tungsten powder.

Class 3: Special processed material for research and evaluation prepared with doped tungsten powder.

Class 4: Commercial alloy rods, no dopants added.

** Single Crystals: Mechanically mixed powders, compressed, sintered and electron beam zone refined with appropriate seed. No dopants were added.

co-reducing tungsten oxide and ammonium perrhenate. These alloys (class 4) are not doped.

A complete metallurgical characterization was performed on each alloy, including chemical analysis, electron and light microscopy, microhardness, and electron diffraction analysis. In addition, room temperature tensile tests were run at a strain rate of 0.005 in/in-min on each alloy. Metallographic samples were polished through 3 μ diamond paste and etched with either Murakami reagent or a slightly diluted acid solution.

Murakami reagent:

10 g potassium ferricyanide
10 g KOH or NaOH
100 ml water

Acid solution:

3 parts HNO₃
3 parts HF
1 part water

In most cases samples were etched and repolished a number of times before final etching to obtain a smooth surface free of any deformed material. The acid etch gives more contrast and in most cases brings out the wrought structure more clearly (as shown for unalloyed tungsten in Figure 7a and b).

2.2 Carburization

Material of each composition was doped with carbon, solution heat treated, and quenched to maximize the carbon in solid solution

Carburizing was performed by back diffusing methane into an evacuated bell jar where the sample was supported on water cooled copper electrodes. Each sample was resistively heated in the methane environment for 15 minutes at 1500°C. The chamber was evacuated and the samples given a homogenization solution treatment at 2000°C for 20 minutes followed by a gas purge quench. They dropped below glowing temperature ($\sim 500^\circ\text{C}$) within 3 seconds. Chemical analysis, metallographic characterization and replication extraction electron diffraction analysis was performed on the carburized materials.

A Brew vacuum quench furnace was also used for solution heat treating and quenching samples. Material was taken to 2600°C (maximum solid solubility temperature for carbon in tungsten) in a vacuum of $1-5 \times 10^{-6}$ torr, held for 15 minutes and quenched into liquid tin at approximately 250°C. Ostermann et al.⁽⁶²⁾ have shown that this provides a considerably faster quenching rate than even a low vapor pressure, water cooled oil bath. In this setup, the liquid tin quench bath has a separate vacuum pumping system and is separated from the tungsten element furnace by a gate valve. The valve is opened and specimens dropped vertically into the liquid tin by means of an externally mounted release mechanism. The tin was chemically removed from the tungsten and tungsten-rhenium alloys in a hot (75°C), agitated, saturated solution of antimony trichloride.

2.3 Electrochemical Polishing

Gauge lengths were electrochemically polished into each 0.060" diameter specimen with a chemical mill. Samples were fixed in a drill chuck mounted on the armature of a small motor. They would turn counterclockwise at a rate close to 20 rpm. An eight inch diameter stainless steel disc, one inch thick, was hollowed out and mounted on a second shaft which turned clockwise around 2 rpm. The 2% NaOH electrolytic solution was contained in a rectangular dish positioned to immerse the bottom of the stainless steel wheel. In this way the wheel was coated with a film of the electrolyte which it carried to the specimen. The anodic sample did not touch the cathodic stainless wheel, but was close enough that a liquid film was supported between them. The potential difference was controlled with a dc power supply to give optimum polishing conditions (2-5 volts). The use of this technique provided a smooth tapered transition from the gauge length area to the grip area and eliminated the problem of localized stress concentrations. A typical specimen is shown in Figure 2.

2.4 Elastic Aftereffect

Carburized, solution treated and gas purge quenched samples were used for elastic aftereffect measurements. Because of the internal friction peak instability problem, particularly with carbon⁽⁵⁰⁾, this technique was used to study the effect of rhenium on carbon interactions in tungsten. An inverted torsion pendulum was designed and constructed

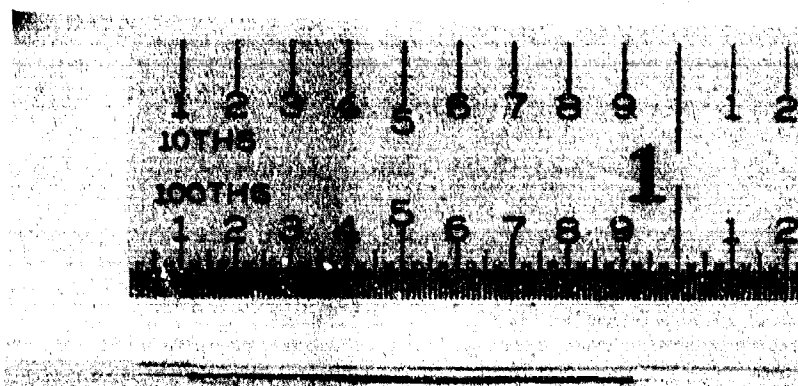


Figure 2. Example tensile and torsion sample with an electrochemically milled gauge length.

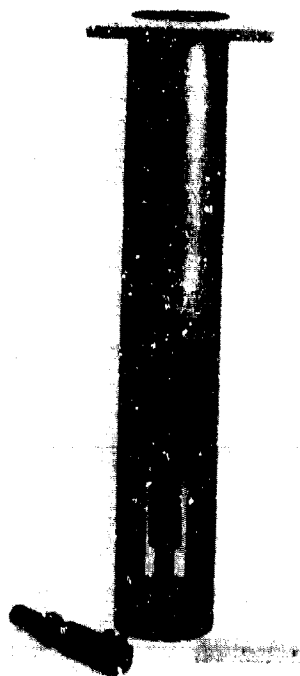


Figure 3. Extension apparatus for testing in heating or cooling liquid. Also shown is extra grip and typical specimen.

that would damp out the elastic portion of strain within 3 seconds. The pendulum was mounted on heavy springs and a thick foam pad to eliminate both low and high frequency vibrations. Strain was measured through a telescope by means of a mirror mounted on the pendulum and could be detected into the 10^{-7} in/in range.

Samples were submerged in a silicon oil bath which eliminated air current problems and provided a means of heating with an immersion resistance heating coil. The oil level remained constant. Once thermal equilibrium was established and overall dimensional stability was excellent. Carburized samples were strained into the 10^{-4} in/in range in torsion and allowed to reach equilibrium at the temperature of interest ($\approx 300^{\circ}\text{C}$). Two symmetrically mounted solenoids were used to provide and maintain torsional strain without bending. The time at temperature varied from 4 to 20 hours. The torsional load was removed, elastic strain damped out, and anelastic decay monitored.

2.5 Stress Relaxation (Dynamic Strain Aging)

Similarly treated material was also used for stress relaxation experiments. These tests were performed with tensile loading in an Instron at elevated temperatures. The apparatus shown in Figure 3 was used with both the inversion torsion pendulum and the Instron. It allowed tensile loading of specimens immersed in hot silicon oil. With the proper exhaust system the oil could be used to obtain temperature up to 300°C .

Stress relaxation was performed by straining the material into the plastic region and stopping the crosshead. The stress relaxes with time as the elastic portion of strain decreases and the plastic portion increases, giving a larger fixed length. Test temperatures were varied between 250°C and 300°C with aging times from a few minutes to three days.

All stress relaxation tests were repeated in a Centorr high temperature vacuum furnace. Temperatures were controlled well within $\pm 1^\circ\text{C}$ in the 300°C to 600°C testing range at pressures of $1-5 \times 10^{-6}$ torr.

2.6 Metallographic Replication

Acetate tape was used to obtain impressions of fracture surfaces. In some cases, the samples were etched before replicating to increase chances of removing carbide precipitates. The tape was shadowed by vapor depositing platinum at a fixed angle and the whole surface was covered with vapor deposited carbon. The tape was dissolved in acetone and the carbon replica placed on a copper grid for examination in a transmission electron microscope. The fracture surface was characterized and electron diffraction patterns were taken and analyzed of all material extracted in the replicas.

2.7 Chemical Analysis

Chemical analysis was performed on each of the polycrystalline alloys. The techniques used for the various elements are listed in Table II. In the combustion technique the sample is turned in a high

TABLE II
CHEMICAL ANALYSIS TECHNIQUES

<u>Element</u>	<u>Technique</u>
C	Combustion
N	Kjeldahl
O	Vacuum Fusion
K and Re	Atomic Absorption Spectroscopy
Metal impurities	Atomic Emission Spectroscopy

TABLE III
PERIODIC CHART ARRANGEMENT OF ELEMENTS
ANALYZED CHEMICALLY

Group													
I	II	III	IV	V	VI	VII	VIII	I	II	III	IV	V	VI
										B	C	N	O
Na	Mg									Al	Si		
K	Ca		Ti	V	Cr	Mn	Fe	Ni	Cu	Zn			
			Zr	Nb	Mo				Ag	Cd		Sn	
			Ta			Re						Pb	

frequency field with oxygen blown on the surface. The metal oxidizes and CO_2 gas evolves. In this case, gas chromatography was used to determine the quantity of CO_2 gas.

The Kjeldahl determination involves dissolving the sample in acid (usually H_2SO_4), and adding NaOH . The NH_3SO_4 formed when the material is dissolved in sulfuric acid breaks down when sodium hydroxide is added, liberating ammonia ($\text{NH}_3 \uparrow$) and steam ($\text{H}_2\text{O} \uparrow$). The gas is introduced to a weak standard acid, usually HCl , which is titrated to a standard pH.

Samples are wrapped in platinum and placed in a graphite container for vacuum fusion oxygen analysis. The reaction gives metal carbide and CO_2 gas, which was analyzed by the volumetric technique.

Atomic absorption is applicable to those elements that can be reduced to unexcited or ground state atoms in a flame. A hollow cathode light source emits the line spectrum of the element to be determined. When this radiation is passed through a vapor containing ground state atoms of that element, the metal atoms absorb at characteristic wavelengths. The degree of absorption is measured photoelectrically and is a measure of the amount of the metal present in the sample.

Emission spectrographic analysis of any material is based on the fact that each element in the vapor state when suitably excited in a flame, arc, spark, or other means, is made to emit its characteristic spectrum. The radiation thus emitted passes into a spectrograph where it is

resolved into its component wavelengths. These spectral lines are a unique property of the atoms and are unaffected by the initial physical state or chemical combination of the atoms. The position and intensity of the lines determine quantitatively the presence and amount of each element. Each element analyzed chemically is listed in the form of a periodic chart in Table III.

2.8 Auger Spectroscopy

Up to this point all experiments described have examined the effect of interstitial carbon in tungsten and tungsten-rhenium alloys on plastic (slip) deformation initiation and propagation. In a parallel effort Auger electron spectroscopy was used to study the fracture surface of all the alloys listed in Table I to establish the effect of interstitials and rhenium on the fracture behavior of tungsten.

2.8.1 Recrystallization Technique

The rods were heat treated to give uniform, equiaxed recrystallized grains. This permitted intergranular fracture and examination of grain boundary surfaces. Two different techniques were used to obtain the same result. In one case, the rods were heated in a tungsten element vacuum furnace (VHT) at 2600°C and 3×10^{-6} torr for 100 hours. The other technique was to heat the samples in an electron beam zone refiner (EBHT) at $2-5 \times 10^{-6}$ torr. The electron beam filament was passed from the bottom to the top of each rod at a rate of 2 inches/hour. Temperature was monitored with an optical pyrometer

and held constant at $2100^{\circ}\text{C} \pm 50^{\circ}\text{C}$.

2.8.2 Experimental Setup

Recrystallized samples were cut into 1-1/4 inch lengths, cleaned with ethyl alcohol and mounted on a multiple sample carousel. This entire specimen assembly was bolted onto a stainless steel, ultra-high vacuum (10^{-10} to 10^{-11} torr) chamber which contained provisions for fracturing in situ. The fracture attachment was manufactured by Physical Electronics Industries.* Samples were suitably positioned for breaking in a groove in the fracture attachment by means of a universal specimen manipulator.

The entire chamber was evacuated with liquid nitrogen cooled zeolite sorption pumps to a pressure of $5-10 \times 10^{-4}$ torr. Noble VacIon† pumps were used from there to achieve ultimate pressures. Once into the 10^{-6} torr range, a surrounding heating mantle was used at 200°C - 250°C to bake out the pump and chamber assembly. Ultimate pressures of 10^{-10} to 10^{-11} torr were reached in around 12 hours.

2.8.3 Auger Operation

All samples were fractured at room temperature and ultimate pressures. Immediately thereafter, the clean fracture surface was rotated in front of the PEI coaxial cylindrical mirror analyzer for examination with Auger electron spectroscopy to excite the Auger

*PEI, Edina, MN.

†Manufactured commercially by Varian Associates, Palo Alto, CA.

transitions within the samples. Improved signal to noise characteristics and relatively high transitions for a given resolution have been ascribed to this type of spectrometer⁽⁶³⁾. Sample currents were of the order of 50 μ amps. Typically 3 Kv beams at normal incidence were used. The operation of these analyzers and the physics of Auger electron spectroscopy are fully described in the literature⁽⁶³⁻⁷²⁾. The analyzer used in this work has the high energy electron gun mounted integrally within the inner cylinder so that the electron beam struck the fracture surface at near normal incidence. The representative Auger spectra were displayed on a conventional x-y recorder.

2.8.4 Sputtering

After the fracture surfaces were examined at 5-6 different positions, they were sputtered with argon to study the composition-depth relationship of the elements appearing on the fracture surface. In this case, pure reagent grade argon gas was introduced into the chamber through a controlled leak valve to a pressure of 5×10^{-5} torr. At the first signs of argon in the chamber, the large VacIon pumps were valved off. A negative 500 V potential was applied to the sample causing the argon ions, produced with a discharge type gun, to be accelerated into it. Typical bombardment times were 10-30 minutes at 50-200 μ amps sample current. After bombardment (sputtering treatments) samples were again rotated and examined with the Auger technique. In some instances, additional sputterings were given to a sample. The entire procedure

was then repeated for the remaining samples on the carrousel.

2.8.5 SEM Fracture Characterization

The fracture surface of each Auger sample was examined in an AMR Model 900 scanning electron microscope* after removal from the vacuum chamber. The fracture mode was characterized and correlated with the material processing history and Auger results. By recrystallizing, the fracture was limited primarily to an intergranular nature and the grain boundary surfaces were studied from 20 X to 20,000 X.

2.9 Compression Measurements

Recent ideas have suggested that the rhenium ductilizing effect is a result of the direct effect of rhenium on the tungsten lattice rather than an interstitial interaction effect. To examine this possibility, dislocation dynamics studies were performed using microstrain and strain rate cycling experiments.

2.9.1 Sample Growth and Preparation

Single crystals of tungsten and tungsten-rhenium were grown from cold pressed rods by electron beam zone refining.† The cold pressed rods were made from tungsten and tungsten-rhenium alloy powders by Sylvania. Both $\langle 100 \rangle$ and $\langle 110 \rangle$ seeds were used for each composition under the following conditions:

* Manufactured by Advanced Metals Research Corporation, 149 Middlesex Turnpike, Burlington, MA 01803.

† All single crystals were grown in the Cornell University Crystal Growth Laboratory.

Vacuum	$2-5 \times 10^{-6}$ torr
Scan rate	4 inches/hr
Number of passes	3 - Two (2) up and one (1) down
Beam current	170 milliamps
Potential	12 KV

Each zone refined rod was analyzed for rhenium content (Table I) and centerless ground, using cuts 0.0005 in. deep, to a uniform diameter. Surface strains were eliminated by chemically removing 0.003" from the diameter in an HF-HNO₃ solution. The chemical polishing was done by rolling the rods in a basin filled with the solution, ensuring that the diameter of the polished rods remains uniform. Orientation was checked with Laue back reflection X-ray pictures. The $\langle 100 \rangle$ crystals were within 2° in all cases but some drift occurred in the $\langle 110 \rangle$ crystals, particularly at the higher rhenium content.

The chemically polished rods were cut into compression specimens with a Micromah wafering machine using a diamond wheel. The ends were lapped flat and parallel within a 0.0002 inch tolerance, and perpendicular to the crystal axis with fine metallographic polishing paper. A length/diameter ratio of 2.2/1 was used for each sample⁽⁷³⁾.

2.9.2 Microstrain Measurements

The compression microstrain equipment was designed and assembled for an earlier investigation⁽³⁸⁾. Excellent resolution of important features of the stress-strain relation in the microstrain

regime was obtained using linear variable differential transformers (LVDT). A key problem in obtaining accurate microstrain measurements involves applying the load parallel to the specimen axis without introducing bending or twist moments to it or the fixturing. The technique used in this study produced microstrain measurements with very low levels of extraneous loading modes.

Microstrain and macrostrain tests were performed with a specially designed apparatus in an Instron, Figure 4. An aluminum centering ring fits over the Instron compression fixture bottom platen. A steel pedestal fits into this centering ring and supports a hardened steel plate with flat ground surfaces. The transducer core is threaded into a large diameter core holder which in turn is threaded into the aluminum centering ring. The large diameter core holder permits fine control in vertical positioning of the core in the transducer coil. A second hardened steel plate is interposed between the upper platen and the specimen. A collar assembly is attached to the upper platen (standard Instron platen) to hold the transducer coil.

The load cell and lower platen assembly are aligned by applying a small load to the hardened steel plates and applying shims to orient the assembly until the faces of the hardened plates are parallel. In this way loading is accomplished with negligible bending or twist moments. Reproducible data are obtained with the aligned compression fixture when the specimen is located on the Instron loading axis and a free,

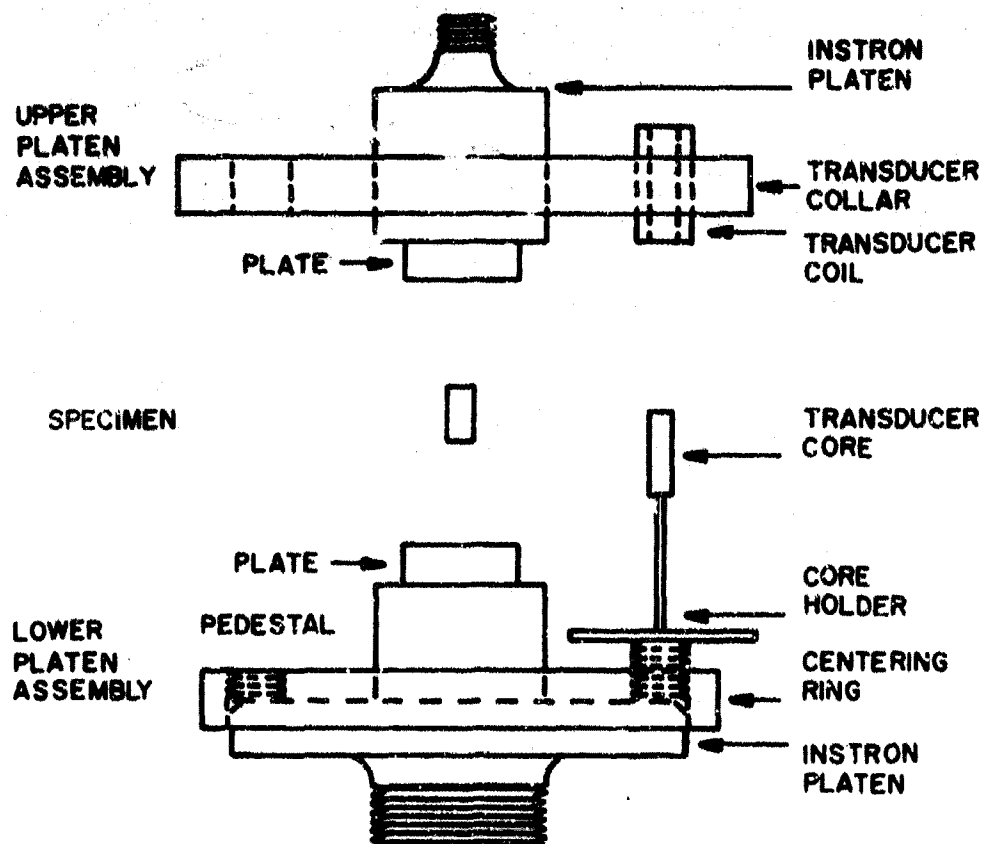


Figure 4. Experimental setup for compression microstrain measurements.

parallel motion of the core exists within the transducer coil. When these conditions are satisfied, the initial part of the curve (elastic) should be linear and retrace itself on unloading at close to Young's modulus. The first deviation from linearity is the precision elastic limit, σ_E .

2.9.3 Plastic Strain Rate Determination

In the microstrain region the true plastic strain rate, $\dot{\epsilon}_p$, is only a fraction of the total strain rate:

$$\dot{\epsilon}_p = \frac{\epsilon_p}{t} = \frac{\epsilon_T - \epsilon_e}{t} \quad (2.1)$$

where ϵ_T is the total strain in time t , and

ϵ_e is the elastic strain in time t .

A timing pulse was superimposed on the load axis to allow calculation of the true plastic strain rate at any point on the deformation curve. This is shown in the schematic layout of the microstrain recording arrangement, Figure 5. The zero-bias system on the load and strain scales permits measurements at high sensitivity. The timing device and the zero-bias system were also used in the strain-rate cycling experiments in the macrostrain region.

2.9.4 Anelastic Limit

The anelastic limit (σ_{my}) was obtained for each sample at six different strain rates. This is the point where the stress-strain curve first deviates from linearity above the precision elastic limit (σ_E).

Strain rate is measured from the superimposed timing pulses. To obtain

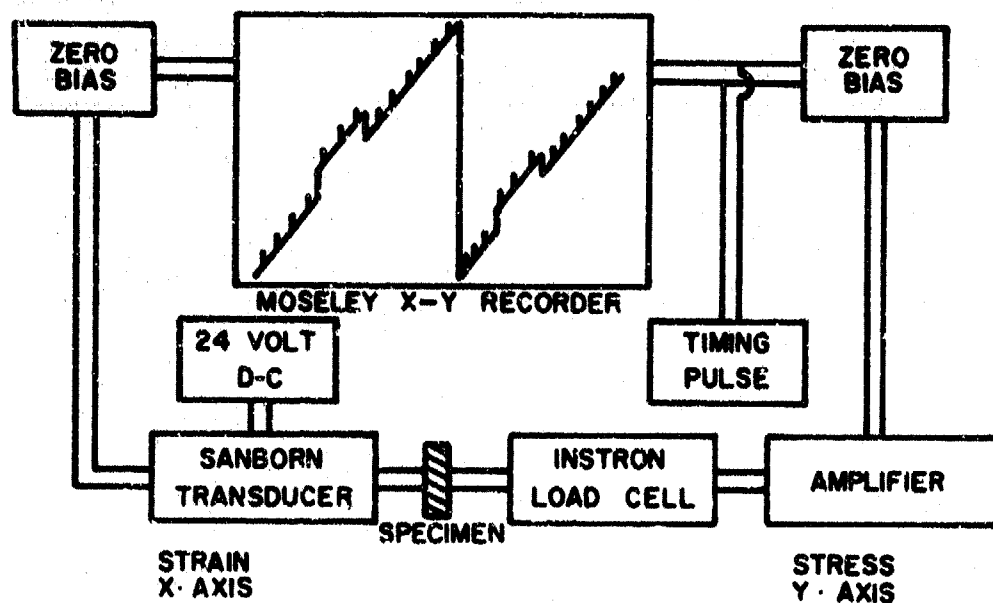


Figure 5. Schematic layout of the recording arrangement. (after Parikh⁽³⁸⁾).

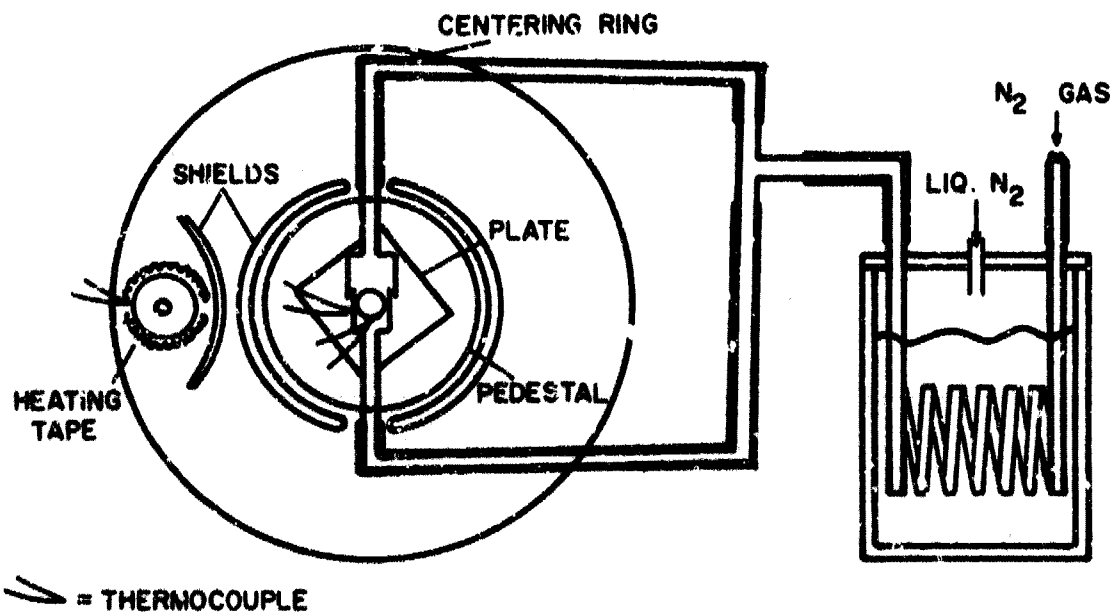


Figure 6. Schematic layout of arrangement for low temperature measurements.

a constant structure for these measurements, each sample was prestrained 2% after determining the precision elastic limit. All anelastic limit tests were run after prestraining.

2.9.5 Strain Rate Cycling

Strain rate cycling experiments were performed in the macrostrain region, after microstrain measurements were completed, for each sample. The Michalak⁽⁷⁴⁾ technique was used with a base crosshead motion of 0.005 inches/minute. The Instron push button electronic control was used to change crosshead speed. This gives strain rate changes that are essentially instantaneous.

2.9.6 Thermal Cooling

Cooling for low temperature measurements was accomplished with the apparatus shown schematically in Figure 6. Nitrogen or helium gas is passed through a copper coil immersed in liquid nitrogen. By varying the gas flow rate, temperatures were varied from room temperature to $\sim 100^\circ\text{K}$. Helium gas was used at the lower temperature since nitrogen partially liquifies and a constant specimen temperature cannot be maintained. Temperature was measured with two thermocouples kept at the bottom and top of each specimen. Metal shields surrounded the specimen and eliminated air currents. The LVDT and load cell were surrounded by heating tapes to maintain constant temperature.

All measurements were made after thermal equilibrium was established in the entire assembly. This condition is accurately determined when a small pre-load on the specimen remains constant. It took 1-2 hours in the 200°K range and 3-4 hours for 100°K temperatures. Specimen thermocouple readings were always constant for some time before the system stabilized. Microstrain measurements, including σ_E and σ_{my} , and macrostrain rate cycling tests were repeated for each composition, with both $\langle 100 \rangle$ and $\langle 110 \rangle$ crystals, at two low temperatures, 200°K and 100°K. A complete list of samples tested is given with actual test temperatures in Table IV.

2.10 Slip System Determination

After deformation each compression sample was carefully examined and characterized for shape changes. Back reflection Laue X-ray procedures were used in conjunction with the shape change observations to determine the operative slip systems. The number and nature of these slip systems were determined for each $\langle 100 \rangle$ and $\langle 110 \rangle$ crystal tested.

TABLE IV
SINGLE CRYSTALS TESTED AND TEST TEMPERATURES

	<u>Room Temp.</u> (°K)		<u>Intermediate Temp.</u> (°K)		<u>Low Temp.</u> (°K)	
	<100>	<110>	<100>	<110>	<100>	<110>
Unalloyed W	295	295	202	198	120	118
W-1 Re	295	295	192	199	120	85
W-2 Re	295	295	190	183	127	140
W-3 Re	295	295	199	194	119	110
W-5 Re	295	295	198	198	119	108
W-9 Re	295	295	199		114	

RESULTS

3.1 Material Characterization

The microstructures of each polycrystalline tungsten-rhenium alloy tested were very similar. Each alloy had been drawn to 0.060 inch diameter and the microstructures were characteristic of this highly worked condition. Typical examples of this structure are presented in Figures 7-16 for each material. With the exception of Figure 7b, all photomicrographs are of transverse sections of the wires. Each alloy is single phase, so the metallographic preparation required considerable care. The light and dark areas are separate grains (not phases) in the microstructure. The grain structure is noticeably smaller in the CRM alloys (W-10Re and W-25Re, Figures 10 and 11) than in the Sylvania material, indicative of greater reductions. These alloys can be worked more because of their higher Re content. The longitudinal photomicrograph for unalloyed tungsten in Figure 7b is typical of all the wrought alloy and shows the severely deformed fibrous grain structure.

Each material tested in this work was characterized chemically. The complete list of elements analyzed is presented in Table III. The results of the emission spectroscopy analysis for metal impurity elements in the as-received polycrystalline rods are given alphabetically in Table V. The interstitial impurity analysis was quite low and uniform for all material. Nitrogen and oxygen were always < 10 ppm

and carbon averaged 24 ± 5 ppm. The results of similar analysis after heat treatment are presented in Table VI for comparison and discussed further in Section 3.3. There is no noticeable difference before and after the heat treatment.

The effect of rhenium additions on the room temperature micro-hardness of tungsten is given in Figure 17. Hardness decreases with increasing rhenium additions up to 5 w/oRe and then increases rapidly with further additions. The yield and fracture stress for these materials similarly reflect the dramatic softening effect of rhenium up to 5 w/oRe, Figures 18 and 19. In addition to affecting the flow stress in tungsten, rhenium has a dramatic effect on the modulus, as shown in Figure 20 for the tensile (Young's) modulus. There is a rapid decrease in Young's modulus up to 5 w/oRe, and a more gradual increase thereafter. Even after the addition of 25 w/oRe, however, it did not return to the value for unalloyed tungsten. The tensile ductility at the same time increases steadily with rhenium content to 10 w/oRe and is unaffected by further alloy additions (Figure 21). The results shown in Figures 17-21 are all presented in Table VII. The tensile behavior (shape of the tensile curve) was similar for each alloy and fracture always occurred at or close to the ultimate tensile strength. With the exception of one W-25Re sample there was never a yield drop. While the upper and lower yield points were classically pronounced in the one sample, this behavior was never reproduced even on samples cut from the same rod.

3.2 Carburized Alloy Behavior

After carburization, chemical analysis showed varying carbon concentrations from 120 ppm up to 1250 ppm. The exact concentration varied with carburization time, temperature, and methane pressure in the chamber, and averaged around 600 ppm to 700 ppm. In every case, however, the quantity of carbon in the samples was increased 10 to 100 times by the carburization treatment to 120 to 1250 ppm.

These relatively large concentrations of carbon never produced any tetragonal lattice distortion. After long exposures at 300°C and 10^{-4} shear strain none of the samples developed any detectable anelastic strain. A schematic example of the elastic-after-affect measurement curves is shown in Figure 22, in contrast to Figure 1 which shows a typical curve when anelastic strain is observed.

Similarly, stress relaxation for extensive time (up to three days) at 300°C never resulted in a yield drop on subsequent reloading. The schematic diagram of Figure 23 shows the type of data curves obtained for all alloys even after quenching into liquid tin from 2600°C. There never was an upper and lower yield point.

Microstructures of carburized samples studied with light microscopy were usually identical to those in Figures 7-16 for the as-received material. In some cases the thermal exposure of carburization caused recrystallization. Figure 24a and b shows longitudinal microstructures of two carburized W-3Re samples that were a.) unrecrystallized and b.) recrystallized. Solution treatment at 2600°C in the Brew quench

furnace always produced a fine equiaxed recrystallized grain structure, usually similar to Figure 24b. In a few unusual cases microstructures similar to Figure 25 were observed. In one exceptional situation a non-homogeneous structure developed after carburization. As the transverse section in Figure 26a shows, the outer diameter microstructure of the wire was quite different than the center (similar to Figure 25). The longitudinal sections in Figures 26b and c show the outer case microstructure and center cross section after further polishing, respectively. The needle-like precipitates found in the case were unusually wide and long. The precipitates in the center of this sample were more representative of most carburized microstructures. Comparison of the central area in Figure 26c with Figure 25 demonstrates this further. Electron microprobe X-ray scan (Figure 27) shows much higher carbon concentrations (at least double) in the outer diameter than the center of this sample, but fails to show significant carbon concentration differences across the acicular precipitates. The experimental sensitivity is good enough to resolve differences between the precipitates and matrix carbon content and leads to the conclusion that they are similar. This may be a result of differences in structure which is discussed further in Chapter 4.

Electron microscopy provided a more detailed carburized microstructure study. Surface replicas of polished and etched metallographic samples revealed structures similar to Figure 28. Attempts to identify these precipitates failed. Numerous extraction replicas were

made and whenever a precipitate-like area gave an electron diffraction pattern it was always analyzed as tungsten. An example of a fracture surface replica with precipitate-like inclusions that turned out to be tungsten is shown in Figure 29.

PHOTOMICROGRAPHS OF AS-RECEIVED POLYCRYSTALLINE RODS

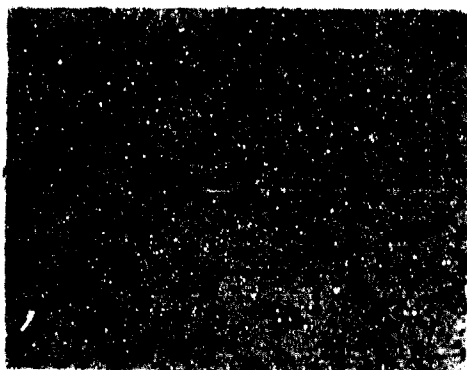


Fig. 7a. Pure tungsten,
transverse section (200X)



Fig. 7b. Pure tungsten,
longitudinal section (200X)

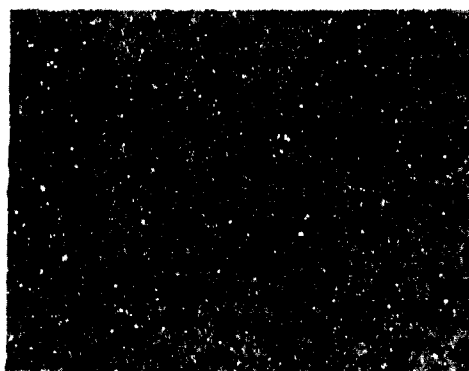


Fig. 8. W-1 $\frac{1}{2}$ w/o Re trans-
verse section (200X)



Fig. 9. W-3w/o Re transverse
section (200X)



Fig. 10. W-10w/o Re trans-
verse section (200X)

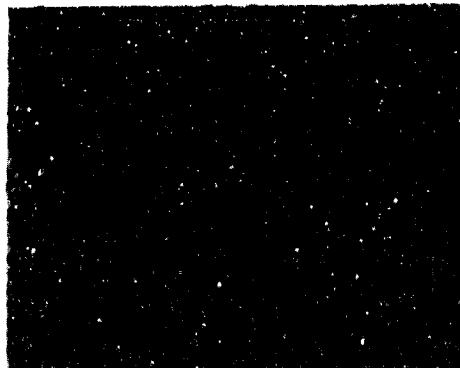


Fig. 11. W-25w/o Re trans-
verse section (200X)

PHOTOMICROGRAPHS OF AS-RECEIVED POLYCRYSTALLINE RODS



Fig. 12. W-2w/oRe transverse section (200X)



Fig. 13. W-2.75w/oRe transverse section (200X)

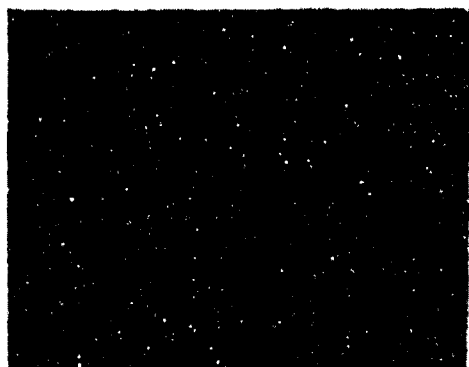


Fig. 14. W-3w/oRe transverse section (200X)

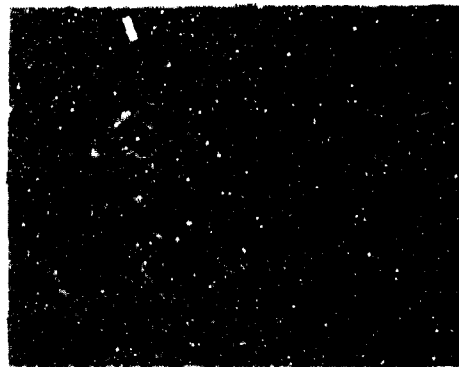


Fig. 15. W-3.25w/oRe transverse section (200X)

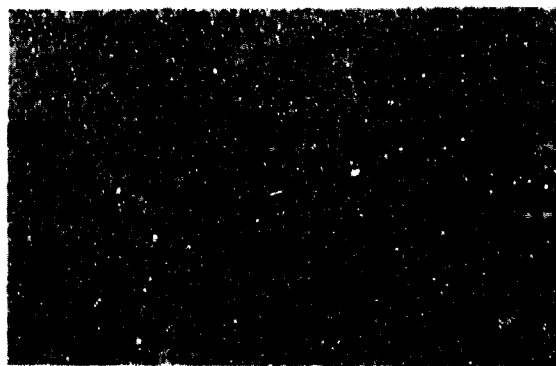


Fig. 16. W-5w/oRe transverse section (200X)

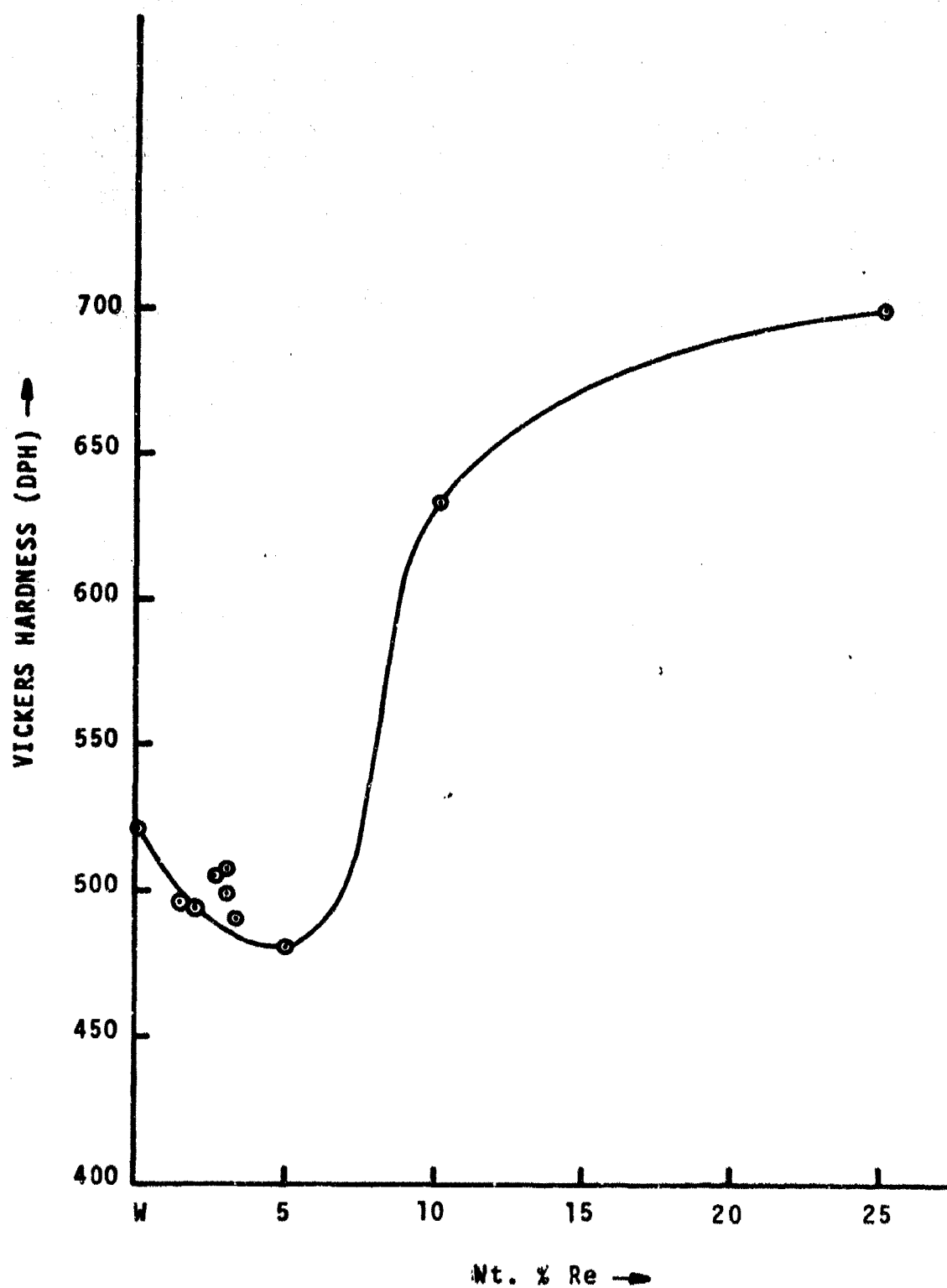


Figure 17. Effect of rhenium additions on the hardness of tungsten.

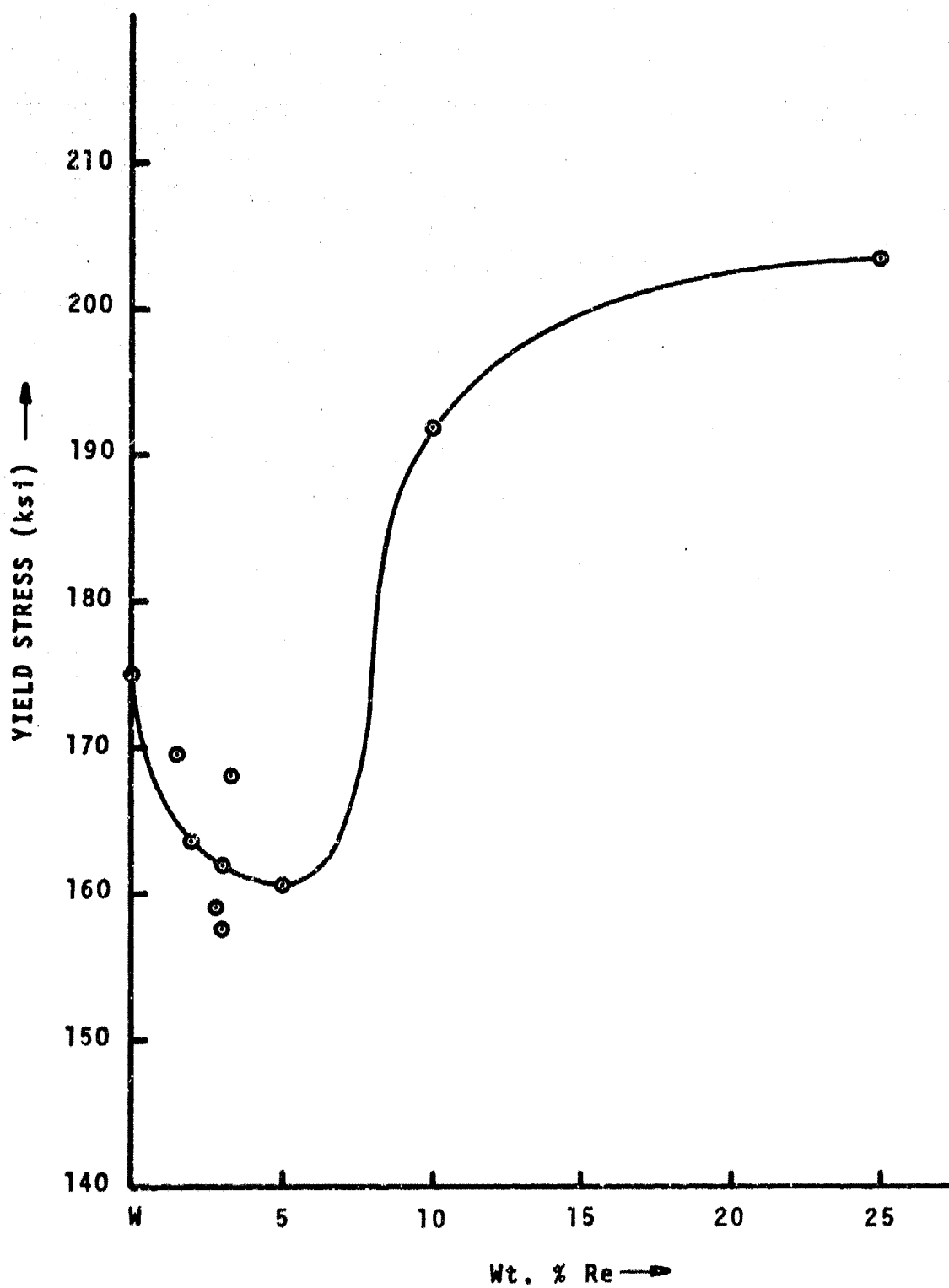


Figure 18. Effect of rhenium additions on the yield strength of tungsten.

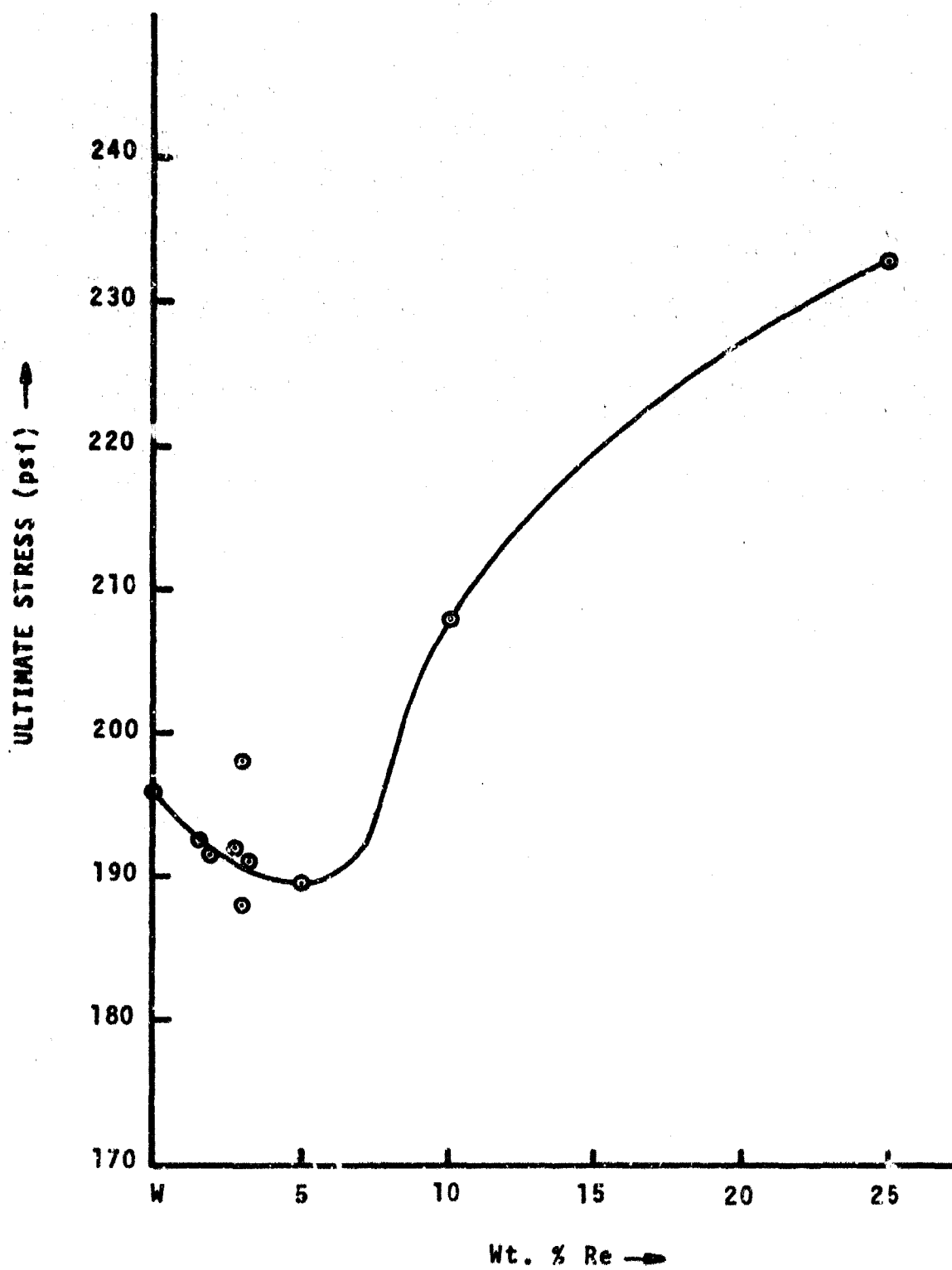


Figure 19. Effect of rhenium additions on the ultimate strength of tungsten.

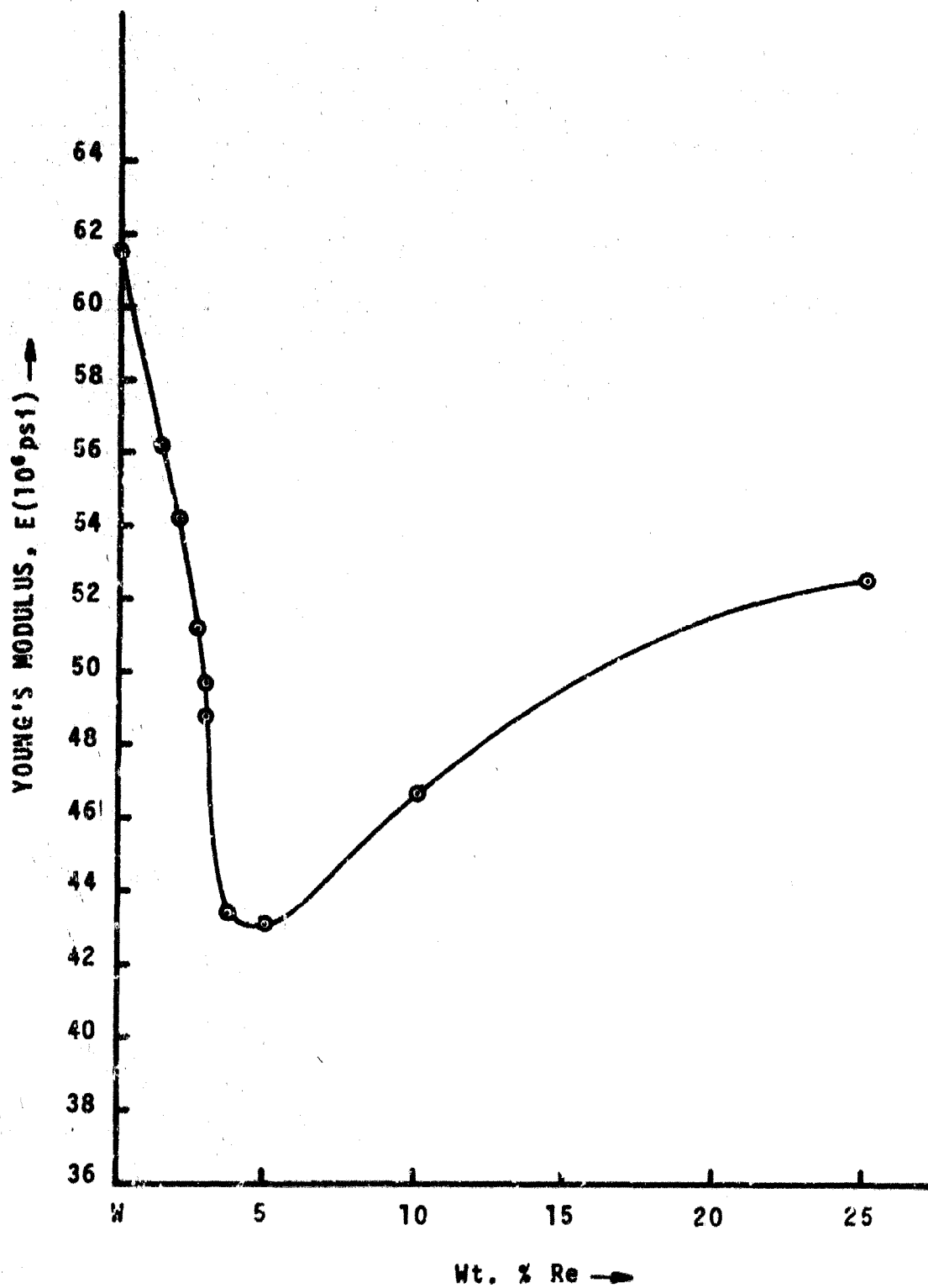


Figure 20. Effect of rhenium additions on the tensile (Young's) modulus of tungsten.

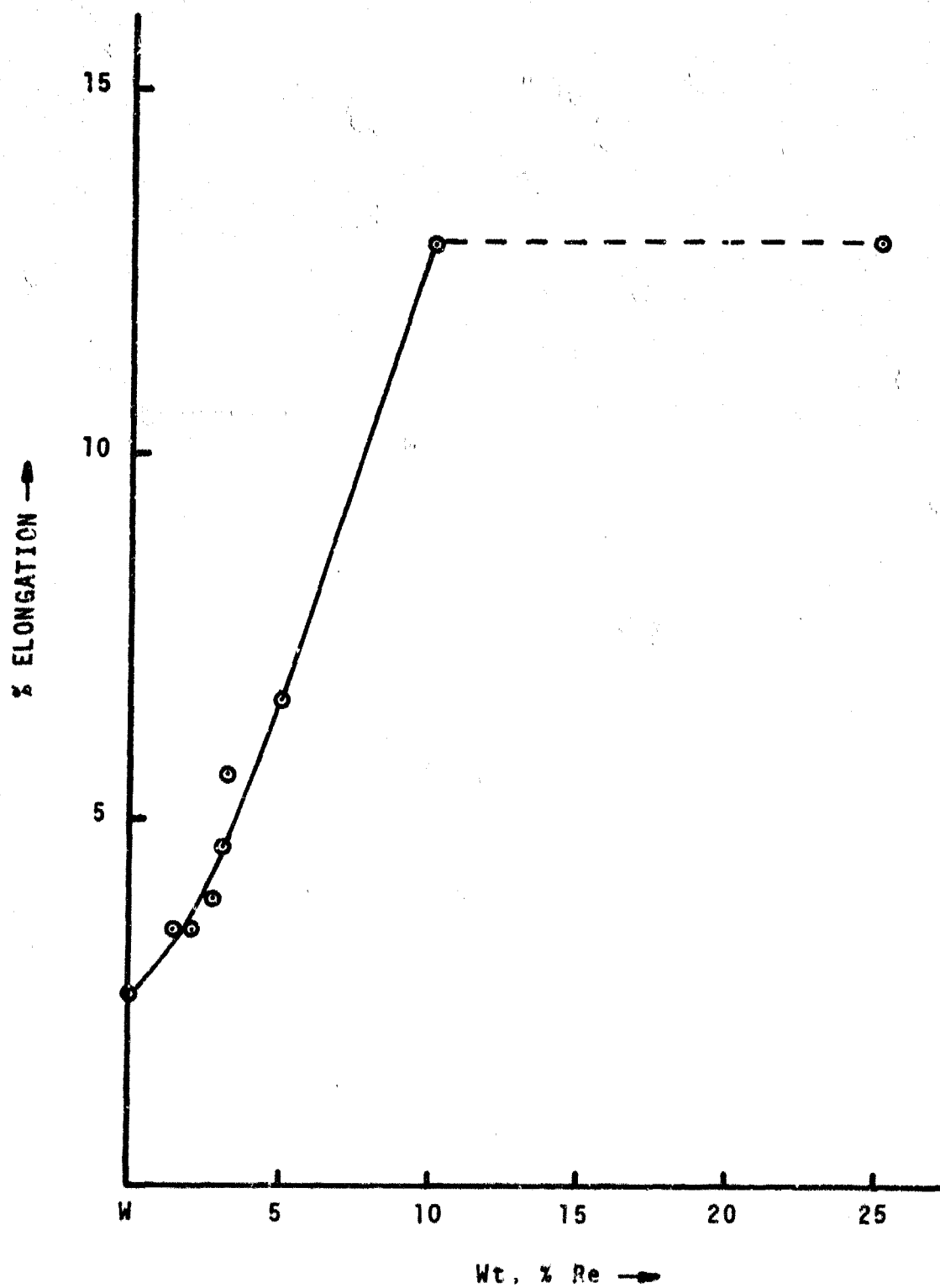


Figure 21. Effect of rhenium additions on the tensile ductility of tungsten.

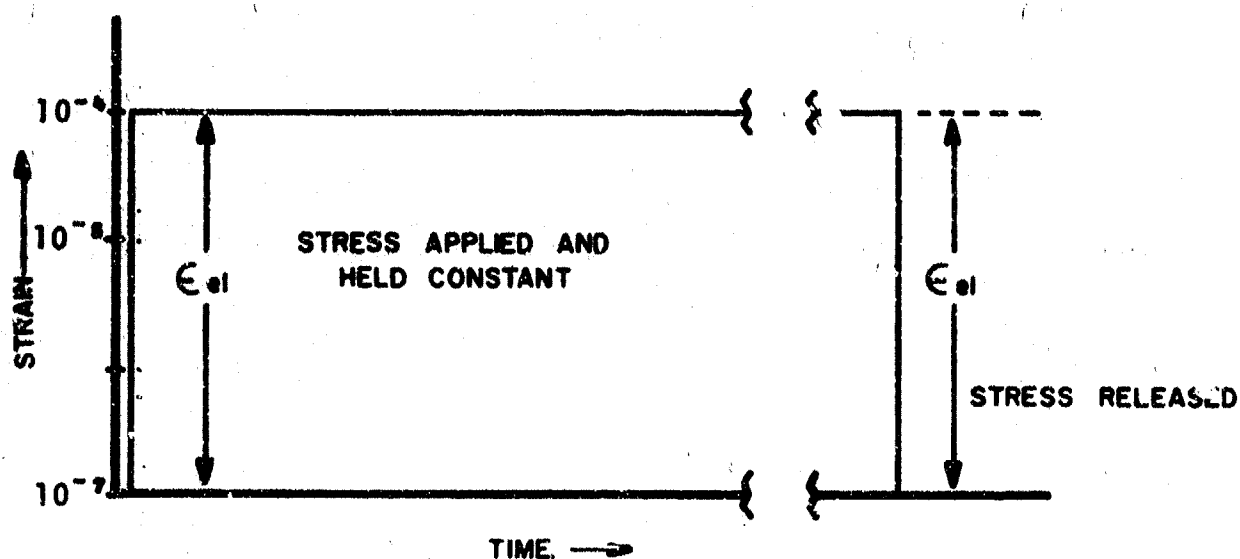


Figure 22. Schematic data curve for anelastic relaxation measurements.

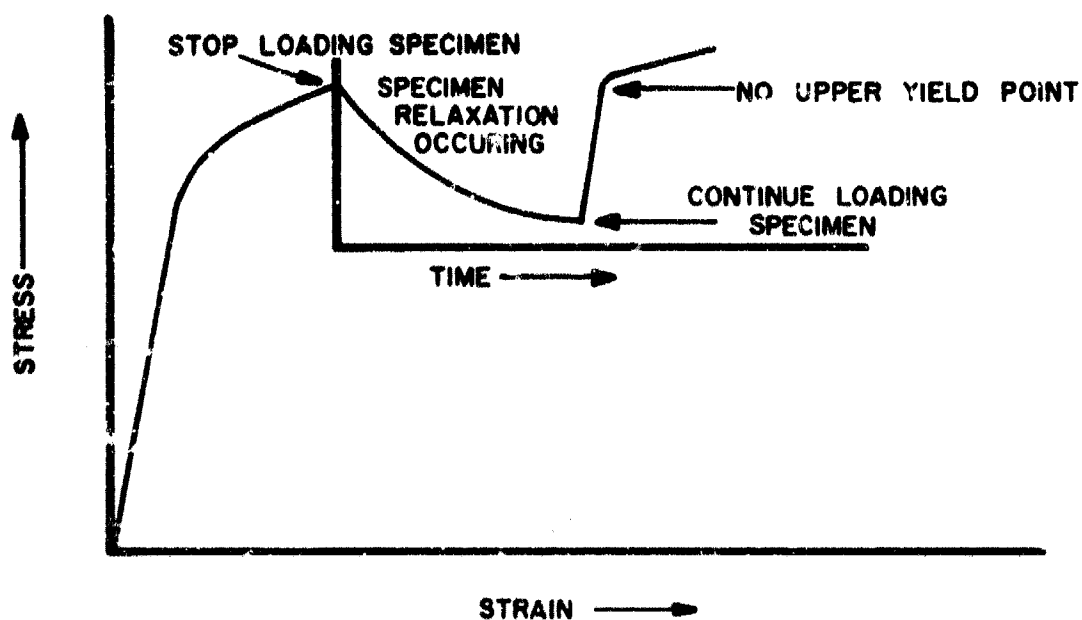


Figure 23. Schematic data curve representative of all stress relaxation measurements.



a.)



b.)

Figure 24. Photomicrograph of W-3w/oRe after carburization, longitudinal section a.) unrecrystallized, b.) recrystallized grains at 200X.

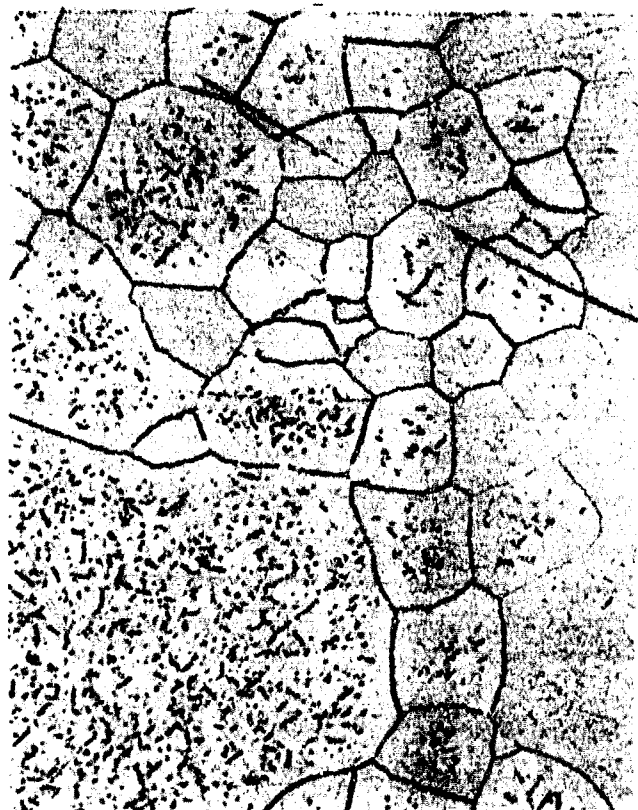
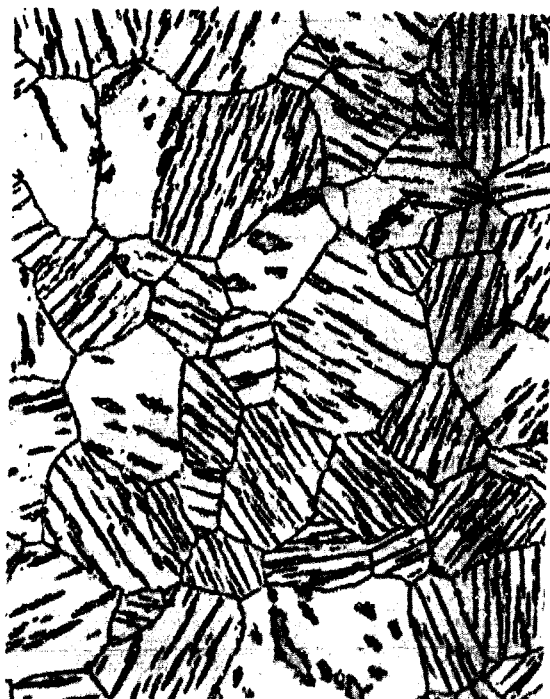


Figure 25. Photomicrograph of W-25w/o Re after carburization, longitudinal section showing crystallographic type precipitates at 200X.



a.)



b.)



c.)

Figure 26. Photomicrograph of unalloyed tungsten after carburization a.) transverse section at 90X, b.) longitudinal section before polishing into center region of different structure at 200X, c.) longitudinal section showing center as well as outer microstructure at 200X.

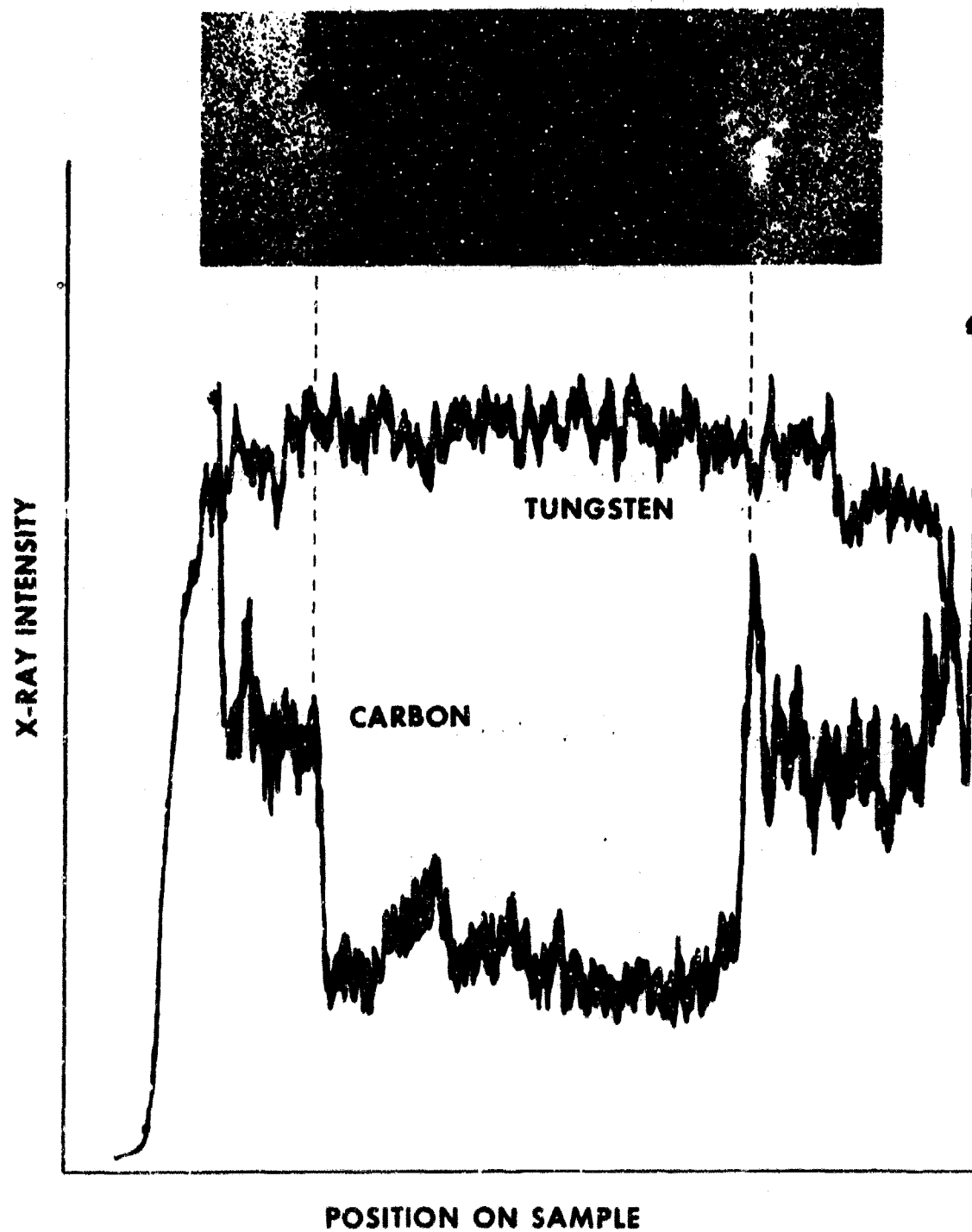


Figure 27. Electron microprobe carbon scan of the unalloyed tungsten microstructure shown in Figure 26c.



Figure 28. Transmission electron micrograph of carbon replica of polished and etched W-5w/oRe microstructure at 2500X.



Figure 29. Transmission electron micrograph of fracture surface carbon replica showing extracted precipitate like particles in unalloyed tungsten at 3400X. Electron diffraction identified them as tungsten.

TABLE V
METAL IMPURITY ANALYSIS OF STARTING MATERIAL

[illegible]

TABLE VII
MICROHARDNESS * AND TENSILE DATA

Material	Vickers Number (Rc Conversion) (DPH)	Y. S. ** (ksi)	UTS (ksi)	%El	E ($\times 10^6$ psi)
Unalloyed W	522	175	196	2.6	61.5
W-1 $\frac{1}{2}$ Re	496	169.5	192.5	3.5	56.2
W-3 Re	507	162	198	4.6	49.7
W-2 Re	494	163.5	191.5	3.5	54.2
W-2.75 Re	505	159	192	3.9	51.2
W-3 Re	498	157.5	188	5.1	48.8
W-3.25 Re	490	168	191	5.3	43.4
W-5 Re	480	160.5	189.5	6.6	43.1
W-10 Re	634	192	208	12.9	46.7
W-25 Re	700	203.5	233	12.9	52.6

* 500 gm load with Vickers diamond pyramid indenter

** 0.2% offset measurement

3.3 Auger Electron Spectroscopy of Recrystallized Alloy Fracture Surface

The use of Auger electron spectroscopy (AES) affords a good qualitative detection and examination of elements present on a clean fracture surface and grain boundaries. A typical Auger trace representative of most of the fractured alloy surfaces examined in this study is given in Figure 30. This particular curve is taken from the W-3.25Re sample that had been given the electron-beam zone-refining heat treatment (EBHT). The various elements found on the fracture surface are designated on this Auger trace. As the figure shows, the potassium peak is quite large, with carbon and oxygen also present. The most prevalent element found on all the class 2 and class 3 material fracture surfaces was potassium (see Table I for class designation). The same peaks were present, but not as pronounced for class 1 material and absent from class 4 samples. The presence (or absence) of potassium did not depend on the particular heat treatment (i. e., VHT or EBHT - see Table XI) used for recrystallization. This is in agreement with the atomic absorption bulk analysis ^{*} for potassium as given in Table VIII. This Table also includes atomic absorption analysis for rhenium which is in agreement with the nominal compositions. Atomic emission spectroscopy showed that the concentration of metal impurity elements was not affected by the particular heat treatment (Table VI compared with

^{*}See Chapter II (Section 2.7) for a description of this technique.

Table V). Only the bulk carbon content was altered by the long high temperature exposure of the VHT, as the results in Table IX demonstrate. This change in bulk carbon content with heat treatment was not reflected at the grain boundary surfaces analyzed with AES. The C/W peak ratios were not consistently higher for the VHT samples immediately after fracture.

The principal Auger energies for tungsten, rhenium and potassium are tabulated in Table X. There is pronounced overlap between the tungsten and the rhenium peaks and they could only be resolved at the higher energy peaks (> 1000 eV and around 1800 eV in particular). Rhenium was not detected in samples having less than five weight percent Re in either the high or low energy spectra. There are two contributing factors responsible for this low detectability. First, the tungsten-rhenium peaks overlap in the low energy range (Table X) and secondly, the Auger yields are smaller in the higher energy ranges where the peaks are resolvable.

The results of AES traces before and after argon ion bombardment of the fracture surfaces are presented in Table XI. The numbers in parentheses in columns 6 and 7 refer to the respective potassium (251 eV) to tungsten (170 eV) Auger peak-to-peak height ratios used to determine the coverages given. The advantage of using peak height ratios is discussed in detail in Chapter IV (Section 4.2.1). In most cases after ion bombardment, all the potassium present on the fracture surfaces was removed with a single sputtering. A representative Auger trace

for this instance is shown in Figure 31. It is the same specimen from which Figure 30 was taken, namely EBHT W-3.25Re, for comparison and continuity. There were several instances, however, when a single bombardment (and in some cases four or five bombardments) was not sufficient to remove all the potassium from the fracture surface. It is of interest to note that the few samples where all the potassium was not sputtered off the fracture surfaces had undergone the electron-beam zone refining heat treatment. Not too much emphasis can be placed on the relative amounts of either carbon or oxygen before or after sputtering because these two elements are typical surface and bulk contaminants found on tungsten (and most other refractory metals) examined by AES in ultrahigh vacuum.

Several anomalies appeared on some of the samples studied and it may be worthwhile to mention some of them. On the electron-beam zone refined (EBHT) pure tungsten sample, a readily detectable Auger peak at 990 eV due to sodium was seen. Potassium was also present on this sample. Sodium was never detected on any of the alloyed samples. On the $1\frac{1}{2}\%$ and 3% Re commercial grade samples (class 2), large sulfur Auger peaks were detectable on both samples after fracture in the EBHT specimens. The absence of sulfur on these same materials given the vacuum heat treatment is still open to conjecture. It is noteworthy that in the EBHT W- $1\frac{1}{2}$ Re and W-3Re samples the normal first ion bombardment was sufficient to remove all traces of sulfur from the surface.

This first bombardment was not sufficient, however, to remove potassium from these samples. In fact, on these two particular samples where sulfur was initially found, several (at least 3) sputterings were not adequate to remove all the potassium from the bombarded fracture surfaces. Sulfur was found after fracture on other samples as well (e.g., VHT 2Re, 3Re, 5Re, and 10Re samples), but in no instance did the presence of sulfur coincide with difficult removal by sputtering of the potassium found originally on the fractured surfaces. Sulfur was also easily removed by argon ion bombardment. In contradistinction to earlier Auger studies of intergranular fracture surfaces in tungsten^(61, 75) only very minute amounts of phosphorus (never more than 1% of the 170 eV tungsten peak) were found on any of the samples in this study. It seems to be present only in billets sintered in vacuum furnaces at relatively low temperatures (1800°-2200°C). Material sintered by resistance heating (2800°-3000°C) are relatively free of phosphorus.

3.4 Scanning Electron Microscopy of Recrystallized Alloy Fracture Surfaces

A thorough characterization of the fracture surface of each Auger specimen was performed with the use of scanning electron microscopy. All the recrystallized samples had a fracture that was typically 90% intergranular as shown in Figure 32 for unalloyed tungsten. Each grain boundary surface was covered with bubble-like porosity similar to that of Figure 33. The bubbles are spherical in shape and range in size from 0.1 μ to 10 μ . The smallest bubbles were found in the unalloyed tungsten

(Figure 34) which is expected from the different doping procedures and the low potassium concentration in the Auger and chemical analysis results of Tables XI and VIII, respectively. An example of very large bubbles is presented in Figure 35. They most likely form by coalescence and spheroidization of many smaller bubbles as the grain boundary surface sweeps through the material during recrystallization and grain growth. It is interesting to note the flat, parallel sides of the largest bubbles.

In general, the bubbles are randomly distributed on grain boundary fracture surfaces (Figure 36) although there are rare situations where they are linear (Figure 37). They were generally much larger and their arrangement was much less linear than those arrays reported by other investigators⁽⁷⁵⁻⁸²⁾, and they never occurred on transgranular fracture surfaces. It has been suggested that the presence and stability of these rows are related to the suitability of these materials for lamp filaments⁽⁸⁰⁾. Bubbles were not found in class 4 alloys which is expected from the chemical analysis (Table VIII) and AES results (Table XI), and were relatively small and few in number for the unalloyed tungsten, class 1 (Figure 34). The density of bubbles was noticeably greater and their size slightly smaller for VHT samples than EBHT material.

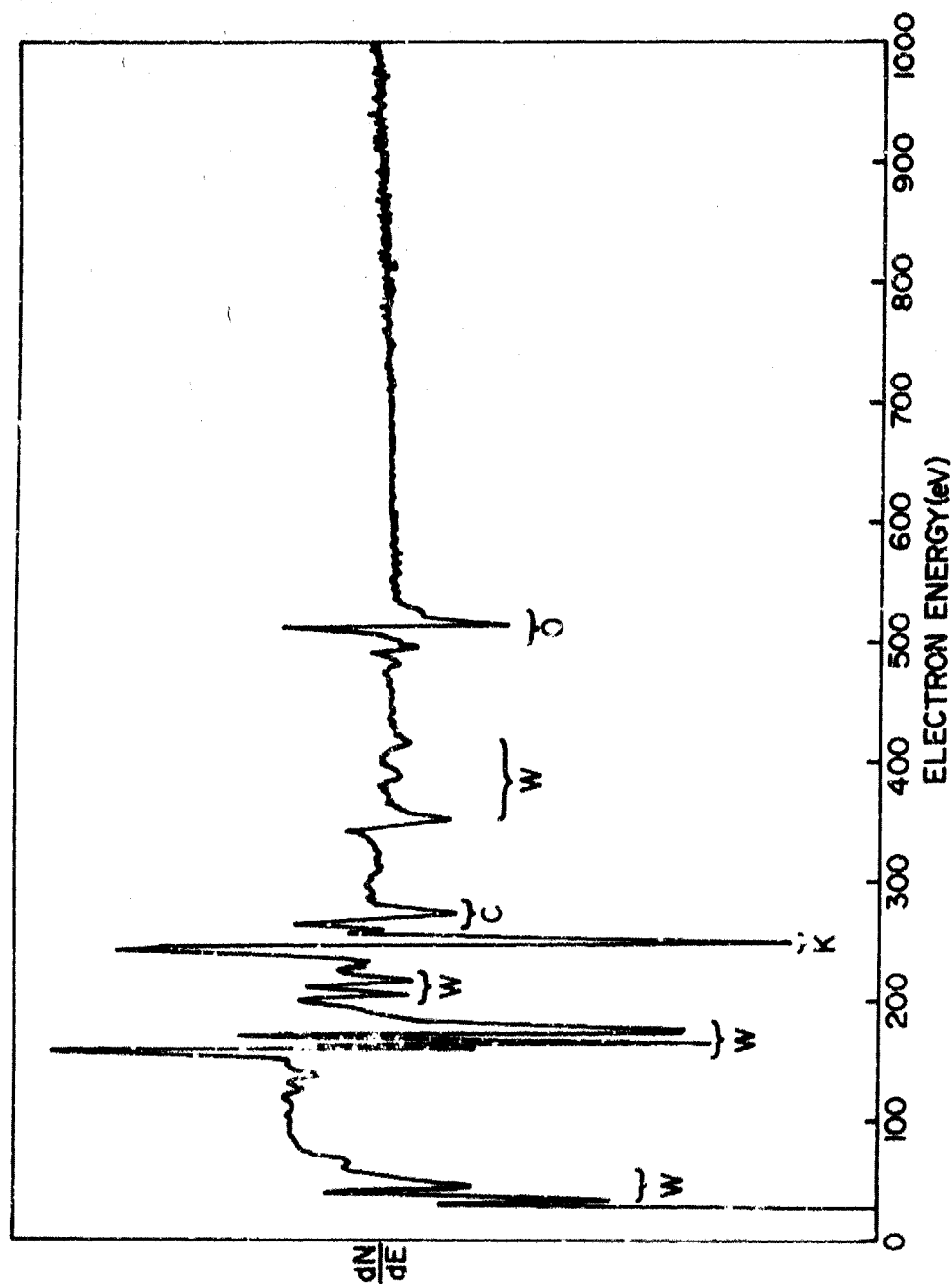


Figure 30. Auger electron spectra of sample W-3.25w/o Re taken in situ immediately after intergranular fracture at room temperature. Primary electron beam voltage: 3.0 K eV; modulating voltage: 1 eV peak-to-peak; sample current: 56 μ A; amplifier gain: 100 μ V; Y-axis recorder: 1/2 V/in; electron multiplier voltage: 1300 V; time constant: off.

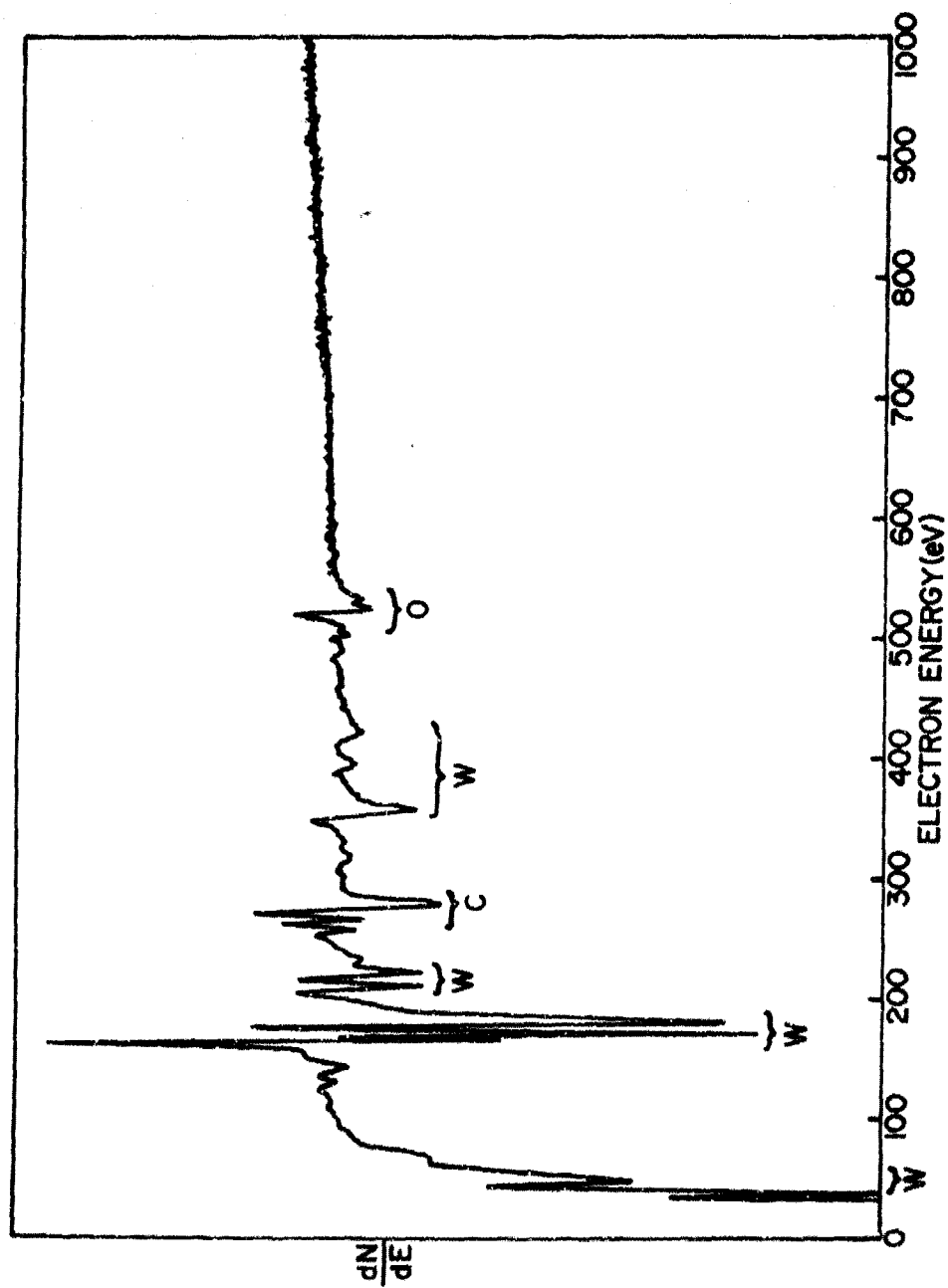


Figure 31. Auger electron spectra of sample W-3.25w/oRe grain boundary fracture surface taken in situ immediately following a 20 minute, 200 μ A current, 500 eV ion, argon ion bombardment. Primary electron beam voltage: 3.0 K eV; modulating voltage: 1 eV peak-to-peak; sample current: 50 μ A; amplifier gain: 100 μ V; Y-axis recorder: 1/2 V/in; electron multiplier voltage: 1300 V; time constant: off.



Figure 32. Scanning electron micrograph of etched tungsten wire showing outer wire surface and intergranular fracture surface.

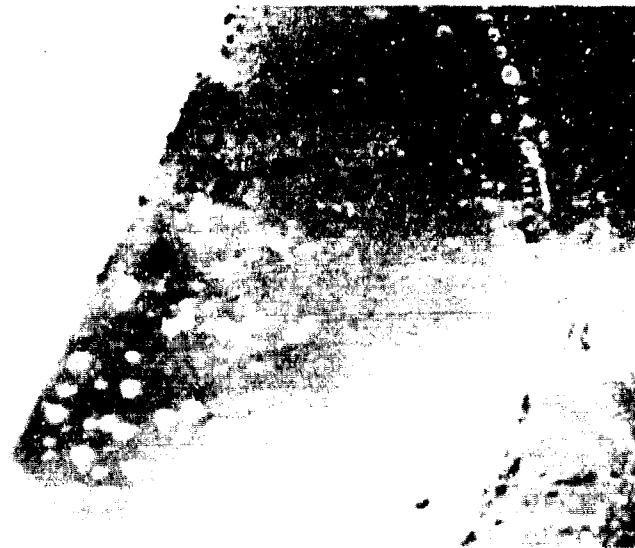


Figure 33. Scanning electron micrograph of bubbles on the intergranular fracture surface at doped W-3w/o Re.



Figure 34. Intergranular fracture surface of unalloyed tungsten.



Figure 35. Unusually large potassium bubbles on the fracture surface of doped W-3.25w/o Re.

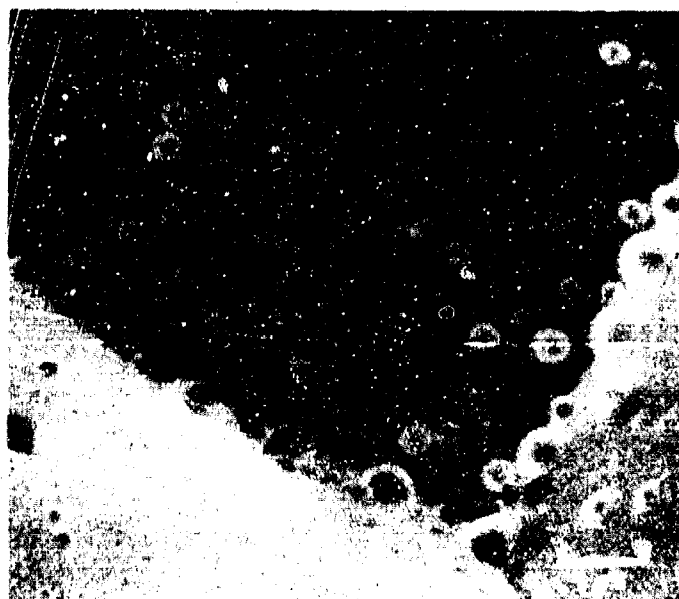


Figure 36. Randomly distributed bubbles on the intergranular fracture surface of doped W-5w/o Re.



Figure 37. Scanning electron micrograph showing occasional rows of bubbles on the intergranular fracture surface of W-5w/o Re.

TABLE VIII

RHENIUM AND POTASSIUM COMPOSITION BEFORE AND AFTER HEAT TREATMENT

Class	Nominal Composition (Wt. %Re)	Rhenium		Potassium			
		As Received (Wt. %Re)	(1) After VHT (Wt. %Re)	(2) After EBHT (Wt. %Re)	As Received (ppm K)	(1) After VHT (ppm K)	(2) After EBHT (ppm K)
1	Unalloyed W				5	5	5
2	W-1 $\frac{1}{2}$ Re		1.55	1.48	51	50	53
2	W-3 Re		3.13	3.23	47	45	53
3	W-2 Re		2.10	2.10	49	50	45
3	W-2.75 Re		2.83	2.88	40	35	32
3	W-3 Re		3.13	3.13	50	45	47
3	W-3.25 Re		3.30	3.40	46	45	44
3	W-5 Re		5.10	5.16	44	44	41
4	W-10 Re	10.6			5	5	5
4	W-25 Re	26.6	26.3	26.8	5	5	5

-62-

Material of each composition was given in two different recrystallization heat treatments:

- 1.) 2600°C for 100 hours in vacuum furnace at 3×10^{-6} torr, (VHT).
- 2.) 2100±50°C with electron beam moving 2 in/hour at $2-5 \times 10^{-6}$ torr, (EBHT).

TABLE IX
AVERAGE INTERSTITIAL CHEMICAL ANALYSIS
BEFORE AND AFTER HEAT TREATMENTS

Element	As Received (ppm)	After VHT ⁽¹⁾ (ppm)	After EBHT ⁽²⁾ (ppm)
C	24±5	66.5±5	29.2±5
N	10	10	10
O	10	10	10

(1) 2600°C for 100 hours in vacuum furnace at 3×10^{-6} torr, (VHT).

(2) 2100±50°C with electron beam moving 2 in/hour at $2-5 \times 10^{-6}$ torr, (EBHT).

TABLE X
CHARACTERISTIC AUGER ELECTRON ENERGIES (eV)
FOR TUNGSTEN, RHENIUM AND POTASSIUM

TUNGSTEN				RHENIUM				POTASSIUM
38	115	180 *	387	33	138	215	422	218
49	130	208	413	45	161*	227	1573	229
53	143	220	1523	74	167*	292	1624	234
70	164 *	229	1571	97	175*	349	1799	251*
85	170 *	310	1736	113	177*	360	1858	271
101	178 *	351	1796	127	202	401		

* Denotes major (or larger) peaks that are used in the determination of coverages.

POTASSIUM COVERAGES OF SAMPLES FOLLOWING FRACTURE AND ARGON ION BOMBARDMENT

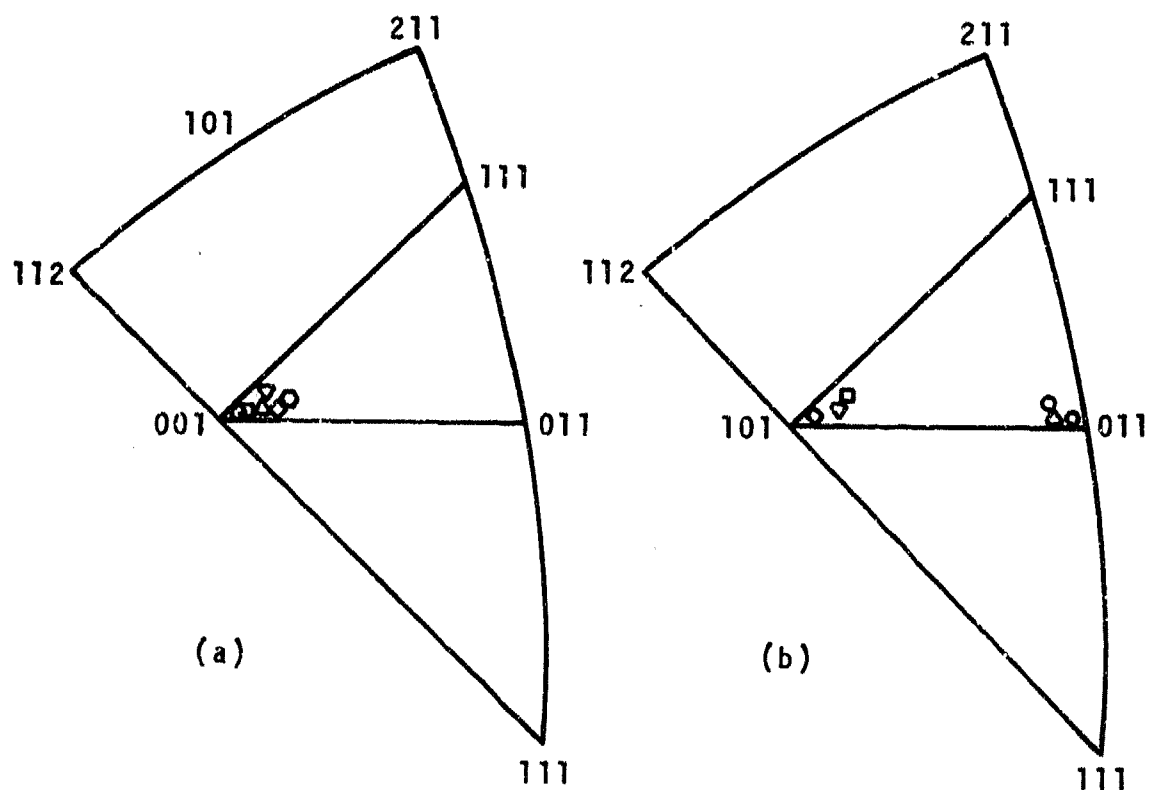
-64-

***All ratios and equivalent K coverage values are the average of several Auger traces taken immediately after fracture or bombardment.

***These samples could not be ion bombarded due to the way they fractured in the sample holder.

3.5 Single Crystal Compression Measurements

The compression strain rate cycling technique is more convenient for measuring the thermal component of flow stress than tensile tests because of the inherent brittle character of tungsten and its alloys at low temperatures. The complete list of single crystals tested is shown in Table IV along with the temperature of each test. Each specimen was cut from an electron beam zone refined rod and analyzed nondestructively with X-ray fluorescence for relative values of rhenium content. A calibration curve was prepared using the 0% and 9% rhenium points to get the quantitative results in Table I. The orientation of each sample was determined by the back reflection Laue X-ray technique and is reported in Figure 38. Most of the crystals grown from a $\langle 100 \rangle$ seed gave diffraction patterns with the $\langle 100 \rangle$ pole right on the sample cylindrical axis and none were off more than 2° , the estimated accuracy of the measurement. There was, however, considerable drift in alloys grown from the $\langle 110 \rangle$ seed. The amount of drift is strongly related to rhenium content. Unalloyed tungsten was right on the $\langle 110 \rangle$ pole while the W-1Re and W-2Re crystals were off 5° - 6° (Table XII). At higher rhenium contents, the zone refined rod started out at $\langle 110 \rangle$ and within a quarter of an inch of the seed snapped over to $\langle 100 \rangle$ (Figure 38). This same effect was observed by Sylvania researchers⁽⁸³⁾, who were never successful at growing $\langle 110 \rangle$ tungsten-rhenium crystals closer than 6° to the $\langle 110 \rangle$ axis. The effect is found in other



Nominal Composition
Wt. % Re

⬡	Unalloyed W
⬠	W - 1Re
◯	W - 2Re
◊	W - 3Re
▽	W - 5Re
◻	W - 9Re

Figure 38. Orientation of single crystals used in compression measurements grown from: a.) $\langle 100 \rangle$ seed, b.) $\langle 110 \rangle$ seed.

TABLE XII
SINGLE CRYSTAL ORIENTATION AND TEST TEMPERATURE

Sample	Nominal Comp	Seed Orientation	Sample Orientation	Misalign- ment	Test Temp (°K)
00	Unalloyed W	<100>	<100>	2°	295
01				0°	202
02				2°	120
05		<110>	<110>	0°	295
06				1°	198
07				0°	118
10					
11	W-1 Re	<100>	<100>	1°	295
12				1°	192
15				2°	120
16		<110>	<110>	4°	295
17				4°	199
				5°	85
20	W-2 Re	<100>	<100>	0°	295
21				0°	190
22				0°	127
25		<110>	<110>	5°	295
26				4°	183
27				5°	140
30	W-3 Re	<100>	<100>	3°	295
31				1°	199
32				2°	119
35		<110>	<100>	1°	295
36				1°	194
37				3°	110
50	W-5 Re	<100>	<100>	2°	295
51				2°	198
52				2°	119
55		<110>	<100>	5°	295
56				4°	198
57				6°	108
90	W-9 Re	<100>	<100>	0°	295
91				0°	107
92				0°	114
95		<110>	<100>	7°	295

refractory alloy systems, such as tantalum-tungsten⁽³⁸⁾. The test crystals are listed with an identification number, composition, orientation, misalignment, and test temperature in Table XII. The Schmidt factor (0.47) was determined for the (112) $\langle 111 \rangle$ slip system.

Each crystal was examined for shape change after deformation and without exception gave results shown in Figure 39. The $\langle 110 \rangle$ crystals always had a pronounced elliptical shape with a $\langle 100 \rangle$ major axis and $\langle 110 \rangle$ minor axis. The $\langle 100 \rangle$ crystals always had the general shape in Figure 39, but in most cases two adjacent $\langle 110 \rangle$ "bumps" were highly pronounced. This means that most of the deformation occurred on two slip systems, which is also the case for the $\langle 110 \rangle$ crystals. The top and bottom portions of the crystals always deformed equally with the center. This is important because it means there was no bulging, i. e., there was essentially no friction between the specimen and the highly polished hardened steel loading blocks on each end. The deformation was uniform throughout the crystals; there were no significant bending moments.

Examples of typical stress-strain curves are shown in Figures 40 and 41 for unalloyed tungsten and W-3Re $\langle 100 \rangle$ crystals. Each curve for a particular crystal was produced sequentially during continuous testing. Strain rate cycling measurements were taken between unloading points, accounting for some of the accumulated plastic strain. In each case, however, the crystal was unloaded (except for a small prestrain

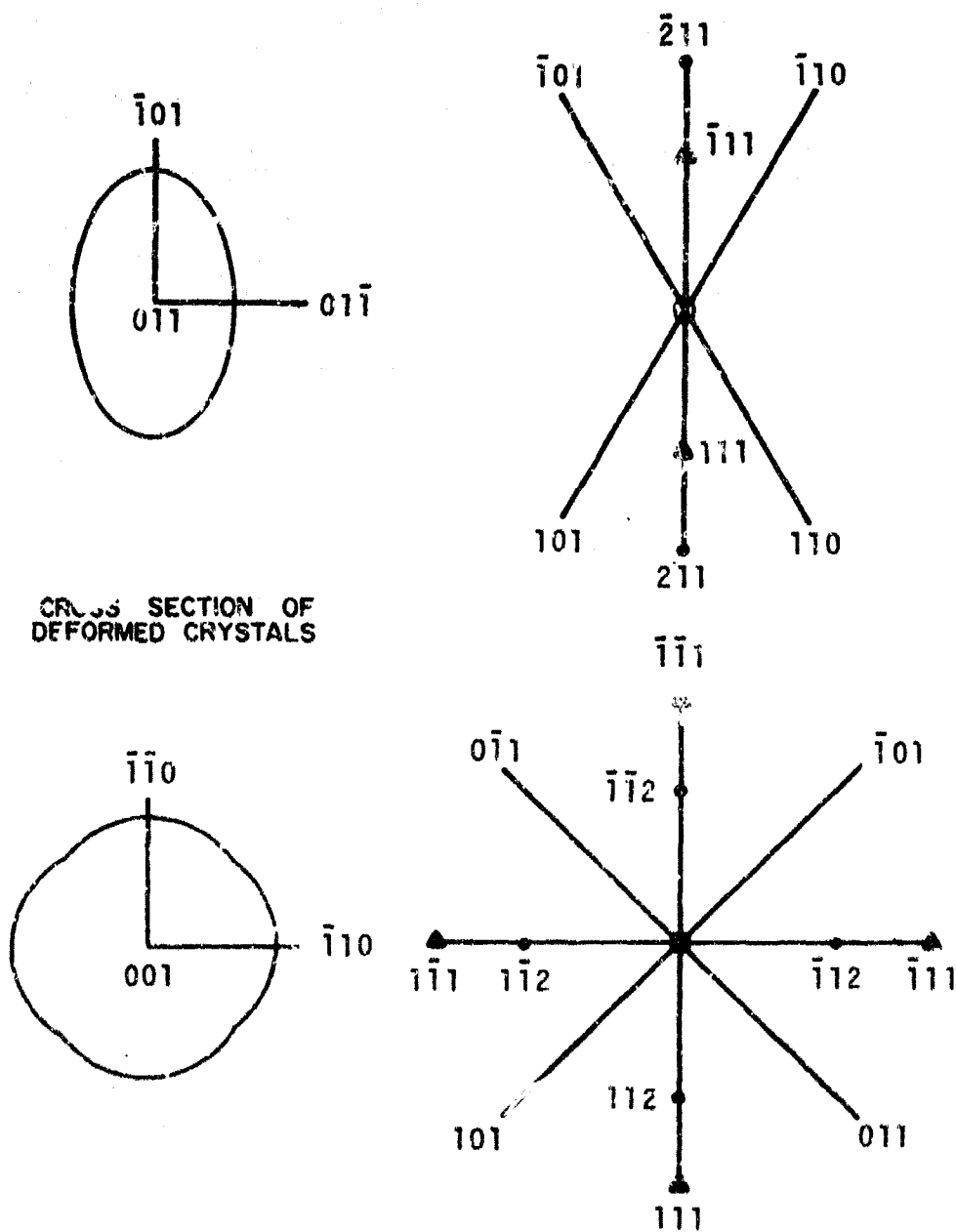


Figure 39. Shape change and slip system analysis for compression loaded $\langle 100 \rangle$ and $\langle 110 \rangle$ single crystals.

to maintain alignment) between curves. The time between runs varied from six hours (during temperature change) to fifteen minutes. The virgin zone refined crystals began deforming plastically at exceptionally low stress during the initial 2% prestress deformation. This phenomenon is indicative of exceptionally pure material, free of pinning sites, and an unusually high initial mobile dislocation density. The low yield point of curves (3) and (4) is difficult to explain, particularly curve (4) which would be expected to follow the elastic slope close to the stress before unloading of curve (3). It is possible that the high purity of the samples allowed them to relax, relieving internal stress and lowering the stress required for macroscopic dislocation motion. This relaxation is highly unusual, however, and it seems more likely that it is due to machine effects. In either case it will not affect the strain rate change measurements.

The strain rate cycling data were plotted according to the Michalak relationship⁽⁷⁴⁾:

$$\frac{m^* \Delta \tau}{\ln(\dot{\epsilon}_2/\dot{\epsilon}_1)} = \tau^* + \frac{\Delta \tau}{2} \quad (3.1)$$

This relationship gives values of effective stress, τ^* (yield stress concept) and dislocation velocity exponent, m^* (slope). Example plots are shown for W-1Re and W-3Re in Figures 42 and 43. An important assumption in the derivation of this expression is that the mobile dislocation density and the dislocation structure does not change during a given change in strain

rate. The results are given for the 295°K measurements in Table XIII along with the activation volume, V^* , calculated from the relationship

$$V^* = kT \frac{m^*}{\tau^*} \quad (3.2)$$

An example calculation is given in Appendix II along with the derivation of the equation.

The effect of rhenium additions to tungsten on the thermal component of flow stress, τ^* , is shown in Figure 44. This effect is strikingly similar to the hardness change with rhenium additions measured on the same crystals (Figure 45 and Table XIV). The importance of this similarity is reviewed in the discussion section (Chapter IV). Both the dislocation velocity exponent, m^* , and activation volume, V^* , decrease with initial rhenium additions to tungsten (Figures 46 and 47, respectively). While m^* increases slightly, V^* shows a large increase above 3 w/o Re.

Plots of equation 3.1 (Figures 42 and 43) are difficult to obtain below 295°K because the slope is too steep to be measured accurately. The experimental scatter in the low temperature measurements masked the effect of m^* and τ^* variations with rhenium content. It is possible however, to show the general effect of temperature on these properties by presenting the results for the best case (Figures 48-50). When m^* could be measured it was near 10-11 at 200°K and 20 at 100°K, but no quantitative significance should be placed on these values, because of difficulties in experimental accuracy at low temperatures.

TABLE XIII

STRAIN RATE CYCLING DATA

Nominal Composition Wt. % Re	τ^* (psi)	m^*	v^* (b^3)
<100>			
Unalloyed W	3,845	9.1	68.4 b^3
W-1 Re	3,088	6.8	63.6
W-2 Re	2,350	4.9	60.2
W-3 Re	2,325	4.5	55.9
W-3 Re +	2,295	4.6	57.9
W-5 Re	2,092	4.7	64.9
W-9 Re	1,988	4.8	69.7
<110>			
Unalloyed W	3,900	8.5	63.0
W-1 Re	3,500	6.6	54.5
W-2 Re	2,630	5.6	61.5

+Grown from a <110> seed

TABLE XIV

EFFECT OF RHENIUM ON SINGLE CRYSTAL HARDNESS

Nominal Composition Wt. % Re	Hardness 30-N and (DPH)			
	<100> Seed		<110> Seed	
Unalloyed W	64.3	(450)	58.8	(384)
W-1 Re	61.6	(416)	58.2	(378)
W-2 Re	60.9	(407)	57.2	(368)
W-3 Re	60.4	(402)	60.4	(402)
W-5 Re	55.0	(346)	55.0	(346)
W-9 Re	53.5	(330)		

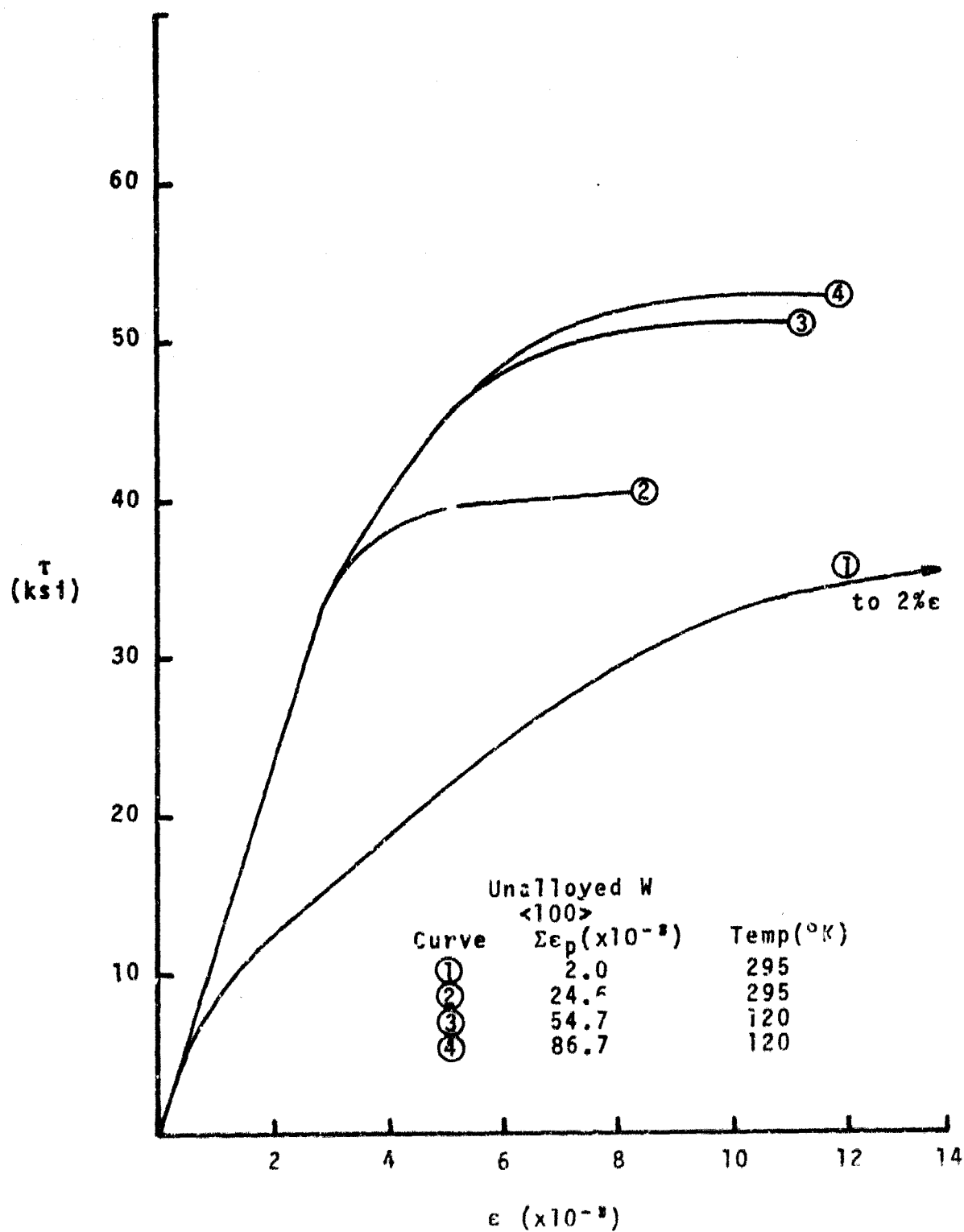


Figure 40. Stress-strain curves for <100> tungsten crystal at increasing accumulated plastic strain levels.

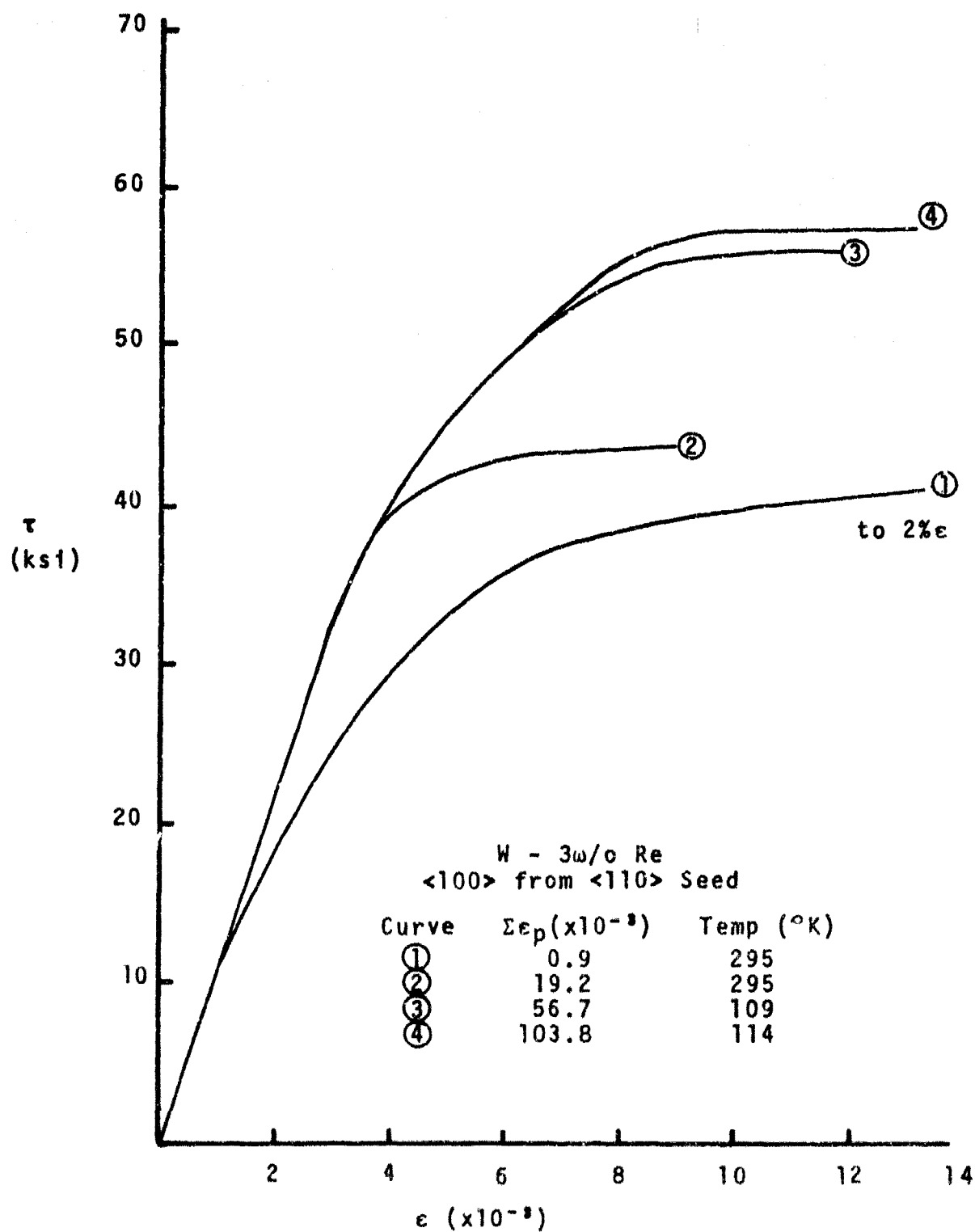


Figure 41. Stress-strain curves for <100> W-3w/o Re crystal at increasing accumulated plastic strain levels.

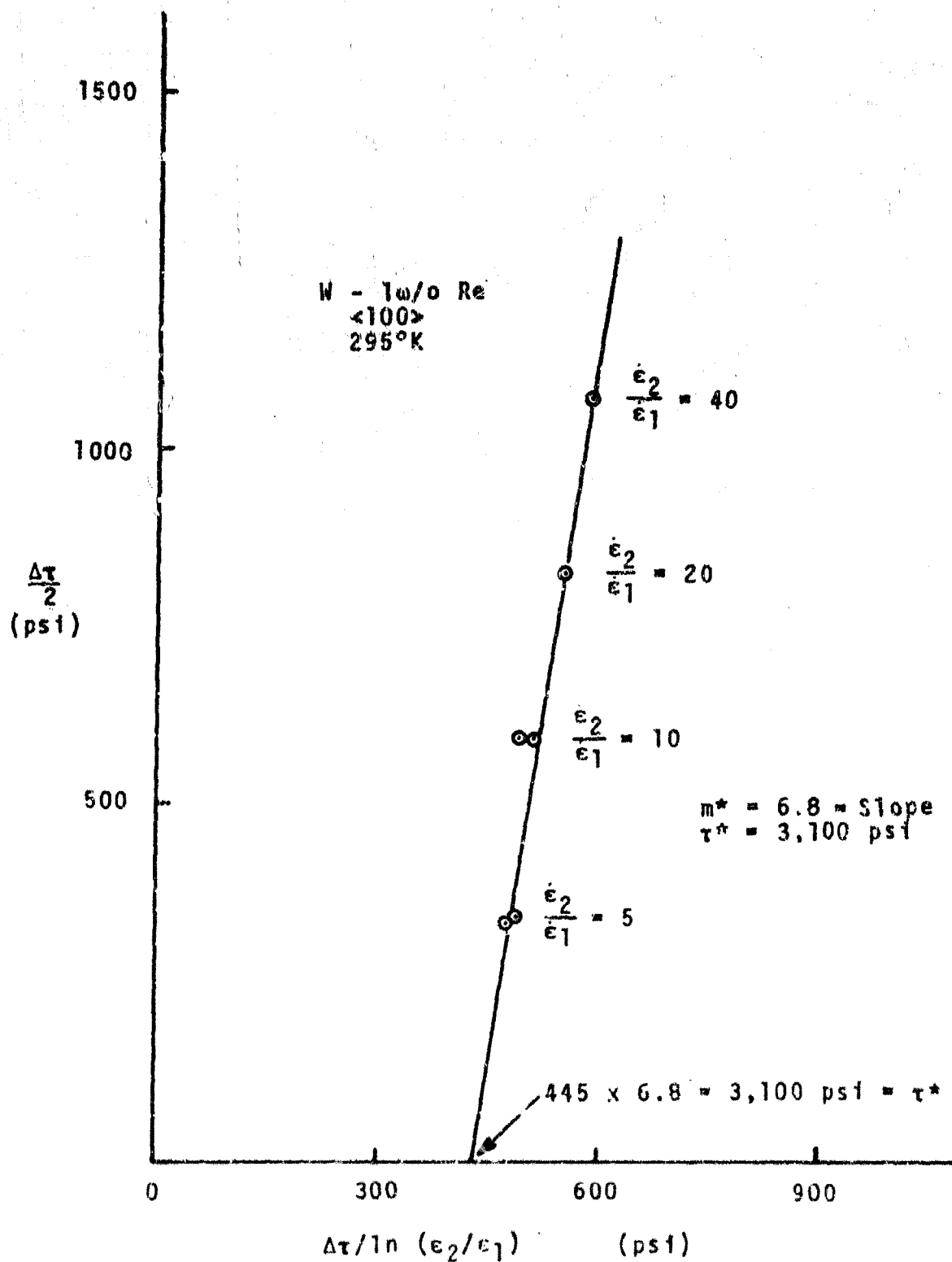


Figure 42. Strain rate change data plotted according to equation 3.1 to give τ^* and m^* values for <100> W-1w/o Re.

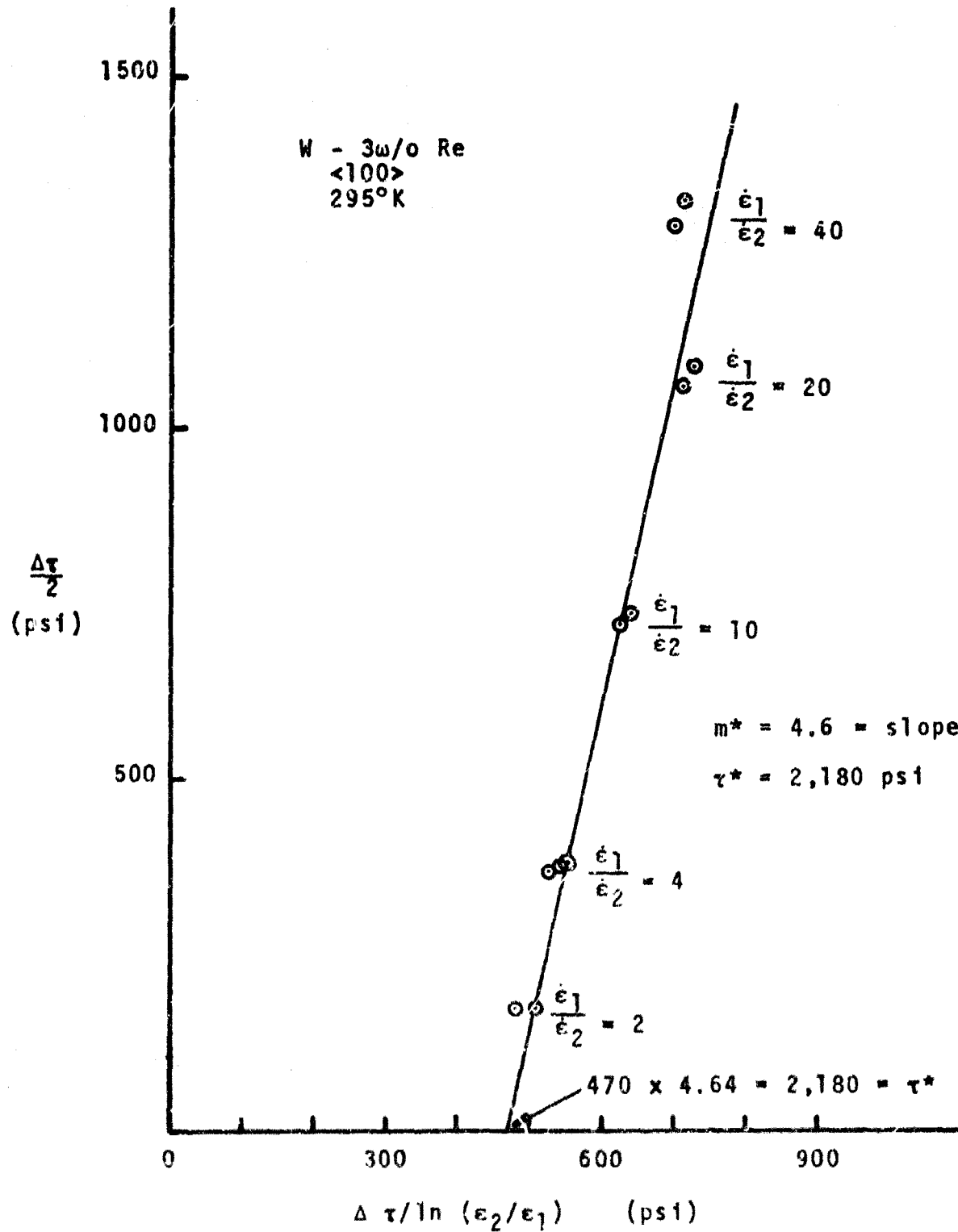


Figure 43. Strain rate change data plotted according to equation 3.1 to give τ^* and m^* values for <100> W-3w/o Re.

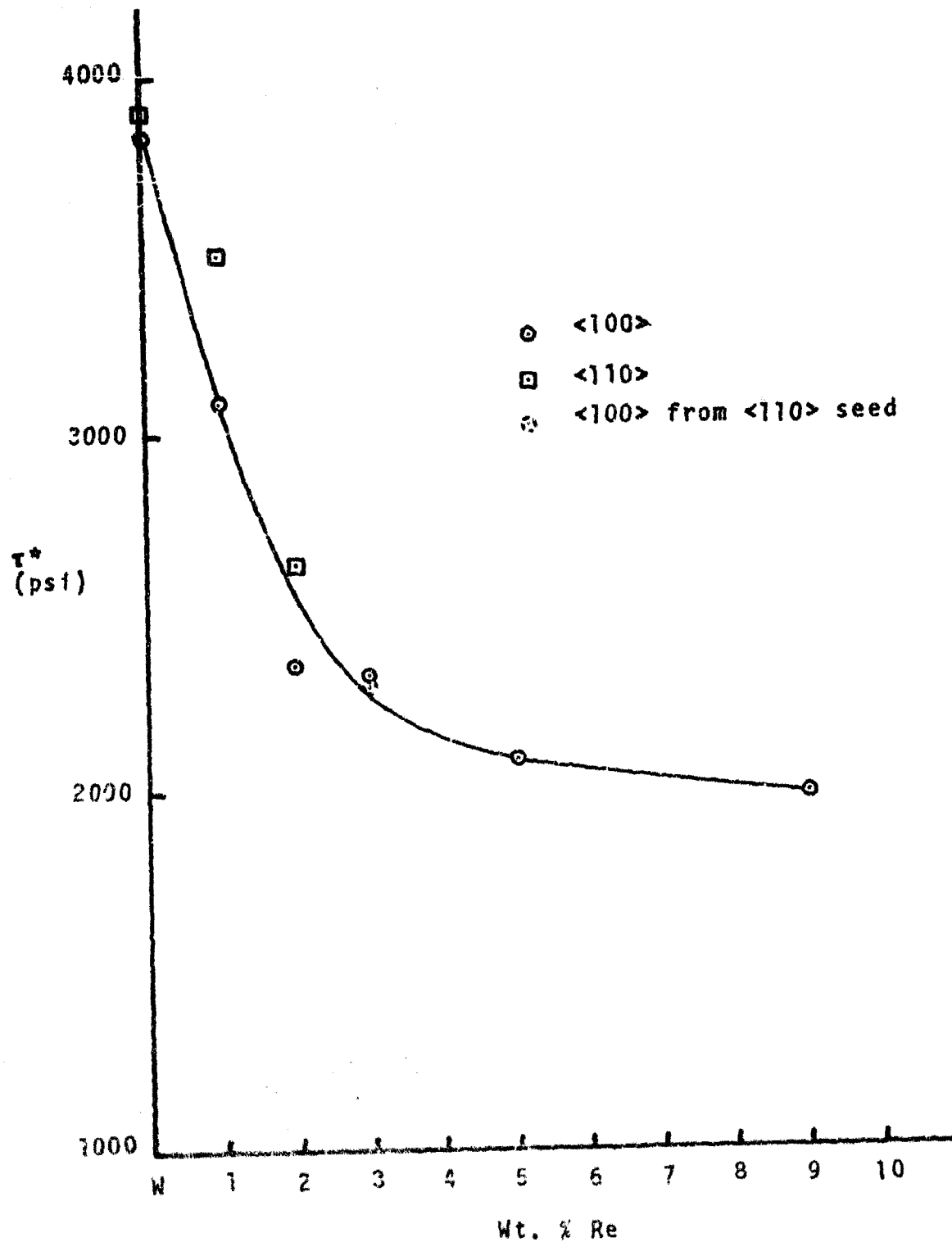


Figure 41. Effect of rhenium additions to tungsten on the thermal component of flow stress, τ^* (effective stress).

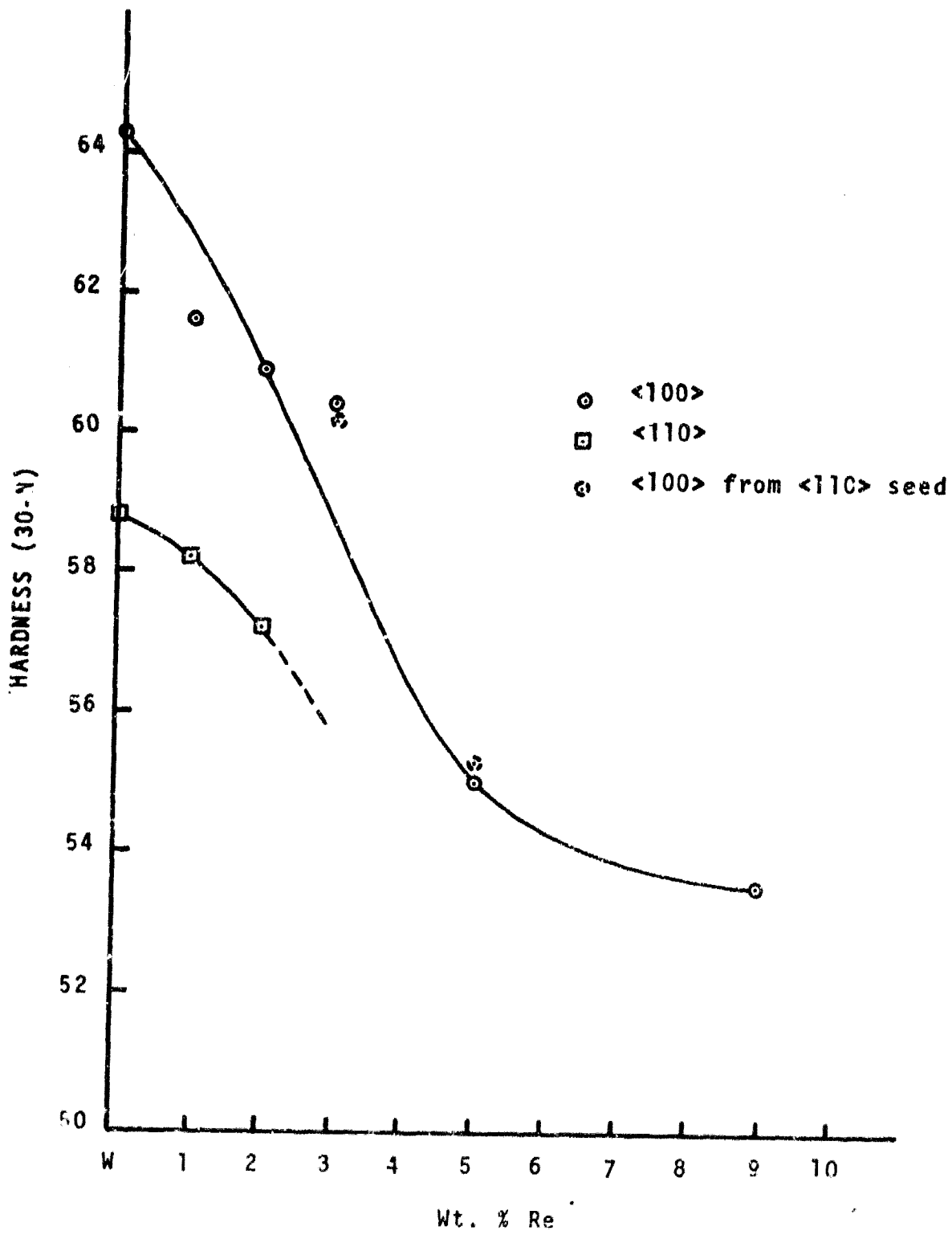


Figure 45. Hardness variations with rhenium additions to tungsten.

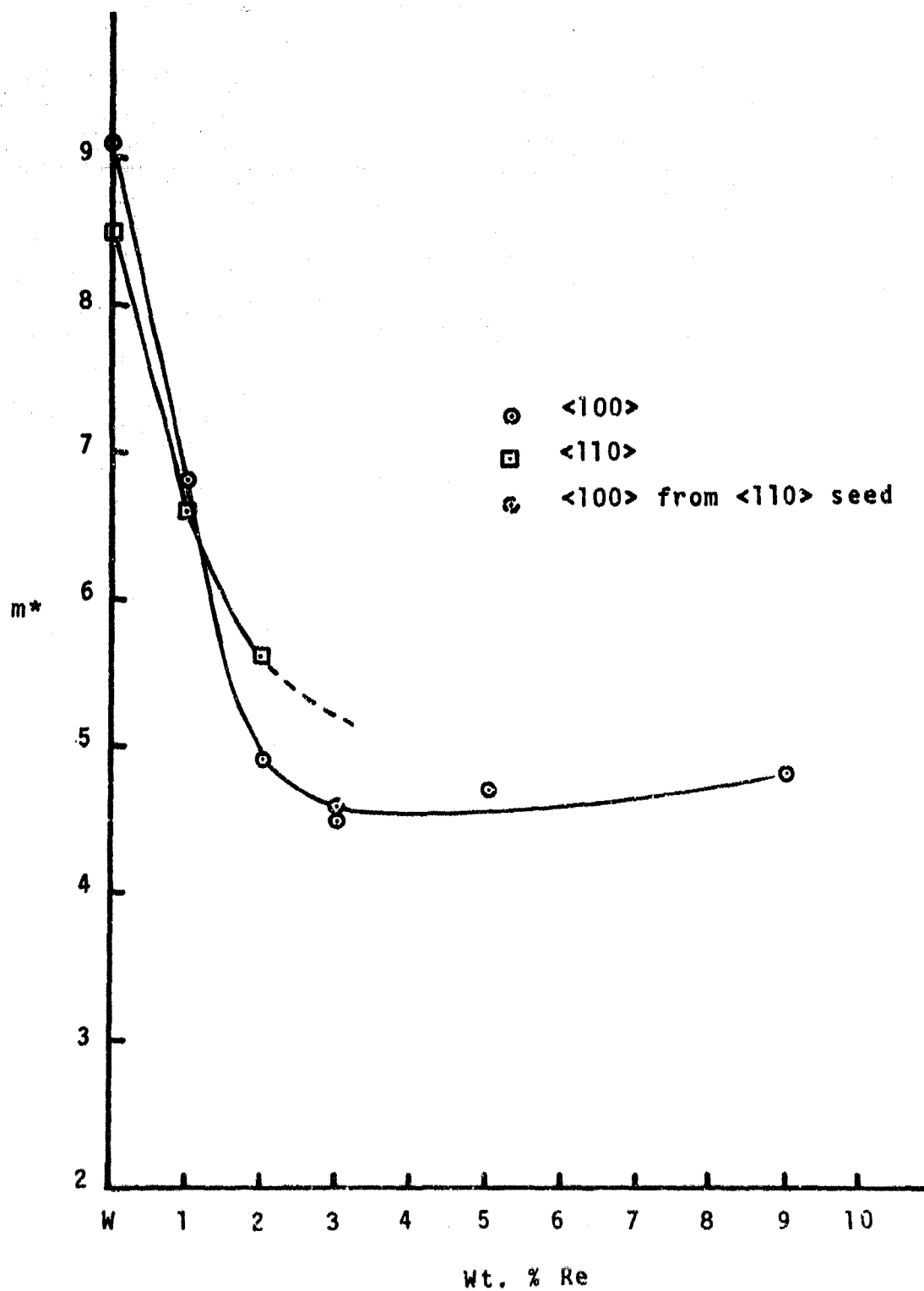


Figure 46. Effect of rhenium additions to tungsten on the dislocation velocity exponent, m^* .

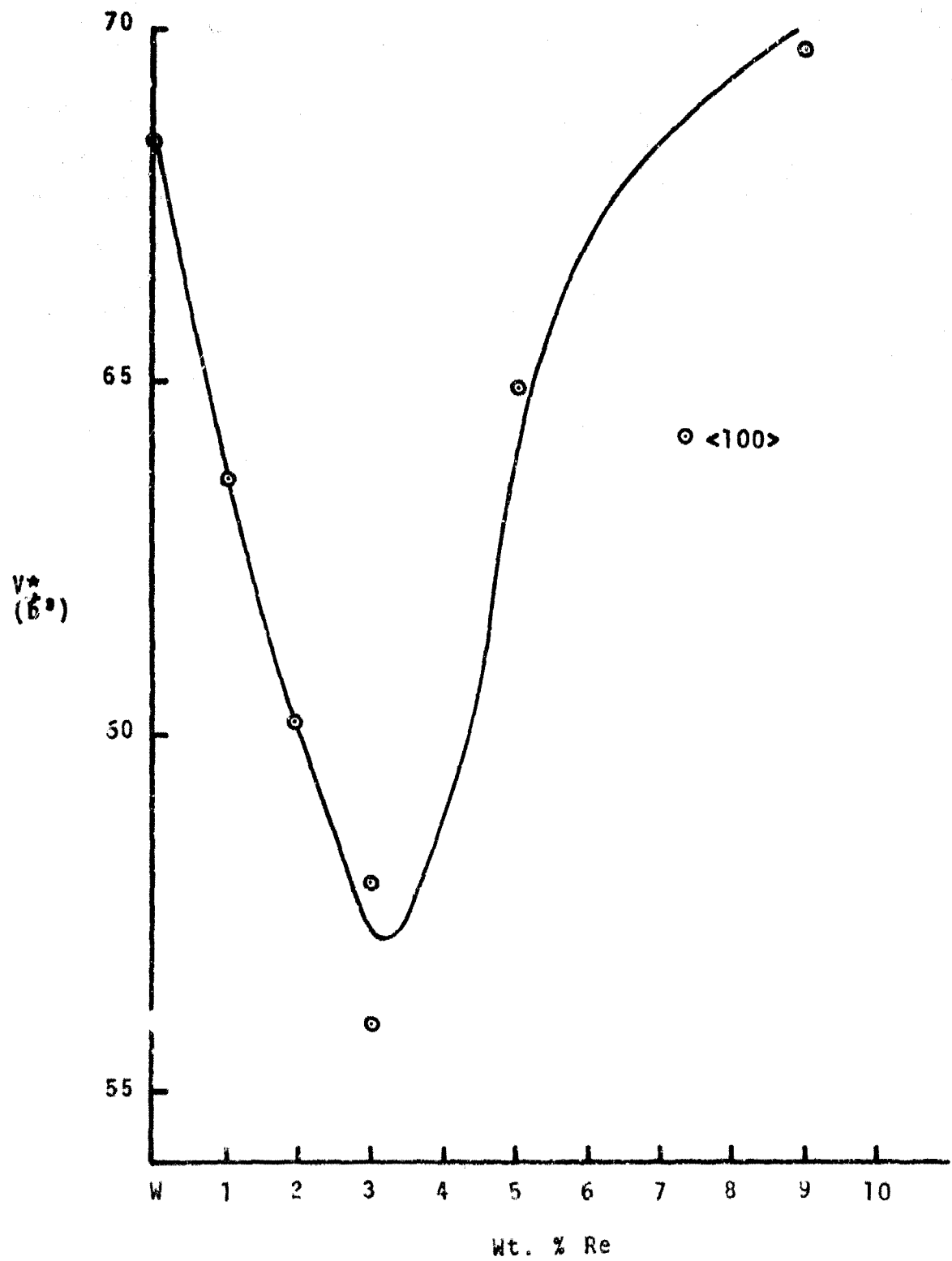


Figure 47. Activation volume changes with rhenium additions to tungsten.

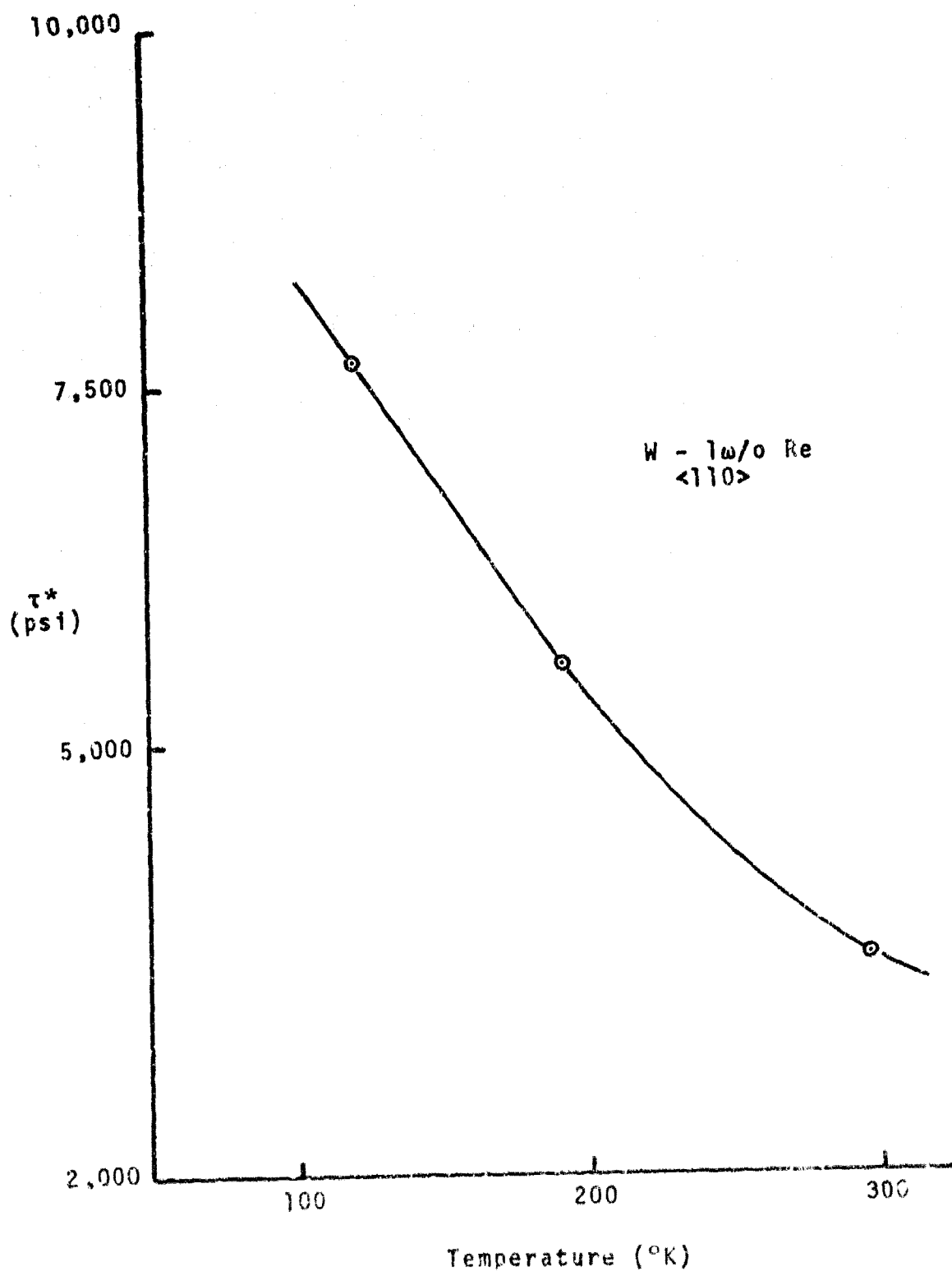


Figure 48. Variation in effective stress, τ^* , with temperature for <110> W-1w/o Re.

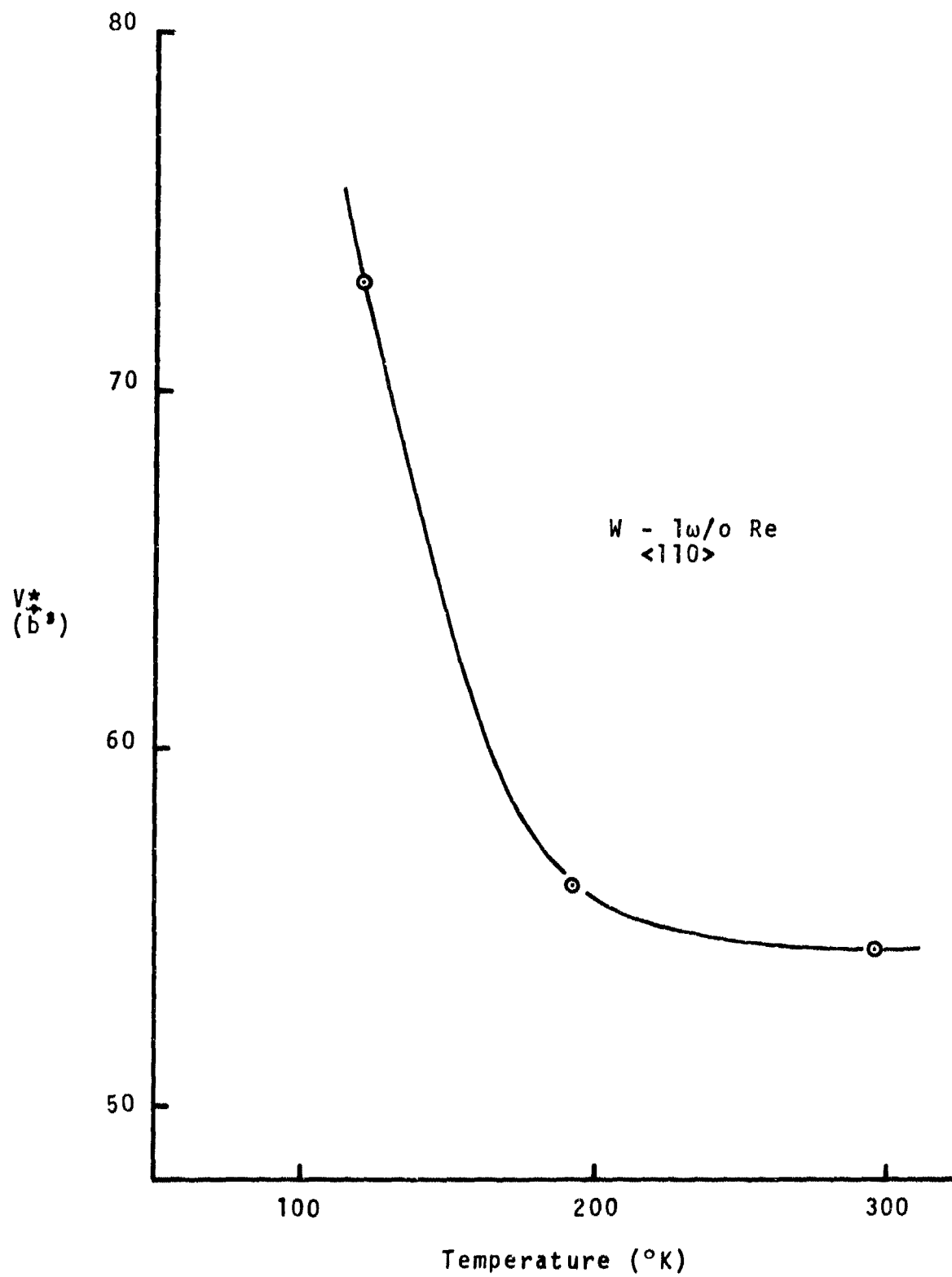


Figure 50. Change in activation volume, V^* , with temperature for $\langle 110 \rangle$ W-1w/o Re.

DISCUSSION

4.1 Rhenium Ductilizing Effect

The approach of this work was to consider the influence of carbon (interstitials) on the effects of rhenium in tungsten, as related to both deformation and fracture, and to study separately the effect of rhenium alone. The results to be discussed show that the relative importance of each element is dramatically different. Studies with the carburized material will be discussed first. The grain boundary segregation studies (AES and SEM) will be tied in briefly with the interstitial studies, but primarily treated separately since it explained an entirely different phenomenon: the effect of dope additions to tungsten and tungsten-rhenium alloys. Then the role of rhenium alone will be discussed and the results tied in with other work on solid solution softening in bcc alloy systems.

4.1.1 Role of Carbon (Interstitials)

In the body centered cubic (bcc) structure tetrahedral interstitial sites are larger and therefore lower in energy than octahedral sites. Consequently, small impurity atoms tend to occupy these tetrahedral sites. They are located mid-way between lattice sites on cube edges and mid-way between body center lattice sites at face centers. Since they are symmetrically located on the major axes, the interstitial sites are frequently referred to as x-, y-, and z-sites. Each site has equal energy giving each an equal chance of being occupied in an

unstrained lattice. When a bcc material is strained, however, certain sites become favored. If a tensile strain exists along the z-axis, the z-sites elongate while the x- and y-sites contract, as shown schematically, in Figure 51. The larger z-sites have lower energy and their occupancy is favored. Under this strained condition there is a redistribution of atoms occupying interstitial sites by diffusion of atoms from x- and y-sites to z-sites. The activation energy for this process is that of diffusion for the interstitial atom in the bcc lattice. Similarly a torsional strain in the x-y plane will cause a net flow of z-atoms into x- and y-sites. The amount of redistribution is dependent on the strain (distortion) in the lattice, the temperature, and the time it is applied.

When the strain is removed each site becomes equally favored again. If a redistribution occurred under strain it will leave an anelastic strain on unloading and time is required for a re-homogenization of site occupancy. The time for diffusion to equal site occupancy (i. e., anelastic strain decay) is dependent on temperature and the amount of redistribution required. By applying a constant stress in the temperature range where localized diffusion occurs in minutes, favored occupancy occurs and the rate of diffusion back to equal occupancy on removal of the stress can be measured by monitoring the anelastic strain decay. This is the approach of the elastic aftereffect technique. By taking anelastic strain decay measurements at different temperatures in this temperature region, the activation energy and diffusion coefficient for this process can be calculated.

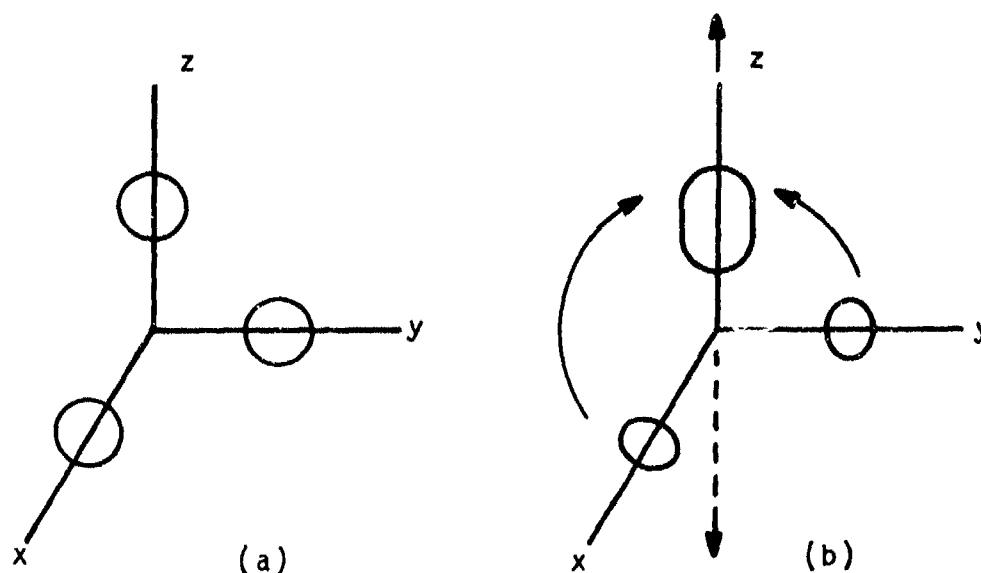


Figure 51. Schematic representation of tetragonal interstitial site distortion from the unstrained condition (a) to the strained condition (b).

The fact that no anelastic strain was produced by elastic aftereffect measurements in carburized tungsten and tungsten-rhenium alloys means that no significant carbon redistribution occurred to favored sites. This is surprising since chemical analysis showed large concentrations of carbon in these materials. After carburization it ranged from 120 ppm to 1250 ppm by weight. Actual atomic concentration is just over 15 times that amount.

Aging bcc materials under constant stress can cause an upper yield

point on subsequent loading. (An example of this is the work of Owen and Roberts⁽⁸⁴⁾ on iron-nickel-carbon martensite.) The stress increment $\Delta\sigma_y$ (Figure 38) is measured in those cases where stress reaches an upper yield value (σ_{uy}) before falling to the strain-hardening portion of the stress-strain curve. The upper stress is related to a decreased mobile dislocation density resulting from an interstitial-dislocation interaction. Both Snoek interaction and Cottrell atmosphere formation have been shown to cause this dislocation pinning⁽⁸⁴⁾. The Snoek locking occurs in relaxation times similar to the time required for a single jump of an interstitial atom while the Cottrell atmosphere pinning requires long-range diffusion. The activation energy for diffusion can be obtained in the second case from a plot of the logarithm of aging time to reach a selected value of Δ_y as a function of reciprocal temperature.

Yield drops are never found for iron-nickel-carbon martensite when the interstitial carbon concentration is too low, even after aging times sufficient for extensive long range diffusion⁽⁸⁴⁾. This condition exists with the carburized W/Re alloys tested in this work. While the carbon concentration of the W/Re alloys was quite high, both the elastic after-effect and stress relaxation experiments demonstrate the interstitial solubility is too low to produce an anelastic strain or noticeable dislocation pinning. The Owen and Roberts work showed that 30 ppm carbon was insufficient to produce the dislocation pinning effect, which was observed at 1200 ppm carbon concentrations. It is not known exactly

what interstitial concentration is required to produce a noticeable pinning in tungsten and tungsten-rhenium alloys, but it is greater than the solubility of carbon in these materials. It is highly unlikely, then, that interstitials are related to the increased ductility produced by rhenium in tungsten. Whatever their solid solubility in the alloy lattice, it is insufficient to seriously affect mobile dislocation density and, therefore, flow stress.

The carbon added to the alloys during carburizing must either be in interstitial solid solution or tied up in carbides. The photomicrographs, transmission electron micrographs, and the electron microprobe trace in Figures 24-29 represent efforts to identify carbides. The needle-like precipitates in Figures 25 and 26b are associated with high carbon concentrations. The W-25Re sample having the microstructure in Figure 25 had 1250 ppm carbon. Electron microprobe X-ray scans (Figure 27) show the carbon concentration in the outer case of the unalloyed tungsten sample shown in Figure 26 is at least twice that of the core. These results again demonstrate an association between the presence of the "precipitates" and a high carbon concentration. The microprobe results also show no significant differences between the large needle-like precipitates and the matrix material. This observation is not completely understood, but could indicate a finer unresolved precipitate exists in addition to the larger needles. The electron transmission micrograph in Figure 28 shows a finer but similar type precipitate in a W-5Re alloy. Most

replicated micrographs did not show this type of precipitate.

It is possible that the interstitial solubility was high enough that resolvable precipitates did not form in any number for the lower carbon concentration carburized alloys (~ 100 ppm). At increasing concentrations needle-like precipitates begin to form, and are quite distinct at 1000 ppm. This observation suggests that 100 ppm carbon is not sufficient to produce detectable anelastic strain or dislocation pinning during aging. The results of recent work⁽⁶¹⁾ with polycrystalline sintered tungsten billet material has suggested that phosphorus at grain boundaries is responsible for the brittle nature of tungsten. It could then be possible that rhenium would increase the solid solubility for phosphorus, removing it from grain boundaries and, thereby, increasing ductility. The Auger electron spectroscopy studies in this work were initiated to pursue this theory. By recrystallizing the drawn polycrystalline wire alloys, intergranular fracture could be achieved and grain boundary surfaces examined in situ. Phosphorus was never observed on any tungsten or tungsten-rhenium grain boundary surfaces although potassium was observed. It is not possible, then, to say what effect rhenium has, if any, on phosphorus solubility or distribution. The Auger technique also allowed the observation of the grain boundary oxygen and carbon concentrations. These were very low, of the order expected from contamination in the ultra-high vacuum conditions, and no systematic differences were noticed with rhenium content. It again seems highly unlikely that a decreased

grain boundary embrittlement by removal of phosphorus or other interstitials is an important part of the rhenium ductilizing effect.

4.1.2 Role of Rhenium

The deformation of bcc metals and alloys is a thermally activated process at temperatures below $0.25 T_m$. In this region the flow stress, τ , is expressed as

$$\tau = \tau^* + \tau_i \quad (4.1)$$

where τ^* is the thermal component of stress (effective stress) and τ_i is the long-range internal stress. Figure 52 depicts the situation schematically, although the relative values of each component are not to scale. The thermal component is considerably smaller than the internal stress, but it is this effective stress that must be overcome for slip to occur. The barrier responsible for this stress must be short range since dislocations are thermally assisted over it. A number of mechanisms have been proposed to explain the short range barrier, but it is now generally accepted that the lattice itself provides resistance or friction to dislocations due at least in part to the directional nature of bonding in the bcc lattice. The best mathematical model of the situation is known as the pseudo Peierls model⁽⁸⁵⁾ and the lattice friction stress is usually considered synonymous with the Peierls stress. Changes in a lattice which affect the bond angles and strengths will produce changes in the lattice friction stress. Alloy additions, such as rhenium in tungsten, which change the electronic structure (electron/atom ratio)

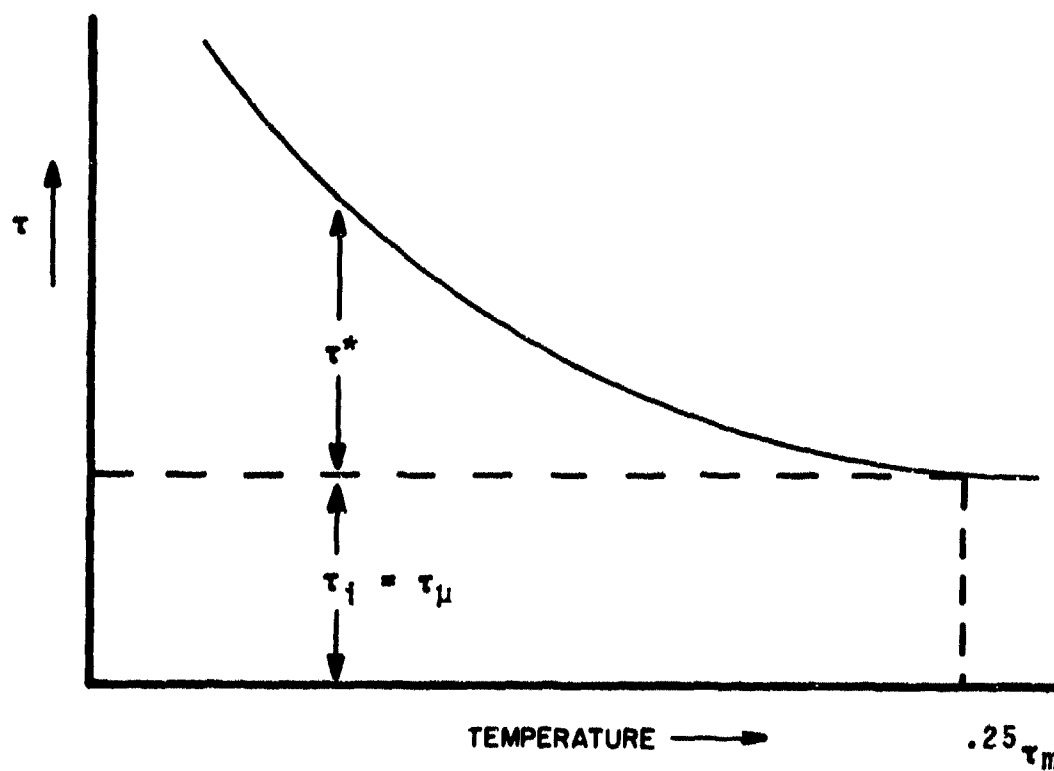


Figure 52. Schematic representation of flow stress below $0.25 T_m$ for a thermally activated deformation process.

are bound to have this effect. These changes may bring about an increase or a decrease in the lattice resistance to dislocation motion.

The long range stress field, on the other hand, is related to such things as grain boundaries, sub-boundaries, jogs, and anything in the lattice that will cause a dislocation pileup and back stress. A foreign substitutional atom will produce an elastic perturbation and, therefore, a stress field in the lattice related to its size misfit with the solute atom. This perturbation is a long range barrier and, since a substitution element can never occupy a lattice site without producing some local distortion, alloy additions will always increase the elastic interaction energy with dislocations. A difference in the elastic properties of the solute and matrix (alloy and pure metal) will modify the elastic interaction of dislocations with the solute elastic interaction effect and thereby affect the interaction energy (U_i). When the volume change due to introduction of a foreign atom is large, as with interstitial carbon in iron, the size misfit will dominate and the elastic interaction effect will be relatively small. For substitutional solute atoms, the elastic interaction effect may be significant since the volume change is relatively small. Rhenium is similar in atomic size to tungsten which would make the ratio of the volume change contribution to the different modulus contribution relatively low compared with other alloy systems. It was also shown in Figure 20 that rhenium reduced the modulus of tungsten. This small size effect and decreased modulus could account for the high rhenium concentration at maximum solid solution softening compared to other bcc alloy systems.

It has been suggested by Klopp, Stephens and Witzke^(17, 31, 32) on the basis of hardness measurements that rhenium additions to tungsten cause a decrease in the Peierls stress (τ^*). By alloying tungsten and molybdenum with various Group VII and VIII solutes in addition to rhenium, they showed the softening effect was related to solute electronic configuration, i.e., position in the periodic table. While these efforts have given indirect evidence, the results in Figure 44 are the first direct observation that rhenium does lower the Peierls stress and thereby ductilizes tungsten. The decrease in τ^* at 295°K is very rapid up to 3 w/o Re and continues more gradually up to 9 w/o Re. It is expected, as the hardness studies^(17, 31, 32) have shown, that the rapid decrease will continue at lower temperatures with the minimum occurring at lower rhenium contents for lower temperatures. Comparison of Figures 17 and 18 as well as 44 and 45 demonstrate the similarities in hardness and yield or flow stress measurements which supports the correlation made in the hardness studies.

In addition to demonstrating the mechanism of the rhenium ductilizing effect for dilute (up to 10 w/o Re) alloys, the single crystal strain rate cycling results show that rhenium alone is responsible. The small elastic zone in the unstrained EBZR crystal emphasizes the high purity of the electron beam zone refined crystals, as shown in the typical stress strain curves of Figures 40 and 41. This high purity is further evidence that

interstitial impurities do not play a role in the rhenium ductilizing effect, i. e., they do not affect τ^* , as the elastic aftereffect and stress relaxation experiments demonstrated.

4.1.3 Similarities with Solid Solution Softening

The addition of dilute concentrations of certain substitutional elements to iron and Group V elements will weaken the solvent metal. While there is some indication that an extrinsic mechanism is responsible in a couple Group V systems⁽⁴²⁻⁴⁸⁾, the overwhelming evidence is that the softening (weakening) is a result of a reduction in the Peierls stress^(8, 17, 18, 28-41). This is the same mechanism responsible for the rhenium ductilizing effect.

A list of alloy systems where softening has been demonstrated is given in Table XV. The behavior of these systems is essentially identical to tungsten-rhenium, only the range of solute is usually much lower. This is not surprising, however, when it is realized that solid solution softening is generally measured in terms of applied stress, equation (4.1). The flow stress, τ , will only decrease with solute additions as long as τ^* is reduced more than τ_i is increased. Since the atomic misfit between tungsten and rhenium is relatively small, increases in τ_i will not dominate as rapidly as in other alloy systems. In addition, the modulus is decreased and the different moduli contribution is important. In studying solid solution softening the solute effect on τ^* is not separated from the solute effect on τ_i . Figure 18 shows that alloy softening occurs up to 5 w/o Re while

TABLE XV

ALLOY SYSTEMS FOUND TO EXHIBIT SOLID SOLUTION SOFTENING

Solvent Element	Substitutional Solute	Interstitial Solute
Fe	Cr, Mo; Ni, Pt; Si, Ge	C; N, P
V	Ti; Mo	
Cb	Mo, W	O
Ta	Mo, W; Re	
Cr	Re	
Mo	Re	
W	Re	

the thermal component of flow stress τ^* continues to decrease up to 9 w/o Re (Figure 44). The increase in τ_i becomes greater than the decrease in τ^* above 5w/o Re. In some alloy systems, e. g., Ni in Fe, this change occurs at fractions of a percent solute.

All indications are that the rhenium ductilizing effect in dilute alloys is another example of solid solution softening in a bcc alloy system. In addition, the results of this work further support the idea that solid solution softening is a result of a reduction of the Peierls stress by the solute addition. Klopp⁽¹⁷⁾ has suggested that in addition to solid solution softening found in dilute tungsten-rhenium alloys (> 10% Re) the ductilizing effect observed in high rhenium concentration alloys is different from that at low concentrations. This difference does seem likely since increases in τ_i will dominate reductions in τ^* in the high solute range.

4.2 Source and Mechanism of Dope Effect

Any alloy that is used in a high-temperature application must exhibit both good room-temperature and high-temperature strength, creep resistance, toughness, fatigue strength, and corrosion and oxidation resistance⁽⁸⁶⁾. With lamp filament materials, the prevention of creep is perhaps the most critical problem that has to be faced. Creep resistance is necessary because any significant sagging of the filament, either due to its own weight or grain growth at high temperatures, is likely to result in premature fracture. Elements such as aluminum, magnesium, silicon and potassium are often added in compound form to pure tungsten and to tungsten alloys prior to sintering to provide the recrystallized grain structure (highly elongated) which offers this much-needed resistance to high temperature creep.

This work established the effects of these elements, interstitials and rhenium as functions of differing heat treatments and rhenium content upon the microstructure and fracture behavior of doped tungsten and tungsten-rhenium alloys. Auger electron spectroscopy (AES) has been shown to be effective in examining refractory metal surfaces fractured in situ in an ultrahigh vacuum environment⁽⁸⁷⁻⁹¹⁾. This technique provides a rapid and direct elemental qualitative analysis of the fracture surfaces without noticeably altering the physical or chemical make-up of the region under study. The Auger method yields valuable information regarding the segregation or depletion of either dopant elements, impurities or alloying

elements at fracture surfaces. By recrystallizing the alloys to get intergranular fracture, the distribution of these elements at grain boundaries was studied.

4.2.1 Auger Electron Spectroscopy

Previous work by Thomas and Haas⁽⁹²⁾ was aimed at providing more quantitative information on the surface elements constitution. The use of this technique assumes that the Auger peak-to-peak height (Figures 30 and 31) is a measure of the concentration of the surface species^(93, 94). In certain instances the chemical environment of the surface atoms can also be studied by this technique⁽⁹⁵⁾. The recent work of Thomas and Haas⁽⁹²⁾ has provided reliable experimental Auger calibration curves to adapt AES for quantitative analysis of alkali metals deposited on refractory metal substrates. This work included the case of potassium deposited onto single crystal tungsten surfaces. These calibration curves were obtained by depositing known amounts of various elements onto well-characterized substrates and monitoring the adsorbate/substrate Auger peak-to-peak height variation. Although the particular specimens in the present study were polycrystalline wires, the ratios of the adsorbate (potassium and other impurity elements) Auger peak height to the substrate (tungsten) Auger peak height is still meaningful. The use of adsorbate substrate peak height ratios should tend to minimize differences in the relative Auger yield between single and polycrystalline

material caused by different crystal faces (of varying atom density).

As demonstrated in Figure 30 and Table X the two tungsten peaks at 164 eV and 170 eV overlap. For this reason, the peak-to-peak height for the tungsten peak is taken as the height of the maximum positive deflection at 160 eV to the maximum negative deflection at 170 eV. The most prominent Auger peak for potassium occurs at 251 eV and it is this peak that was used in attempting to determine the approximate coverages of potassium on the fracture surfaces. The ratios of the appropriate potassium to tungsten peak-to-peak heights were calculated and the findings compared to the calibration curves in earlier results⁽⁹²⁾ to determine the approximate coverages shown in Table XI. The use of ratios also has the effect of discounting arbitrary experimental and instrumental parameters (e.g., beam voltage, sample current, electron multiplier gain, modulation voltage, etc.). Using adsorbate Auger peak heights alone as a function of coverage does not provide this advantage. Taking ratios yields more meaningful data, especially when attempting to compare results from different laboratories. This approach of course assumes that these variable parameters are kept constant during any one given Auger scan in a particular experiment. It is generally a good assumption.

It is interesting to note that potassium Auger peaks were found in the pure unalloyed tungsten material (class 1) both for the vacuum heat

treatment (at 2600°C) and for zone refining treatment (at 2100°C). The much lower K/W peak ratios for the class 1 material compared with classes 2 and 3 is consistent with the lower potassium bulk analysis in Table VIII. This lower potassium content is a result of the different doping compound chemistry* used in the welding rod material (class 1) than in the lamp grade tungsten powders used to make classes 2 and 3 alloys. The absence of potassium peaks is expected in the class 4 alloys since dope was not added during processing.

The dominant size of the potassium peaks on the intergranular fracture surfaces of doped alloys demonstrates that a large concentration of potassium is present on recrystallized grain boundary surfaces. The rapid disappearance of the peak with ion sputtering further indicates that it is highly localized on the grain boundary surfaces. The significance of this localization is only realized when considered in conjunction with the recrystallized grain microstructure and morphology.

4.2.2 Scanning Electron Microscopy

Several qualitative assessments can be made from examination of the scanning electron micrographs of the fractured alloy surfaces. The bubbles never occurred within grains. Examples of grains that fractured transgranularly are shown in Figures 34 and 37. The absence of bubbles from these fracture areas is conspicuous. These

*These dopants and techniques are not revealed by the supplier; they are highly proprietary items.

observations are consistent with the concentration profile Auger results, where the potassium peak height drops off rapidly as the grain boundary surface is removed by sputtering (Table XI). This result suggests that the bubbles are dragged along by grain boundaries during recrystallization. Without dope additions potassium bubbles do not form and recrystallization and grain growth is uninhibited. This is substantiated by the larger bubble free grains of the class 4 materials. Since it is more difficult for a propagating crack to go around these larger grains, transgranular fracture occurs more frequently in the class 4 materials.

Generally, the vacuum heat treated samples contained far greater numbers of slightly smaller bubbles (i. e., greater bubble density at equivalent magnifications) than zone refined samples. This difference appears surprising in light of the fact the VHT samples were subjected to a higher temperature (2600°C as compared to 2100°C for the EBHT specimens) for a much longer time. It seems reasonable that at the higher temperatures for very long times the smaller bubbles would migrate until two smaller bubbles intercepted each other and coalesced into a single larger bubble. Dawson⁽⁷⁶⁾ has shown, however, that bubbles in commercially doped tungsten grow considerably in size when subjected to a temperature gradient but do not grow during isothermal anneals, even under stress. The driving force for growth is the temperature gradient. The present results dramatically support this fact since the VHT was an isothermal anneal and the EBHT subjected the material to a severe

thermal gradient. While the EBHT fracture surface had slightly larger bubbles in some cases, their bubble area density was noticeably lower. As the electron beam zone moved up the rod during EBHT, the steep thermal gradient caused bubble migration. While the times of thermal exposure used by Dawson were much greater, the thermal gradients produced were not likely as severe. He also noticed increased randomness with bubble growth but comparisons could not be made between VHT and EBHT samples since all bubble morphologies were random.

Small additions of silicon, aluminum, and potassium have been added as compounds (known as dope) to tungsten for several decades to significantly raise the recrystallization temperature (several hundred degrees centigrade) and alter the recrystallized grain morphology of heavily drawn wire. The result is a unique interlocking recrystallized grain structure that gives greatly improved creep resistance (non sag lamp filaments) and superior toughness. The source of and reason for the dope effect in tungsten has long been a mystery.

Early ideas linked the doping effect with mullite ($3\text{Al}_2\text{O}_3:2\text{SiO}_2$) particles⁽⁷⁷⁾. This correlation was reasonable since the doping compounds contain both Al and Si. Shortly thereafter, Koo⁽⁷⁸⁾ and later Moon and Koo⁽⁷⁹⁾ and Das⁽⁸⁰⁾ concluded that the strings of "fine particles" observed in transmission specimens are not mullite, but are voids. They did not, however, establish the source of the voids although it was suggested that volatilization of the dope during sintering was responsible. The

possibility of residual doping elements at the surface of voids was unresolved.

The present work not only increases evidence that the dope forms voids or bubbles, but establishes the source of the bubbles. The scanning electron micrographs in Figures 33 through 37 are representative of bubbles found on all the recrystallized doped tungsten-rhenium alloys. The AES results in Table XI show clearly that these bubbles are coated with potassium. In no instance was aluminum or silicon detected on the fractured or bombarded surface of any sample examined in this study. Similar observations were independently made by Sell et al.⁽⁷⁵⁾ for pure tungsten. These workers used Auger electron spectroscopy, along with secondary-ion mass spectrometry and energy dispersive X-ray analysis and were able to correlate the absolute peak height of the potassium Auger peak with the density of bubbles of specified size in a given area. The bubbles form by the volatilization of potassium during sintering which is somehow trapped within the solid. While some of the potassium may escape, chemical analysis (Table VIII) and AES (Table XI) show a significant portion condenses on the surface of the bubbles and remains on cooling.

A number of observations in the present work on grain and bubble morphology in all doped tungsten-rhenium alloys (classes 2 and 3) after recrystallization and grain growth are consistent with the proposed bubble formation mechanism of Moon and Koo⁽⁷⁹⁾. The bubbles form in

the material during the sintering process and are elongated during subsequent wire drawing. The amount of working determines the shape change the elongated bubbles undergo on annealing. Those with length-to-width ratios less than ten spheroidize while those with length-to-width ratios greater than twenty are unstable and break up into a row of bubbles. As Figures 33 through 37 demonstrate bubble morphology was very random in all doped samples investigated. This indicates the wires were not worked sufficiently to produce unstable elongated bubbles that break up into rows. The bubble size, which is generally larger when compared to other observations of linear rows^(76, 79-82), further suggests the elongated bubbles spheroidized rather than breaking up into a row of bubbles on annealing.

Das⁽⁸⁰⁾ suggested that the stability of the rows is related to the stability of the filament. Moon and Koo's mechanism says the stability of the rows is related to the amount of working or bubble elongation prior to annealing. The critical characteristic of sag resistant filaments is the interlocking high aspect ratio grains formed on recrystallization. This structure typically forms in wires drawn to 0.030 inch diameter or smaller and always forms in wires 0.010 inch in diameter or less⁽⁸³⁾. It did not form in any of the 0.060 inch diameter doped wire examined in this work. While the recrystallization temperature was high, the recrystallized grain morphologies were always equiaxed (Figure 32). This equiaxed structure will not give the stable sag

resistance found with the interlocked grains. Consistent with this equiaxed structure is the observation that the bubbles are randomly distributed. While they pinned boundaries and raised the recrystallization temperature, the randomly distributed bubbles resulted in equiaxed grains. It takes rows of bubbles to control the recrystallization texture and give the interlocked elongated grains.

It seems likely that rows of bubbles will become apparent as the recrystallized grain morphology begins to become elongated and interlocked. The presence of bubbles alone is not sufficient to give the high creep resistant morphology. In addition to the dope additions, the production of a sag resistant wire requires a sufficient amount of working to produce unstable elongated bubbles that will break up into rows on annealing. It is these rows that are responsible for the interlocked grain structure.

SUMMARY AND CONCLUSIONS

For many years the roll of interstitial impurities has not been uniquely defined in tungsten and its alloys. A number of theories considered the interstitial impurities responsible in one way or another for the rhenium ductilizing effect in tungsten (detailed in Appendix I). A thorough combination of metallurgical research procedures in this work has shown that doping tungsten and tungsten-rhenium alloys with carbon has no noticeable effect on the results of any of the experiments, even after quenching the doped material into liquid tin from 2600°C. It must be concluded, then, that the solid solubility is so low that carbon is not a significant feature in the rhenium effect in tungsten. Similarly it is expected that oxygen and nitrogen solid solubilities will be too low to allow an effect. The insignificant interstitial effect suggests that rhenium alone is responsible for the ductilizing of tungsten.

Although phosphorus has been linked with the intergranular brittle behavior of pure tungsten⁽⁶¹⁾, Auger electron spectroscopy (AES) in this work eliminated a rhenium-phosphorus interaction as a possible ductilizing mechanism. In the few instances where phosphorus was present, there was no evidence that rhenium lowered the grain boundary concentration by increasing solid solubility.

Strain rate cycling experiments on high purity single crystal tungsten and tungsten-rhenium alloys showed that rhenium additions alone can

lower the thermal component of flow stress (Peierls stress). The dislocation dynamics, therefore, also points to the rhenium (rather than the combination of rhenium and interstitials) as being responsible for the ductilizing effect. This ductilizing effect is similar to solid solution softening in other bcc alloy systems which is generally believed to be caused by a lowering of the Peierls stress (Appendix I).

Recently Klopp and Witzke⁽⁹⁶⁾ and Stephens and Witzke⁽³¹⁾ have concluded, on the basis of hardness studies as a function of rhenium content and temperature, that the rhenium ductilizing effect is caused by a lowering of the Peierls stress, which is consistent with the results and conclusion of this work.

The dopants added to lamp grade tungsten powder before sintering retard recrystallization and growth and control grain structure in tungsten and tungsten-rhenium alloys. Recently a theory of bubble strengthening⁽⁷⁹⁾ has been proposed to explain this phenomenon. Scanning electron microscopy in this work confirms the presence of bubbles at grain boundaries; the Auger electron spectroscopy identified large concentrations of potassium associated with the bubbles. All the potassium was shown to be highly localized at grain boundary surfaces. This work confirms the fact that elemental potassium is entrapped within tungsten and tungsten-rhenium alloys, and forms bubbles during sintering and processing (probably by vaporizing within the solid) which restrict recrystallization and control the texture of grain growth. Studies of

bubble size and distribution demonstrate that the rows of bubbles are necessary to get the elongated, interlocked, recrystallized grain structure responsible for superior high temperature creep resistance and toughness. Bubble density differences with heat treatment show that a thermal gradient is necessary for bubble migration. This is in agreement with the work of Dawson⁽⁷⁶⁾.

The complete list of conclusions from this work follows:

1. The yield strength, ultimate strength and hardness of polycrystalline tungsten-rhenium alloys decrease with rhenium additions up to 5 w/o Re.
2. The solid solubility of carbon in tungsten and tungsten-rhenium is too low to affect dislocation dynamics. It is likely that other interstitials (N, O) will behave similarly.
3. Phosphorus is not present on grain boundary fracture surfaces of any alloy examined and, therefore, is not responsible for the rhenium ductilizing effect.
4. Rhenium alone lowers the Peierls stress of tungsten and is responsible for the rhenium ductilizing effect.
5. The rhenium ductilizing effect is another example of solid solution softening in a bcc alloy system.
6. In doped tungsten and tungsten-rhenium alloys, bubbles are responsible for the increased recrystallization temperature and recrystallized grain morphology.

7. The bubbles are coated with a surface layer of potassium. They form by volatilization of the potassium during sintering, are elongated during processing and spheroidize on annealing.

8. Randomly distributed bubbles will raise the recrystallization temperature but will not control recrystallization morphology to give elongated interlocked grains. Rows of bubbles are necessary for this and they only form after a critical amount of deformation or wire reduction.

9. The thermal gradient during electron beam heat treatment caused some bubble migration with the beam as it passed along the rods. This gradient is necessary for bubble migration and coalescence during annealing.

APPENDIX I
A REVIEW OF THE RHENIUM DUCTILIZING EFFECT
AND ITS RELATION TO SOLID SOLUTION SOFTENING
IN BCC ALLOYS

For some time it has been known that the addition of rhenium to tungsten decreases its ductile to brittle transition temperature (DBTT). Although this phenomenon has received considerable attention and extensive experimental data has been accumulated, no completely satisfactory explanation of the effects of rhenium in these alloys has yet been obtained. This investigation examines the effect of rhenium on both plastic deformation and fracture behavior since changes in either or both of these properties will effect the DBTT. An extensive review of past experimental work follows as an introduction to the present program.

Rhenium Ductilizing Effect

The first indication that rhenium additions increased the ductility of tungsten and molybdenum was reported by Geach and Hughes at the First Plansee Conference in 1955⁽¹⁾. Processing studies with arc-cast button ingots of 30-35%Re alloys demonstrated excellent cold-rollability to strip for the Mo-35Re composition and unusually good hot rollability, at unspecified temperatures, for the W-30Re alloy. These results were confirmed by Jaffee, Sirius and Harwood⁽²⁾ who identified the composition

region of good workability of arc-cast alloys, by direct flat rolling, at rhenium concentrations of 20-40 a/o in the Mo-Re system and 26-30 a/o in the W-Re system. In this and subsequent work⁽²⁵⁾ the softening and recrystallization behavior and room- and elevated-temperature tensile properties of the Mo-35Re and W-30Re alloys were first reported. At the same time, Savitskii and Tylkina^(3, 97-100) attempted to improve compressive ductility of molybdenum with rhenium additions. Their early efforts were unsuccessful, but subsequent studies⁽³⁾ showed that arc-cast Mo-Re alloys containing up through 37% Re could be hot forged to 25% reductions by preheating them to 1200°C. Higher rhenium content alloys were brittle and not capable of hot plastic deformation. Ten years of unusually intensive exploration of the "Rhenium Ductilizing Effect" ensued by Jaffee and co-workers at Battelle Memorial Institute and Savitskii and co-workers in the USSR.

The earliest theories of this effect^(2, 25) were discussed in some detail by Jaffee, Maykuth and Douglass⁽¹⁰¹⁾. Similar explanations for these ductilizing effects were also believed to apply to chromium and molybdenum with rhenium additions⁽⁴⁾. It was believed that rhenium additions produced a more complex oxide with greater surface tension in all Group VI metals. Instead of wetting grain boundaries, the oxide then agglomerated into round globules giving the alloy high intergranular strength and considerable ductility, even at 300 to 500 ppm oxygen for molybdenum. Pure molybdenum required less than 5 to

10 ppm to be ductile. Similarly increased tolerance for carbon or nitrogen was not observed⁽²⁵⁾. In another case⁽⁴⁾ fabricability at 1200° to 1250°C was possible for Mo-35Re at least to 250 ppm oxygen while 70 ppm nitrogen or 18 ppm carbon rendered the alloy incapable of direct hot fabricability.

At the same time interstitial solubility (chiefly oxygen) was thought to be lowered by rhenium additions, explaining the failure of these alloys to exhibit yield-point behavior. The contribution of valence electrons from rhenium to the VIA solute lattice was believed responsible for the reduced solubility^(102, 103). Initial decreases in hardness of molybdenum with the addition of rhenium was interpreted as evidence for the reduced interstitial solubility.

Twinning effects have been found during tensile deformation of Mo-Re^(4, 104, 105) and W-Re⁽¹⁰⁴⁾ alloys. They resulted in serrations in stress-strain curves similar to the discontinuities caused by interstitial locking. The yield point was attributed to an audible burst of twins as the critical twinning stress was exceeded for Mo-20 to 35 a/o Re. The addition of rhenium to molybdenum and tungsten was found to raise the slip-to-twinning transition temperature, T_d , and lower the DBTT in the twinning region, changing significantly the plastic deformation mechanism. The amount of twinning increased both with rhenium content and decreasing test temperature. This is due to rhenium reductions in stacking fault energy as suggested by Lawley

and Maddin⁽¹⁰⁶⁾, Votava⁽¹⁹⁾, Aqua and Wagner⁽¹⁰⁷⁾, and by Davidson and Brotyen^(105, 108, 109), and to the lack of temperature sensitivity of the critical twinning stress⁽⁴⁾ compared to the flow stress which is very temperature sensitive at lower temperatures for bcc alloys.

Grain boundaries in some chromium-rhenium alloys were found to contain a eutectic-type structure surrounded by a Re-rich region⁽¹⁶⁾. This phase was considered to contribute to the alloy strength by resisting the propagation of small cracks which may develop in the precipitate-metal interface during the fracture process.

In summary, early studies indicated the ductilizing effects of rhenium resulted from:

- 1) A change in intergranular oxide morphology and/or composition.
- 2) A reduction in the solubility of interstitial impurities (chiefly oxygen).
- 3) A reduction in the stacking fault energy resulting in easier twinning.
- 4) A continuous eutectic-like grain boundary phase, accompanied with local rhenium segregation.

During the development of the early theories a wealth of interesting phenomenological and property observations was obtained (e. g., References 5, 6, 111, 114-120, 124-126, 129, 131, 133, 138-142) in an effort to shed more light on these mechanisms. Particular emphasis

was placed on evaluating the effect of rhenium additions on electronic structure^(11, 110-114), interstitial solubility, motion and morphology (5, 6, 14, 114-120), deformation mechanisms, particularly twinning behavior⁽¹²¹⁻¹²⁵⁾, interfacial energies^(9, 10, 126), fracture behavior (5, 6, 119, 120, 127-129), recrystallization and ductile to brittle transition temperatures⁽¹²⁹⁻¹³⁶⁾.

Hypothesis 1) above is now generally considered unimportant to the rhenium ductilizing effect since cracks in Group VIA metals are frequently initiated in clean regions of grain boundaries and propagate by intragranular cleavage⁽⁵⁻⁷⁾. The tendency to intergranular failure increases with rhenium content, as demonstrated in tungsten-rhenium alloys by Raffo⁽⁸⁾. Numerous studies^(7, 9-15) have not only failed to substantiate the decreased interstitial solubility hypothesis, but in many cases showed this to be incorrect⁽¹²⁻¹⁵⁾ and in some cases showed the opposite situation to be true^(14, 15). It is now an accepted fact that rhenium increases interstitial solubility in Group VIA metals. The occurrence of a grain boundary eutectic-like phase and accompanying local rhenium segregation has received little further attention since its early proposal⁽¹⁶⁾. It was noticed in all three Group VIA alloys, but only at rhenium concentrations close to the solid solubility limit (Cr-35Re, Mo-35Re, W-25Re). It seems likely then that a sigma phase, formed in the grain boundary of these alloys, accounts for local chemical and microhardness

inhomogeneities. This unique situation, combined with the lack of any further evidence of the phenomenon, also eliminates it as a possible controlling mechanism. Allen^(9,10) also showed that rhenium has no significant effect on surface tension of Group VIA metals. These observations are in direct opposition to the effect of the proposed change in grain boundary precipitate morphology.

It is well established that rhenium promotes twinning in Group VIA alloys. At high solute concentrations the initial deformation of the ductile alloys is accompanied by twinning at temperatures below $0.25 T_m^{(17)}$. The twinning only accounts for a minor fraction of the observed total deformation, usually at the onset of macroscopic strain, with slip accounting for the remainder. Consequently, the importance of twinning to the rhenium ductilizing effect is still not well understood.

In 1962, Lawley and Madden⁽¹⁰⁶⁾ showed that low-temperature deformation occurred by slip on the $\{110\} \langle 111 \rangle$ system for single crystals of molybdenum containing from 6 to 39 a/o rhenium. Twinning occurred readily in the 30 a/o Re alloy on the $\{112\} \langle 111 \rangle$ system. Several investigators have observed slip emanating from tips of $1/6 \langle 111 \rangle \{11\bar{2}\}$ twins terminating inside a crystal⁽¹⁹⁻²⁴⁾. Gilbert and Allen⁽⁵⁾ have shown that failure in Cr-Re alloys frequently follows twin/matrix interfaces. Stephens and Klopp⁽¹⁸⁾, however, suggest twinning is important in relieving localized stress concentrations which might otherwise have led to fracture. In their mechanism, twinning

arises from a stress-assisted precipitation of sigma phase from a metastable solid solution.

Klopp⁽¹⁷⁾ has proposed that there is a distinct difference between the rhenium ductilizing phenomenon observed at high rhenium concentrations, the rhenium ductilizing effect (above 20 a/o Re), and that at low rhenium concentrations, the solution softening effect (less than 10 a/o Re). The lowered ductile-brittle transition temperature in near-saturated Group VIA-Re alloys is not specific to rhenium but is also found in alloys with other solutes from Group VIIA and the early portions of Group VIIIA. The ability of a solute to promote the (rhenium) ductilizing effect is related to its position in the periodic table. Several rhenium analog alloys have been identified for Cr and are probable for Mo and W. Their identification was based on similarities in electron to atom ratios, phase diagrams (including an intermediate sigma phase and moderately high solid solubilities) hardening rates, and propensity for twinning, all of which are related to the position of the solute in the periodic table.

Phase diagrams for chromium, molybdenum and tungsten with Group VIIA and VIIIA elements indicate two trends regarding solubility. The major trend is a decrease in solid solubility with increasing number of s and d valence electrons. This is consistent with Robbins theory^(102, 103) which predicts decreasing solubility as the average electron to atom ratio increases above 6. A minor trend is for solutes

to have their highest solubility in the Group VIA element from the same period, probably due to size effects. The effectiveness of solutes in promoting twinning appears to vary with the solute to solvent relation similar to that governing solubility. Twinning does not necessarily occur near the solubility limit as in the case of Cr-Mn and Cr-Fe alloys. At low temperatures Cr-Re alloys twin at rhenium concentrations well below the solubility limit. This is a further indication that twinning is associated with a factor other than the impending appearance of a new phase, which is inconsistent with the earlier ideas of Stephens and Klopp⁽¹⁸⁾. Twinning does appear to be a function of temperature and solute electronic structure similar to those that govern solubility rather than on solubility itself.

Although the mechanism of the rhenium ductilizing effect is still not understood, important conclusions can be drawn from trends in the extensive collection of information now available. The periodic position of the solute is of fundamental importance in controlling the properties of Group VIA systems alloyed with solutes from Group VIIA and VIIIA. This factor influences the solubility relations, appearance and location of the sigma phase, hardening, twinning, and most likely the improved ductility associated with the rhenium ductilizing effect. The correlation of all these effects reflect the probability that each is controlled by the electronic features of the solute rather than being directly interrelated. It is interesting to note that the rhenium

ductilizing effect is limited to Group VIA alloy systems. Both Cb-Re and Ta-Re systems, which contain sigma phases, do not exhibit the rhenium ductilizing effect⁽²⁵⁻²⁷⁾.

Superplasticity has been observed in three systems (Cr-Co, Cr-Ru, and W-Re) which show the rhenium ductilizing effect. Its role is not known, but it is expected in other rhenium ductilizing effect alloy systems based on phase-relation similarities⁽¹⁷⁾. It has been suggested that superplasticity is associated with the apparent solute segregation to grain boundaries in Cr-Re and Mo-Re^(143, 144). This solute segregation, however, has not been well documented; it was very slight, highly localized, and has not been reproduced anywhere in the literature.

Solid Solution Softening

The interesting difference between low and high rhenium concentrations in Group VIA alloys is the alloy softening which occurs only for dilute alloys, while both have lower ductile to brittle transition temperatures. It is promoted by Group VA and VIA additions to Group VIA solvents as well as by Group VIIA and VIIIA additions. The major trend, similar to that for solubility and twinning, is for the solute content at the hardness minimum (maximum softness) to decrease with increasing number of s and d electrons. A minor trend is for this necessary solute concentration to increase with increasing period number. The solute content at the hardness

minimum is expected to be highest for rhenium and lowest for nickel in Group VIA elements⁽¹⁷⁾. This solid solution softening phenomenon is common in many other bcc transition metal alloy systems at low temperatures and low alloy concentrations.⁽¹⁴⁵⁻¹⁴⁸⁾ It has been observed in vanadium^(149, 150), columbium^(27, 40, 42-45, 47, 151), tantalum^(26, 28, 38, 41, 46, 47), chromium^(7, 15, 18, 137, 138), molybdenum^(32, 105, 106), tungsten^(8, 17, 29, 152-162), and iron^(34-37, 39, 163-172). Leslie et al. suggest alloy softening can be produced by any solute addition in bcc metals at some combination of concentration, temperature, and strain rate⁽³⁷⁾. It has been noted by Clark⁽¹⁶⁵⁾ that this softening also occurs in the alkali halides, and the Group IV semiconductors.

Solid solution softening is characterized by a decrease in the temperature and strain-rate dependence of yield or flow stress in the temperature range where these stresses increase rapidly with decreasing temperature. The assumption is made that the flow stress (σ) is separated into two parts, a thermal component (σ^*), called the effective stress, and an athermal component (σ_μ or σ_i), called the internal stress, thus

$$\sigma = \sigma^* + \sigma_i .$$

The athermal component, σ_i , generally follows simple size and modulus effect rules which require hardening on addition of a second

element. That is, the long range stress field increases with solute additions, but does not vary significantly with temperature. It dominates above homologous temperatures of about 0.2. Solute additions may either raise or lower the thermal component, σ^* , of flow stress which increases rapidly with decreasing temperature below 0.2 Tm. Solid solution softening is attributed to a decrease in σ^* caused by the presence of solute atoms. In such cases the solute reduction of σ^* is greater than the increase in σ_1 . This phenomenon has received considerable attention in recent years and is reviewed in detail by Arsenault⁽¹⁷³⁾, Christian⁽¹⁷⁴⁾, Leslie⁽³⁶⁾, and Wolfson and Clark⁽¹⁷⁵⁾.

There is some disagreement whether the explanation of solution softening is intrinsic or extrinsic in origin. Some investigators consider that it arises from effects on the inherent difficulty of moving dislocations in a bcc lattice (intrinsic), while others believe that it results from the loss of interstitial interaction with dislocations (extrinsic). Three general intrinsic and one extrinsic mechanism have been proposed:

1. Reduction of lattice friction (Peierls-Nabarro) stress,
2. Enhanced sessile-glissile transformations of screw dislocations,
3. Increase in mobile dislocation density,
4. Solute association (scavenging) processes.

Most substitutional alloy softening is considered caused by a reduction of the Peierls stress. This mechanism has recently been considered responsible for the rhenium ductilizing effect in Group VIA elements^(17, 18, 28-33), but in these cases alloy softening does not occur at high rhenium concentrations^(31, 32). This could be the result of a different phenomenon at high solute contents, with a separate controlling mechanism as suggested by Klopp⁽¹⁷⁾, or a natural extension of the increased solute contribution to σ_i becoming greater than the reduction of σ^* . Wolfson and Clark have reported solution softening, defined as a reduction in σ^* with solute additions, in Fe-Ge up to 8.3 a/o Ge despite the fact that alloys above 2 a/o Ge are considerably stronger than pure iron at all temperatures down to -196°C . They also showed that the reduction of σ^* increases with increasing Ge content, up to the maximum concentration investigated (8.3 a/o Ge) although all alloys containing more than 2.0 a/o Ge exhibit normal alloy hardening.

Solute additions can lower the Peierls stress by reducing the shear modulus or by locally enhancing kink nucleation due to solute-induced elastic interactions, lattice disorder, and interatomic bond modifications, all of which tend to "smear out" the dislocation core⁽¹⁷⁵⁾. Although Arsenault⁽¹⁷³⁾ showed that modulus considerations could explain softening in Ta-Nb alloys, Gamble⁽³⁹⁾ showed that modulus changes are frequently too small to account

for the effect and softening can even be accompanied by modulus increases⁽¹⁷⁶⁾. This suggests the more probable double-kink mechanism of overcoming the Peierls stress as the solute effects the ease of kink formation.

The thermally activated sessile-glissile transformation of screw dislocations has been proposed to explain the temperature dependence of the yield and flow stress in bcc systems^(170, 177, 178) and extended to alloy softening as well^(171, 172). Both the temperature dependence of cross slip and the low temperature asymmetry of yielding in bcc metals have been attributed to spontaneous dissociation of screw dislocations into sessile configurations of partials^(179, 180). For such an extended screw dislocation to cross slip it must first recombine by some thermally activated process. Friedel has proposed such a mechanism for cph structures⁽¹⁸¹⁾. In this case the idea is that solute atoms near a dissociated screw dislocation facilitate the constriction of partials. This makes it easier for low-energy sessile configurations to transform to higher energy glissile configurations by decreasing the energy difference between them. The asymmetry of yielding in bcc metals occurs because the applied stress can either assist or oppose this transformation.

Since there is no evidence for pronounced dislocation dissociation in bcc metals this mechanism is considered quite speculative⁽¹⁷⁵⁾. Christian does not even mention it in his review of the subject⁽¹⁷⁴⁾.

Calculations indicate that the equilibrium separation of the partials is so small that they have little physical reality. Thus, Kroupa and Vitek⁽¹⁸²⁾ interpreted the extended configuration as an approximate description of the core structure of the dislocation. This was done by Dorn and Mukherjee⁽⁸⁵⁾, also, who generalized the Peierls mechanism for thermally activated deformation to include the effects of an asymmetric dislocation core. The pseudo-Peierls model develops an alternative explanation for cross slip and asymmetric yielding. While it is not yet possible to distinguish between this and the original recombination model⁽¹⁸³⁾, both can be treated as special cases of the double-kink mechanism, where the solute promotes screw segments of double kink size which can then cross slip.

Nakada and Key⁽¹⁶⁹⁾ found that the CRSS of purified iron is higher than Fe-N crystals between 100-200°K. They suggested this was due to a greater mobile dislocation density in the alloy crystals than the purified iron. A specific model for the increase in mobile dislocation density was proposed by Christ et al.^(163, 164, 167). It depends on interstitial impurity-induced cross slip. Elastic interaction forces exerted by stationary interstitial dipoles on screw dislocations may promote cross slip leading to dislocation multiplication as described by Low and Guard⁽¹⁸⁴⁾. Christ et al. noted the rate of softening per a/o solute was about 30 times greater for Fe-N than Fe-Ni alloys and attribute the Fe-Ni softening to reductions in the Peierls stress, while

the Fe-N softening was due to interstitial induced cross slip. Slip line traces in the work of Nakada and Key⁽¹⁶⁹⁾, however, indicated that cross slip is more difficult and slip is more crystallographic in Fe-N alloys than in purified iron. While both mechanisms 2 and 3 involve cross slip of screw dislocations, they are distinct proposals. The effect of 2 could be to increase dislocation density as described in 3, but the latter model makes no assumptions regarding dislocation dissociation. In his review of the subject for the 1971 Campbell Memorial Lecture, Leslie⁽³⁶⁾ concluded that the weight of evidence favors an intrinsic origin for the temperature dependence of the yield stress in iron. The Spitzig and Leslie⁽³⁵⁾ data provided no support for the interstitial hardening theory and showed that the temperature dependence of the yield stress in iron is increased rather than decreased by gettering of interstitial impurities^(34, 164, 168, 169). Christ et al.⁽¹⁶³⁾ also show that alloy softening is a dynamic flow phenomenon rather than a static yield phenomenon. Its origin is related to thermally activated dislocation mechanisms of plastic deformation. This still allows for the interstitial scavenging mechanism, assuming hardening occurs by dislocation interstitial interaction. There is evidence that the temperature dependence of yield and flow stress in bcc metals arises from the thermal activation of mobile dislocations past residual interstitial atoms⁽¹⁸⁵⁻¹⁸⁷⁾. The removal of interstitial carbon, nitrogen, and oxygen has been shown to result in significant reductions

of the thermal component of flow stress^(44, 188-194). Allen and Jaffee⁽¹³⁸⁾ proposed that alloying can remove interstitials from solution in two ways:

1. The solute can form a compound with the interstitials.
2. The solute can promote the formation of solvent-interstitial or interstitial-interstitial compounds.

Smialek et al.⁽¹⁸⁹⁾ have also proposed the formation of large ordered complexes which reduce the effective concentration of the new solute species and the interstitial species.

Evidence for the scavenging mechanism is presented by Smialek et al.⁽¹⁸⁹⁾ in Ta-Re where no softening occurs for pure Ta-Re or rapidly quenched Ta-Re-N crystals. Slowly cooled Ta-Re-N, however, shows a minimum in the yield stress-Re composition curve near 1.3 at/o Re and the minimum corresponds approximately to the yield stress of pure tantalum. Similar effects have been observed in Nb-Mo where alloy softening was observed relative to electron beam zone-refined niobium crystals, but not relative to ultra high vacuum (UHV) annealed niobium⁽⁴⁸⁾. The same behavior has been observed in Ta-Re-N and postulated in Nb-W-O by Gibala and co-workers^(43, 46, 47). The latter group claims that, in general, alloy softening is not a reversible phenomenon, since softening is observed when interstitials are added to outgassed niobium but not when interstitials are removed⁽¹⁸⁸⁾, and it is limited to only a few interstitial alloy systems (Fe-N, Fe-C,

Nb-O). It has also been found in Fe-P⁽¹⁹⁵⁾. If it were an intrinsic effect they claim it should be reversible and occur in virtually all interstitial systems. Christian⁽¹⁷⁴⁾ has shown that the procedure used to show the process is irreversible is wrong. He further noted, in his extensive review of bcc plastic deformation, that while scavenging effects very probably exist, there is generally no softening at high temperatures. It is necessary then to postulate a temperature-dependence of the relevant dislocation-interstitial interaction. He concluded that the most probable cause of alloy softening was intrinsic, i.e., either mechanism 1 or 3. Many investigators have argued against the solute-interstitial association mechanism as the cause of softening, and the work of Lahiri and Fine⁽¹⁹⁶⁾ showed that removal of C and N from their Fe alloys reduced only the athermal component, σ_1 , of flow stress. This is consistent with the SSH theories that predict a temperature-independent alloy hardening [Mott-Nabarro⁽¹⁹⁷⁻¹⁹⁹⁾, Schoeck-Seeger⁽²⁰⁰⁾, and Friedel^(201, 202)]. The SSH theories that predict a very strong temperature dependence of alloy hardening^(185-187, 203, 204) predict a stronger temperature dependence of CRSS for alloys of higher solute concentrations. This trend was not observed by Nakada and Key⁽¹⁶⁹⁾ suggesting that solute atoms are not responsible for the characteristic, steep temperature dependence of CRSS in iron and its alloys. It is interesting to note that interstitial scavenging systems have only been identified for Group V A

alloys. Leslie and colleagues^(37, 205, 206) have shown that the strong temperature dependence of strength persists as interstitial concentrations approach zero in titanium-scavenged iron. In addition, solid solution softening occurred in essentially interstitial free iron.

The four mechanisms of alloy softening (Page 120) can be reduced to three since 2 is a special case of 1 once dislocation dissociation is considered limited to the core region. Most investigators consider the interstitial gettering mechanism is incorrect. While there is strong evidence this effect exists in some Group V A alloys it has not been found in Group VI A alloys and the effect is even reversed in some iron alloy systems. Dislocation interstitial interaction is not believed responsible for the strong increase in σ^* with decreasing temperature for bcc structures. The dislocation multiplication mechanism has had no significant critical review in the literature and there is no direct evidence for considerable dislocation multiplication with certain solute additions. The dislocation density immediately after macroscopic yielding (0.2% plastic strain) is the same in pure iron and Fe-N alloy crystals (about $5 \times 10^8 / \text{cm}^2$)⁽¹⁶⁹⁾. It is generally accepted that the temperature dependence of the Peierls stress is responsible for the high temperature dependence of the effective stress, σ^* , in bcc materials below $0.2 T_m$. It is a natural extension of this for alloy softening to be caused by solute reductions in the effective Peierls barrier at low temperatures. This is believed

to be the mechanism in most solid solution softening alloy systems.

A possible compromise situation may exist. Mordike and colleagues^(207, 208) found that each theory alone could not explain all the experimental observations in tantalum alloys. They consider deformation is controlled by a unique lattice mechanism where the thermal activation is influenced very strongly by interstitial foreign atoms. They studied Ta, Ta-Mo, and Ta-Re single crystals from 77°K up to 2000°K in both tension and compression. There was a complicated concentration dependence of the change in shear stress with alloy additions that suggest an interaction between interstitial and substitutional foreign atoms. The effect of solute additions on flow stress is dependent on crystal orientation and the type of loading, i. e., the orientation dependence in tension is quite different from that in compression. This observation is not consistent with the idea that the direct interaction between interstitial atoms and dislocations alone determines the deformation mechanism since the getters influenced compression and tension in the same way. A mechanism peculiar to the lattice would predict this behavior and is believed primarily rate controlling while a gettering process is also envisioned to neutralize the direct interaction of interstitial atoms with dislocations.

The "Rhenium Ductilizing Effect" has progressed through many stages of understanding since its discovery sixteen years ago⁽¹⁾.

The recent work by Klopp, Wityke, Stephens, Raffo and Garfinkle at NASA Lewis Research Center demonstrate the correlation of this effect with solute electronic structure. Klopp⁽¹⁷⁾ also showed that the magnitude of the softening effect varies systematically with the position of the solute in the periodic table. For a more thorough understanding it is now necessary to consider developments in solid solution softening of bcc alloy systems in conjunction with the rhenium ductilizing effect in Group VIA elements.

APPENDIX II

ACTIVATION VOLUME CALCULATION

It is customary to define activation volume as

$$V^* = - \frac{dH}{d\sigma^*} \quad (1)$$

where H is activation energy and σ^* is the thermal component of applied stress. For thermally activated deformation

$$\dot{\epsilon} = A_i e^{-\left(\frac{\Delta G_i}{kT}\right)} \quad (2)$$

where A_i is a constant structure factor, G_i the free energy, k is the Boltzman constant, and T is absolute temperature. Rewriting (2),

$$G = -kT \ln (\dot{\epsilon}/A) \quad (3)$$

$$G = H - TS \quad (4)$$

Combining (3) and (4)

$$\frac{dH}{d\sigma^*} = kT \left[\frac{\partial \ln (\dot{\epsilon}/A)}{\partial \sigma^*} \right]_T \quad (5)$$

From (1) and (5)

$$V^* = kT \left[\frac{\partial \ln (\dot{\epsilon}/A)}{\partial \sigma^*} \right]_T \quad (6)$$

Strain rate can be expressed as

$$\dot{\epsilon} = \rho b \bar{v} \quad (7)$$

where ρ is the density of mobile dislocations, b their Burgers vector and \bar{v} the average dislocation velocity.

Preceding page blank

By definition

$$\bar{v} = \sigma^* m^* \quad (8)$$

From (6), (7) and (8)

$$V^* = kT \frac{\partial \left[m^* \ln \left(\frac{\rho b}{A} \sigma^* \right) \right]}{\partial \sigma^*} \quad (9)$$

Or

$$V^* = kT \frac{m^*}{\sigma^*} \quad (10)$$

This can also be expressed as

$$V^* = kT m^* / \tau^* \quad (11)$$

An example calculation follows:

$$k = 1.38 \times 10^{-23} \text{ joules/}^\circ\text{K} \quad (12)$$

From (11) and (12)

$$V^* = \frac{1.38 \times 10^{-23} \text{ joules}}{^\circ\text{K}} \left| \frac{295^\circ\text{K}}{0.7376 \text{ Ft-Lb}} \right| \left| \frac{12 \text{ in}}{\text{Ft}} \right| \left| \frac{16.4 \text{ cm}^3}{\text{in}^3} \right| \left| \frac{10^{24} \text{ }^\circ\text{K}^3}{\text{cm}^3} \right| \left| \frac{\bar{v}^3}{20.45 \text{ }^\circ\text{K}^3} \right| \left(\frac{m^*}{\tau^*} \right)$$

Or

$$V^* = 28,897.0688 \frac{m^*}{\tau^*} \bar{v}^3 \left(\frac{\text{Lb}}{\text{In}} \right) \text{ at } 295^\circ\text{K} \quad (13)$$

The value for \bar{v}^3 was obtained from the bcc relationship

$$\bar{v} = \frac{\sqrt{3}}{2} a_0 \quad (14)$$

Using the lattice parameter for tungsten

$$a_0 = 3.1585 \text{ }^\circ\text{A} \quad (15)$$

From (14) and (15)

$$\bar{v} = 2.73 \text{ \AA}$$

Or

$$\bar{v}^3 = 20.45 \text{ \AA}^3 \quad (16)$$

For the <100> unalloyed tungsten sample, then

$$v^* = \frac{28,897.0688 \bar{v}^3 \text{ Lb}}{\text{In}^2} \quad \bigg| \quad \frac{9.1}{\text{In}^2} \quad \bigg| \quad \frac{\text{In}^2}{3,845 \text{ Lb}}$$

$v^* = 68.4 \bar{v}^3$

(17)

REFERENCES

1. G. A. Geach and J. R. Hughes, "The Alloys of Rhenium with Molybdenum or with Tungsten and Having Good High Temperature Properties," Plansee Proc. (1955), p 245, Pergamon Press Ltd., London, 1956.
2. R. I. Jaffee, C. T. Sims and J. J. Harwood, "The Effect of Rhenium on the Fabricability and Ductility of Molybdenum and Tungsten," Plansee Proc. (1958), p 380, Pergamon Press Ltd., London, 1959.
3. E. M. Savitskii, M. A. Tylkina and K. B. Povarova, Zhnr. Neorg. Khim, 4, 424, 1959.
4. W. D. Klopp, F. C. Holden and R. I. Jaffee, "Further Studies on Rhenium Alloying Effects in Molybdenum, Tungsten and Chromium," Technical Report on Contract No. Nonr-1512(00), Battelle Memorial Inst., Columbus, Ohio, July 12, 1960.
5. A. Gilbert and B. C. Allen, "The Notch-Impact Behaviour of Chromium and a Chromium-35 At.-% Rhenium Alloy," J. Inst. Metals, 93, 529, 1965.
6. A. Gilbert, "A Fractographic Study of Tungsten and Dilute Tungsten-Rhenium Alloys," J. Less-Common Metals, 10 (5) 328, 1966.
7. A. Gilbert, M. J. Klein, J. W. Edington, "Investigation of Mechanical Properties of Chromium, Chromium-Rhenium, and Derived Alloys," Battelle Memorial Inst. (NASA CR-81225) Aug 31, 1966.
8. P. L. Raffo, "Yielding and Fracture in Tungsten and Tungsten-Rhenium Alloys," J. Less-Common Metals, 17, 133, 1969.
9. B. C. Allen, "Effect of Rhenium on the Interface Energies of Chromium, Molybdenum, and Tungsten," Trans. AIME, 236 (6) 903, 1966.

Preceding page blank

10. B. C. Allen, "Mechanisms of Grain Boundary Grooving in Chromium, Molybdenum, Tungsten, Cr-35Re, Mo-33Re, and W-25Re," *Trans. AIME*, 236 (6) 915, 1966.
11. J. G. Booth, R. I. Jaffee and E. I. Salkovitz, "The Mechanisms of the Rhenium-Alloying Effect in Group VIA Metals," *Plansee Proc. 1964 - Metals for the Space Age*, F. Benesovsky, ed., p 547, Springer-Verlag, New York, 1965.
12. Mark J. Klein, "Precipitation of Nitrogen from Solid Solution in Cr-35 pct Re," *Trans. AIME*, 236 (7) 1044, 1966.
13. Mark J. Klein, "Nitrogen-Induced Internal Friction in Cr-35 Pct Re," *Trans. AIME*, 233 (11) 1943, 1965.
14. D. T. Novick and E. S. Machlin, "A Field Ion Microscope Investigation of the Effect of Rhenium on the Lattice Solid Solubility of Oxygen in Tungsten," *Trans ASM*, 61, 777, 1968.
15. A. Gilbert, C. N. Reid, G. T. Hahn, "Tensile Properties of Chromium-Rhenium Alloys." *High Temperature Refractory Metals*, Vol. 34, p 194, W. A. Krivsky, R. W. Fountain, J. Maltz, and L. Richardson, eds., Gordon and Breach, Science Publ, Inc., 1966.
16. I. G. Booth, "Effect of Electron Concentration on Mechanical Properties of Alloys of Refractory Metals," *Annual Topical Report on Contract No. Nonr-3589(00)*, Battelle Memorial Inst., Columbus, Ohio, Oct. 17, 1963.
17. W. D. Klopp, "Review of Ductilizing of Group VIA Elements by Rhenium and Other Solutes," *NASA TN D-4955*, Dec 1968.
18. J. R. Stephens and W. D. Klopp, "Enhanced Ductility in Binary Chromium Alloys," *Trans AIME*, 242, 1837, 1968.
19. E. Votava, "Polygonization and Stacking Faults in Molybdenum-Rhenium Alloys," *Acta Met*, 10, 745, 1962.
20. E. Votava and A. W. Sleeswyk, "Emissary Dislocations in a Molybdenum-Rhenium Alloy," *Acta Met*, 10, 965, 1962.

21. A. W. Sleeswyk, "Emissary Dislocations: Theory and Experiments on the Propagation of Deformation Twins in α -Iron," Acta Met, 10, 705, 1962.
22. D. Hull, "The Initiation of Slip at the Tip of a Deformation Twin in α -Iron," Acta Met, 9, 909, 1961.
23. D. Hull, "Deformation Twinning," p 121, Gordon and Breach, New York, 1964.
24. J. Lavesseur, "Geometric Study of Twin Intersections and the Interaction Twin-Slip in α -Iron," Mat. Sci. Eng., 4, 343, 1969.
25. C. T. Sims and R. I. Jaffee, "Properties of Refractory Alloys Containing Rhenium," Trans. ASM, 52, 929, 1959.
26. P. L. Raffo and T. E. Mitchell, "Yielding, Work Hardening, and Cleavage in Tantalum-Rhenium Alloy Single Crystals," Trans AIME, 242, 907, 1968.
27. E. N. Aqua and C. N. J. Wagner, "X-Ray Diffraction Study of Deformation of Nb(Cb)-Re Alloys," Trans AIME, 236, 1085, 1966.
28. T. E. Mitchell and P. L. Raffo, "Mechanical Properties of Some Tantalum Alloys," Can. J. of Phys., 45, 1047, 1967.
29. J. R. Stephens, "Dislocation Structures in Slightly Strained Tungsten, Tungsten-Rhenium, and Tungsten-Tantalum Alloys," Trans AIME, 242, 634, 1968.
30. J. R. Stephens, "Dislocation Structures in Single-Crystal Tungsten and Tungsten Alloys," Met. Trans, 1, 1293, 1970.
31. J. R. Stephens and W. R. Witzke, "Alloy Softening in Group VIA Metals Alloyed with Rhenium," J. Less-Common Metals, 23, 325, 1971.
32. J. R. Stephens and W. R. Witzke, "Alloy Hardening and Softening in Binary Molybdenum Alloys as Related to Electron Concentration," NASA TN D-6810, May 1972.

33. R. A. Foxall and C. D. Statham, "Dislocation Arrangements in Deformed Single Crystals of Niobium-Molybdenum Alloys and Niobium-9 At% Rhenium," *Acta Met*, 18, 1147, 1970.
34. T. Tanaka and S. Watanabe, "The Temperature Dependence of the Yield Stress and Solid Solution Softening in Fe-Ni and Fe-Si Alloys," *Acta Met*, 19, 991, 1971.
35. W. A. Spitzig and W. C. Leslie, "Solid Solution Softening and Thermally Activated Flow in Alloys of Fe with 3 at. % Co, Ni or Si," *Acta Met*, 19, 1143, 1971.
36. W. C. Leslie, "Iron and Its Dilute Substitutional Solid Solutions," *Met Trans*, 3, 5, 1972.
37. W. C. Leslie, R. J. Sober, S. G. Babcock, and S. J. Green, "Plastic Flow in Binary Substitutional Alloys of bcc Iron- Effects of Strain Rate, Temperature and Alloy Content," *Trans ASM*, 62, 690, 1969.
38. Prakash D. Parikh, "Some Aspects of the Mechanical Behavior of Body-Centered Cubic Transition Metals," Ph. D. Dissertation, Drexel University, June 1972.
39. R. P. Gamble, M. S. Thesis, Cornell University, 1969.
40. C. D. Statham and J. W. Christian, "Solution Hardening and Softening in Niobium-Molybdenum and Niobium-Rhenium Alloys," *Scripta Met*, 5, 399, 1971.
41. G. C. Das and R. J. Arsenault, "Non-Monatomic Strengthening in bcc Solid Solutions," *Scripta Met*, 2, 495, 1968.
42. M. F. Amaleau, R. Gibala and T. E. Mitchell, "Dislocation Relaxations in Niobium Single Crystals," *Scripta Met* (in press).
43. K. V. Ravi and R. Gibala, "The Strength of Niobium-Oxygen Solid Solutions," *Acta Met*, 18, 623, 1970.
44. K. V. Ravi and R. Gibala, "Low Temperature Strengthening in Niobium-Hydrogen Single Crystals," *Met. Trans*, 2, 1219, 1971.

45. K. V. Ravi and R. Gibala, "Dislocation Dynamics in Niobium-Oxygen Solid Solutions," to be published in Met Trans.
46. A. A. Sagues and R. Gibala, "Substitutional-Interstitial Solute Interactions in Ta-Re-N Solid Solutions," Scripta Met, 5, 689, 1971.
47. M. G. Ulitchny, A. A. Sagues and R. Gibala, "Alloy Softening in Niobium and Tantalum-Base Solid Solutions," Presented at Discussion Meeting on Defects in Refractory Metals, MOL, Belgium, 20-22 Sep 1971.
48. C. D. Statham, Ph. D. Dissertation, Oxford University, 1969.
49. D. R. Hay, Ph. D. Thesis, Cornell University, 1966.
50. R. W. Powers and Margaret V. Doyle, "Diffusion of Interstitial Solutes in the Group V Transition Metals," JAP, 30, p 514, 1959.
51. R. W. Powers and Margaret V. Doyle, "The Diffusion of Carbon and Oxygen in Vanadium," Acta Met, 6, p 643, 1958.
52. R. W. Powers, "Internal Friction in Oxygen - Vanadium and Nitrogen - Vanadium Solid Solutions," Acta Met, 2, p 604, 1954.
53. R. W. Powers and M. V. Doyle, "The Association of Oxygen Atoms in Interstitial Solid Solution in Tantalum," Trans AIME 215, p 655, 1959.
54. R. W. Powers and Margaret V. Doyle, "Carbon Tantalum Internal Friction Peak," J. Appl. Phys. 28, p 255, 1957.
55. R. W. Powers and Margaret V. Doyle, "Internal Friction in Solid Solutions of Tantalum," Acta Met, 4, p 233, 1956.
56. D. J. van Ooijen and A. S. van der Groot, "The Internal Friction of Cold-Worked Niobium and Tantalum Containing Oxygen and Nitrogen," Acta Met, 14, p 1008, 1966.
57. Patricia M. Bunn, D. G. Cummings and H. W. Leavenworth, Jr., "The Effects of Zirconium on Internal Friction in Columbium," J. Appl. Phys. 33, p 3009, 1962.

58. Mark J. Klein and A. H. Clauer, "Nitrogen - Induced Internal Friction in Chromium," *Trans AIME*, 233, p 1771, 1965.
59. Randolph H. Schnitzel, "Damping Measurements on Single-Crystal Molybdenum," *Trans AIME*, 230, p 609, 1964.
60. R. H. Schnitzel, "Internal Friction of Tungsten Single Crystals," *Trans AIME*, 233, p 186, 1965.
61. A. Joshi and D. F. Stein, "Intergranular Brittleness in Tungsten Using Auger Spectroscopy," *Met. Trans.*, 1, p 2543, 1970.
62. F. Ostermann and F. Bollenrath, "On the Precipitation Behavior of Niobium Alloy D-43 (Nb-10W-1Zr-0.1C), *Plansee Proceedings 1966*), p 317, Pergamon Press, Ltd., London, 1967.
63. P. W. Palmberg, G. K. Bohn and J. C. Tracy, "High Sensitivity Auger Electron Spectroscopy," *Appl. Phys. Letter* 15, 254 (1969).
64. T. W. Haas, J. T. Grant and G. J. Dooley, "Auger Electron Spectroscopy of Transition Metals," *Phys. Rev. B* 1, 1449 (1970).
65. P. W. Palmberg, "Optimization of Auger Electron Spectroscopy in LEED Systems," *Appl. Phys. Letter* 13, 183 (1968).
66. P. W. Palmberg and T. N. Rhodin, "Auger Electron Spectroscopy of F. C. C. Metal Surfaces," *J. Appl. Phys.* 39, 2425 (1968).
67. P. W. Palmberg, "Secondary Emission Studies on Ge and Na-covered Ge," *J. Appl. Phys.* 38, 2137 (1967).
68. R. E. Weber and W. T. Peria, "Use of LEED Apparatus for the Detection and Identification of Surface Contaminants," *J. Appl. Phys.* 38, 4355 (1967).
69. L. A. Harris, "Analysis of Materials by Electron-excited Auger Electrons," *J. Appl. Phys.* 39, 1419 (1968); 39, 1428 (1968).

70. J. J. Lander, "Auger Peaks in the Energy Spectra of Secondary Electrons from Various Materials," *Phys. Rev.* 91, 1382 (1953).
71. L. N. Tharp and E. J. Scheibner, "Energy Spectra of Inelastically Scattered Electrons and LEED Studies of W," *J. Appl. Phys.* 38, 3320 (1967).
72. E. J. Scheibner and L. N. Tharp, "Inelastic Scattering of Low-energy Electrons from Surfaces," *Surface Sci.* 8, 247 (1967).
73. H. C. Raghuram, R. W. Armstrong, and R. E. Reed, "A Note on Compression Testing of High-Purity Niobium Single Crystals," *Scripta Met.* 3, 199, 1969.
74. J. T. Michalak, "The Influence of Temperature on the Development of Long-Range Internal Stress During the Plastic Deformation of High-Purity Iron," *Acta Met.* 13, 213, 1965.
75. H. G. Sell, D. F. Stein et al., "The Identification of Bubble-Forming Impurities in Doped Tungsten," *J. Inst. of Metals* 100, 275 (1972).
76. Chester W. Dawson, "Effect of a Temperature Gradient on Bubble Growth in Tungsten," *Met. Trans.* 3, 3103 (1972).
77. J. L. Walter, "Growth of Preferred Orientations of Large Elongated Grains in Doped Tungsten Sheet," *Trans AIME*, 239, 272 (1967).
78. R. C. Koo, "Evidence for Voids in Annealed Doped Tungsten," *Trans AIME*, 239, 1996 (1967).
79. D. M. Moon and R. C. Koo, "Mechanism and Kinetics of Bubble Formation in Doped Tungsten," *Met. Trans.* 2, 2115 (1971).
80. G. Das, "Direct Observation of Voids in Doped Tungsten By Scanning Electron Microscopy," *Met. Trans.* 2, 3239 (1971).

81. D. B. Snow, "Dopant Observations in Thin Foils of Annealed Tungsten Wire," *Met. Trans.* 3, 2553 (1972).
82. J. Brett and S. Friedman, "High Temperature Porosity in Tungsten," *Met. Trans.* 3, 769 (1972).
83. R. Cheney, personal communication
84. W. S. Owen and M. J. Roberts, "Dynamic Aging Effects in Iron-Nickel-Carbon Martensite," *Dislocation Dynamics*, McGraw Hill, N. Y., p 357, 1968.
85. J. E. Dorn and A. K. Mukherjee, "A Modified Peierls Model for Thermally Activated Deformation in bcc Metals," *Trans AIME*, 245, 1493, 1969.
86. K. C. Li, in: *Rare Metals Handbook*, Ed. C. A. Hampel (Reinhold, New York, 1961) p 596.
87. G. J. Dooley III and T. W. Haas, "Auger Electron Spectroscopy: Metallurgical Applications," *J. Metals* 22, 17 (1970).
88. H. L. Marcus and P. W. Palmberg, "Auger Fracture Surface Analysis of a Temper Embrittled 3340 Steel," *Trans. Met. Soc. AIME* 245, 1664 (1969).
89. G. J. Dooley III and T. W. Haas, "Behavior of Refractory Metal Surfaces in Ultrahigh Vacuum as Observed by Low-energy Electron Diffraction (LEED) and Auger Electron Spectroscopy," *J. Vac. Sci. Technol.* 7, 92 (1970).
90. G. J. Dooley III, "Surface Segregation Studies in Alloys Using Auger Electron Spectroscopy," *J. Vac. Sci. Technol.* 9, 145 (1972).
91. A. Joshi and D. F. Stein, "Intergranular Brittleness Studies in Tungsten Using Auger Electron Spectroscopy," *Met. Trans.* 1, 2543 (1970).
92. S. Thomas and T. W. Haas, "Quantitative AES and LEED Study of Alkali Metal Overlays on W(100)," *J. Vac. Sci. Technol.* 10, 218 (1973).

93. S. Thomas and T. W. Haas, "LEED/Auger Spectroscopy Study of the Adsorption of Alkali Metals on Mo(100)," J. Vac. Sci. Technol. 9, 840 (1972).
94. F. Meyer and J. J. Vrakking, "Quantitative Aspects of Auger Electron Spectroscopy," Surface Sci. 33, 271 (1972).
95. T. W. Haas, J. T. Grant and G. J. Dooley, "Chemical Effects in Auger Electron Spectroscopy," J. Appl. Phys. 43, 1853 (1972).
96. W. D. Klopp and W. R. Witzke, "Mechanical Properties of Electron-Beam Melted Molybdenum and Dilute Molybdenum-Rhenium Alloys," NASA TN X-2576, June 1972.
97. E. M. Savitskii and M. A. Tylkina, "Investigations into High Temperature Alloys," Rhenium and Its Alloys, Izdatel'stvo Akad. Nauk S. S. S. R. Moscow, 1956.
98. E. M. Savitskii, M. A. Tylkina and K. B. Povarova, Rhenium Alloys, Nauka Publ. House, Moscow (1965), Trans. JPRS No. 34, p 566, U. S. Dept. Commerce, 15 March, 1966.
99. E. M. Savitskii, M. A. Tylkina and L. L. Shishkina, "Equilibrium Diagram of the System Tungsten-Rhenium and Properties of the Alloys," Izvest. Akad. Nauk S. S. S. R., Otdel, Khim, Nauk, 99, 1959.
100. M. A. Tylkina and E. M. Savitskii, "Contemporary State and Prospects for the Development of Operations Based on Rhenium Alloys," Third All-Union Conference on the Problem of Rhenium, Moscow, Oct 68, E. M. Savitskii, Ed., 5, 1970.
101. R. I. Jaffee, D. J. Maykuth and R. W. Douglass, "Rhenium and Refractory Platinum Group Metals," Refractory Metals and Alloys, Met. Soc. Conference, 1961, Vol. II, Inter-science Publication, p 383, 1961.
102. D. A. Robins, "An Interpretation of Some of the Properties of the Transition Metals and Their Alloys," J. Less-Common Metals, 1, 396, 1959.

103. Dudley A. Robins, "Discussion to 'Properties of Refractory Alloys Containing Rhenium'," by Chester T. Sims and Robert I. Jaffee, Trans. ASM, 52, 943, 1960.
104. Yu V. Mil'man, A. P. Rachiek and V. I. Trefilov, "Investigation of the Mechanism of Deformation and Brittle Failure of Transition-Metal Alloys on a VIA-Group Base," SOURCE: AN UkrSSR. Institut metallofiziki. Sbornik nauchnykh trudov, no. 20, 1964. Voprosy fiziki metallov i metallovedeniya (Problems in the physics of metals and physical metallurgy), 3-24.
105. D. L. Davidson and F. R. Brotzen, "Plastic Deformation of Molybdenum-Rhenium Alloy Crystals," Acta Met., 18, 463, 1970.
106. A. Lawley and R. Maddin, "Tensile Behavior of Zone-Melted Molybdenum-Rhenium Single Crystals," Trans. AIME, 224, 573, 1962.
107. E. N. Aqua and C. N. J. Wagner, "Faulting in Cold Worked Ta-10%Re and W-20%Re," Trans. ASM, 59, 367, 1966.
108. D. L. Davidson and F. R. Brotzen, "Asymmetric Mechanical Properties of Molybdenum-Rhenium Alloy Single Crystals," Scripta Met. 5, 303, 1971.
109. D. L. Davidson and F. R. Brotzen, "Elastic Constants of Molybdenum-Rich Rhenium Alloys in the Temperature Range -190°C to +100°C," J. Appl. Phys., 39, 5768, 1968.
110. J. G. Booth, "Antiferromagnetic-Weak-Ferromagnetic Behavior in Aged Chromium-Rhodium Alloys," J. Appl. Phys., 37, 1332, 1966.
111. J. G. Booth, "Magnetic Properties of Cr Alloys Containing Dilute Concentrations of Co, Ni, and Fe," J. Phys. Chem. Solids, 27, 1639, 1966.
112. B. A. Gusynin, M. A. Tylkina and E. M. Savitskii, "Elastic Characterization of Rhenium Alloys," Third All-Union Conference on the Problem of Rhenium, Moscow, Oct 68, E. M. Savitskii, ed., 115, 1970.

113. K. B. Povarova, V. M. Amosov, M. A. Tylkina and E. M. Savitskii, "High-Temperature Properties of Tungsten-Molybdenum-Rhenium System Alloys," Third All-Union Conference on the Problem of Rhenium, Moscow, Oct 68, E. M. Savitskii, ed., 85, 1970.
114. Mark J. Klein and A. H. Clauer, "Influence of Interstitial Solutes on Elasticity and Damping of Chromium Near Its Neel Temperature," J. Applied Physics, 32 (12) 3566, 1964.
115. Mark J. Klein, A. H. Clauer and R. E. Maringer, "Influence of Thermal and Mechanical History on Young's Modulus and Damping Anomalies Near 40°C in Chromium," J. Applied Physics, 35 (6) 1994, 1964.
116. Mark J. Klein and A. H. Clauer, "Nitrogen-Induced Internal Friction in Chromium," Trans AIME, 233 (9) 1771, 1965.
117. Mark J. Klein, "A Study of Nitrogen in a Chromium-Yttrium Alloy," Trans AIME, 236 (12) 1679, 1966.
118. Mark J. Klein, "Diffusion Coefficient of Nitrogen in Chromium," J. Applied Physics, 38 (1) 167, 1967.
119. A. Gilbert, C. N. Reid and G. T. Hahn, "Observations on the Fracture of Chromium," J. Iron Steel Inst., 202, 677, 1964.
120. A. Gilbert, J. L. Ratliff and W. R. Warke, "A Fractographic Study of a Thoriated Tungsten-Rhenium Alloys," Trans ASM, 58 (2) 142, 1965.
121. A. R. Rosenfield, "Deformation Twinning of Polycrystalline Chromium-Rhenium Alloys," J. Less-Common Metals, 7, 235, 1964.
122. S. Mahajan, "Twin-Slip and Twin-Twin Interactions in Mo-35 at% Re Alloy," Phil Mag, 23, 781, 1971.
123. S. Mahajan, "Evaluation of Slip Patterns Observed in Association with Deformation Twins in Mo-35 at% Re Alloy," J. Phys. F: Metal Phys., 2, 19, 1972.

124. C. N. Reid, G. T. Hahn and A. Gilbert, "The Speed of Twin Growth in Mo-35Re," Air Force Conference on Deformation of Twinning, Gordon and Breach, New York, 1964.
125. C. N. Reid, A. Gilbert and G. T. Hahn, "Dislocation and Deformation Modes in Chromium Single Crystals," Trans AIME, 239 (4) 467, 1967.
126. B. C. Allen, "The Surface Tension of Liquid Chromium and Manganese," Trans AIME, 230 (10) 1357, 1964.
127. I. M. Saakyan, V. I. Sarraf, N. M. Fonshtein and R. I. Entin, "Effect of Rhenium on the Brittle Fracture Tendencies of Refractory Metals," Fiz. Khim. Obrab. Mater., 2, 79, 1968.
128. V. I. Sarraf, N. M. Fonshtein, R. I. Entin, "Effect of Rhenium on the Brittle Fracture Tendency of Tungsten," Third All-Union Conference on the Problem of Rhenium, Moscow, Oct 68, E. M. Savitskii, ed., 112, 1970.
129. A. Gilbert and M. J. Klein, "The Effect of Cooling Rate on the Ductile-Brittle Bend-Transition Temperature of Chromium Wire," Acta Met, 14 (4) 541, 1966.
130. D. J. Maykuth, F. C. Holden and R. I. Jaffee, "The Workability and Mechanical Properties of Tungsten- and Molybdenum-Base Alloys Containing Rhenium," Rhenium, P 114, Elsevier Publ. Co., Amsterdam, 1961.
131. B. C. Allen, D. J. Maykuth and R. I. Jaffee, "The Effect of Impurities and Structure on the Tensile Transition Temperature of Chromium," Trans AIME, 227 (6) 724, 1963.
132. G. T. Hahn, A. Gilbert and R. I. Jaffee, "The Effects of Solutes on the Ductile-to-Brittle Transition in Refractory Metals," Refractory Metals and Alloys II, p 23, Interscience Publishers, 1963.
133. J. L. Ratliff, D. J. Maykuth, H. R. Ogden and R. I. Jaffee, "Tungsten Sheet Alloys with Improved Low-temperature Ductility," Trans AIME, 230, 490, 1964.

134. V.A. Ermishkin, Z.G. Fridmann, M.A. Tylkina and E. M. Savitskii, "Heating-Resisting Properties of a VR-27VP [W-Re] Alloy," Third All-Union Conference on the Problem of Rhenium, Moscow, Oct 68, E.M. Savitskii, ed., 76, 1970.
135. E.M. Savitskii, M.A. Tylkina, S.I. Ipatova and E.I. Pavolova, "The Properties of Tungsten-Rhenium Alloys," Metalloved. i Termichesk. Obrabotka Metal., No. 9, 20-5, 1960.
136. L. L. Zhdanova, M.A. Tylkina and E.M. Savitskii, "Recrystallization and Some Properties of VR-27VP-[W-Re] Alloy," Third All-Union Conference on the Problem of Rhenium, Moscow, Oct 68, E.M. Savitskii, ed., 90, 1970.
137. A. Gilbert, B.C. Allen and C.N. Reid, "An Investigation of Mechanical Properties of Chromium, Chromium-Rhenium, and Derived Alloys," Contractor Report, NASw-101, Battelle Memorial Inst., Columbus, Ohio, NASA Cr-118, Nov 1964.
138. B. C. Allen and R.I. Jaffee, "The Hardness Behavior of Chromium Alloyed with Group IV A to VIII Transition Metals," Trans. ASM, 56, 387, 1963.
139. R.I. Jaffee and G. T. Hahn, "Structural Considerations in Developing Group VIA Alloys," Proceedings of Conference, The Relations Between the Structure and the Mechanical Properties of Metals, p 707, Her Majesty's Stationery Office, London, 1963.
140. C. T. Sims, C.M. Craighead and R.I. Jaffee, "Physical and Mechanical Properties of Rhenium," Trans AIME, 203, 168, 1955.
141. C. T. Sims and R. I. Jaffee, "Further Studies of the Properties of Rhenium Metal," Trans AIME, 206, 913, 1956.
142. C. T. Sims, Gordon B. Gaines and R.I. Jaffee, "Refractory-Metal Thermocouples Containing Rhenium," Review of Scientific Instruments, 112, 1959.

143. E. E. Underwood, "Effect of Electron Concentration on Mechanical Properties of Alloys of Refractory Metals," Annual Topical Rept, Battelle Memorial Inst., Contract Nonr-3589(00), Dec 28, 1962.
144. Ervin E. Underwood, "A Review of Superplasticity and Related Phenomena, J. Metals, 14, 914, 1962.
145. R. J. Arsenault, "Solid Solution Strengthening and Weakening of bcc Solid Solutions," Acta Met, 17, 1291, 1969.
146. D. F. Hasson and R. J. Arsenault, "Solid Solution Weakening of bcc Solid Solutions," Proceedings of the Second International Conference on the Strength of Metals and Alloys, Vol. 1, ASM, 267, 1970.
147. Ram B. Roy, "Comments on 'Solid Solution Softening in bcc Alloys'," Scripta Met, 3, 531, 1969.
148. Ram B. Roy, "Orientation and Stress-Polarity Dependence of Critical Resolved Shear Stress (CRSS) in bcc Metal Crystals," Scripta Met, 3, 721, 1969.
149. E. Pink and R. J. Arsenault, "Solid Solution Strengthening and Weakening of Vanadium-Titanium Alloys," to be published in J. of Materials Science.
150. George H. Keith, "Interactions of Titanium and Molybdenum Additions with Interstitial Impurities in Vanadium," Rept. RI-7262, Bureau of Mines, May 1969.
151. B. Harris, "Solution Hardening in Niobium," Phys. Stat. Sol., 18, 715, 1966.
152. M. Garfinkle, W. R. Witzke and W. D. Klopp, "Superplasticity in Tungsten-Rhenium Alloys," Trans AIME, 245, 303, 1969.
153. W. D. Klopp, W. R. Witzke and P. L. Raffo, "Mechanical Properties of Dilute Tungsten-Rhenium Alloys," NASA TN D-3483, Sept 1966.

154. W. D. Klopp and W. R. Witzke, "Mechanical Properties of Arc-Melted Tungsten-Rhenium-Hafnium-Carbon Alloys," NASA TN D-5348, July 1969.
155. W. D. Klopp and W. R. Witzke, "Mechanical Properties of a Tungsten -23.4-Percent-Rhenium-0.27-Percent-Hafnium-Carbon Alloy," NASA TN D-6308, Apr 1971.
156. P. L. Raffo and W. D. Klopp, "Mechanical Properties of Arc-Melted and Electron-Beam Melted Tungsten Base Alloys," NASA TN D-2561, Jan 1965.
157. W. H. Lenz and R. E. Riley, "Ductility Studies in Sintered Tungsten-Molybdenum-Rhenium Alloys," Los Alamos Scientific Lab, N. Mex, LA-4136, 20 Feb 1969.
158. W. H. Lenz and R. E. Riley, "The Rhenium Effect in Sintered Tungsten-Molybdenum-Base Alloys," Los Alamos Scientific Lab, N. Mex, LA-4173-MS, 15 Apr 1969.
159. C. S. Wukusick, "The Rhenium Ductilizing Effect," General Electric, Cincinnati, Ohio, GE-TM 65-9-11, Oct 1965.
160. J. W. Pugh, L. H. Amra, D. T. Hurd, "Properties of Tungsten-Rhenium Lamp Wire," Trans ASM, 55, 451, 1962.
161. M. Garfinkle, "Room Temperature Tensile Behavior of <100> Oriented Tungsten Single Crystals with Rhenium in Dilute Solid Solution," NASA TN D-3190, Jan 1966.
162. Peter L. Raffo, "Yielding and Fracture in Tungsten and Tungsten-Rhenium Alloys," J. of Less-Common Metals, 17, 133, 1969.
163. B. W. Christ, R. P. Gamble and G. V. Smith, "On the Distinction Between Alloy Softening Due to Nitrogen and Nickel in Dilute Lattice Solutions in Iron," Scripta Met, 3, 521, 1969.
164. B. W. Christ and G. V. Smith, "Effects of Nitrogen in Lattice Solution on the Yielding and Flow of Zone-Refined Iron Polycrystals Between 128° and 300°K," Met Trans, 1, 827, 1970.

165. W. R. Clark, "Alloy Softening in the Iron-Germanium System," M.S. Thesis, Dartmouth College, June 1971.
166. H. H. Kranzlein, M. J. Burton and G. V. Smith, "Solid Solution Strengthening in Iron-Nickel and Iron-Platinum Alloys," Trans AIME, 233, 64, 1965.
167. B. W. Christ and G. V. Smith, "Effects of Impurities on Yield and Flow Strength of Zone Refined Iron," Mem. Scient. Revue, 65, 207, 1968.
168. W. C. Leslie and R. J. Sober, "The Strength of Ferrite and of Martensite as Functions of Composition, Temperature and Strain Rate," Trans ASM, 60, 459, 1967.
169. Y. Nakada and A. S. Key, "Solid Solution Strengthening in Fe-N Single Crystals," Acta Met, 16, 903, 1968.
170. N. Brown and R. A. Ekvell, "Temperature Dependence of the Yield Points in Iron," Acta Met, 10, 1101, 1962.
171. W. Jolley, "Influence of a 3.28 pct Nickel Addition on the Yield and Fracture Behavior of Alpha Iron," Trans AIME, 242, 306, 1968.
172. B. W. Christ, "On the Mechanism of Interstitial-Impurity-Induced Cross-Slip in Iron Deformed Near 175°K," Acta Met, 17, 1317, 1969.
173. R. J. Arsenault, "Solid Solution Strengthening and Weakening of bcc Solid Solutions," Acta Met, 17, 1291, 1969.
174. J. W. Christian, "Plastic Deformation of bcc Metals," Proc. 2nd Int. Conf. Strength of Metals and Alloys, Vol. I, p 29, ASM, Cleveland, Ohio, 1970.
175. R. G. Wolfson and W. R. Clark, "Solid-Solution Softening in Nonmetallic Crystals," Dartmouth College, Hanover, N. H., Presented at TMS AIME, Detroit, 19 Oct, 1971.
176. A. Urakami, Ph. D. Dissertation, Northwestern University, 1970.

177. T. Takeuchi, "Theory of Low Temperature Work-Hardening of Body-Centered Cubic Metals," J. Phys. Soc. Japan, 27, 436, 1969.
178. V. Vitek and F. Kroupa, "Dislocation Theory of Slip Geometry and Temperature Dependence of Flow Stress in bcc Metals," Phys. Stat. Sol. 18, 703, 1966.
179. F. Kroupa and V. Vitek, "On the Contribution of 110 Planes to the Slip Asymmetry in bcc Metals," Phys. Stat. Sol., 36, K143, 1969.
180. F.R.N. Nabarro and T.R. Duncan, "Dissociated Dislocations and the Schmidt Law of Resolved Shear Stress in bcc Metals," Can. J. Phys., 45, 939, 1967.
181. J. Friedel, Dislocations, p 161 ff., Pergamon Press, New York, 1964.
182. F. Kroupa and V. Vitek, "Slip and the Conception of Splitting of Dislocations in bcc Metals," Can. J. Phys., 45, 945, 1967.
183. M. S. Duesbery and P. B. Hirsch, Dislocation Dynamics, Rosenfield et al., eds., p 57, McGraw-Hill, New York, 1968.
184. J.R. Low, Jr. and R.W. Guard, "The Dislocation Structure of Slip Bands in Iron," Acta Met, 7, 171, 1959.
185. A.W. Cochardt, G. Schoek and H. Widersich, "Interaction Between Dislocations and Interstitial Atoms in Body-Centered Cubic Metals," Acta Met, 3, 533, 1955.
186. R. L. Fleischer, "Rapid Solution Hardening, Dislocation Mobility, and the Flow Stress of Crystals," J. Appl. Phys., 33, 3504, 1962.
187. P. M. Kelly, "The Low Temperature Strength of bcc Metals," Scripta Met, 3, 149, 1969.
188. K. V. Ravi and R. Gibala, "The Strength and Alloy Softening of bcc Metals," Scripta Met, 3, 547, 1969.
189. R. L. Smialek, G. L. Webb and T. E. Mitchell, "Solid Solution Softening in bcc Metal Alloys," Scripta Met, 4, 33, 1970.

190. B. W. Christ and G. V. Smith, "Yield and Flow Stress Increase in Pure Polycrystalline Iron During 600°C Treatment After Wet Hydrogen Purification," *Scripta Met*, 1, 123, 1967.
191. T. E. Mitchell, R. A. Foxall and F. B. Hirsch, "Work-Hardening in Niobium Single Crystals," *Phil. Mag.*, 8, 1895, 1963.
192. D. F. Stein, "The Effect of Orientation and Impurities on the Mechanical Properties of Molybdenum Single Crystals," *Can. J. Phys.*, 45, 1063, 1967.
193. R. L. Fleischer, "The Flow Stress of Body-Centered Cubic Metals: Inherent Lattice Hardening or Solution Hardening?" *Acta Met*, 15, 1513, 1967.
194. D. S. Kamenetskaya, I. B. Piletskaya and V. I. Shiryaev, "Mechanical Properties of High-Purity Iron," *Soviet Physics - Doklady* (in English translation) 15, 177, 1970.
195. W. A. Spitzig, "The Effects of Phosphorus on the Mechanical Properties of Low Carbon Iron," *Met Trans*, 3, 1183, 1972.
196. S. K. Lahiri and M. E. Fine, "Temperature Dependence of Yield Stress in Fe-1.67 At. Pct. Cu and Fe-0.5 At. Pct. Au," *Met Trans*, 1, 1495, 1970.
197. N. F. Mott and F. R. N. Nabarro, Rep. Conf. Internal Strain Solids, p 86, Bristol, 1940.
198. N. F. Mott and F. R. N. Nabarro, Rep. Conf. Strength Solids, p 1, Bristol, 1948.
199. N. F. Mott, Imperfections in Nearly Perfect Crystals, p 173, Wiley and Sons, New York, 1952.
200. G. Schoeck and A. Seeger, "The Flow Stress of Iron and Its Dependence on Impurities," *Acta Met*, 7, 469, 1959.
201. J. Friedel, Internal Stresses and Fatigue in Metals, p 244, Elsevier, 1959.

- 202. J. Friedel, Dislocations, p 379, Pergamon Press, New York, 1964.
- 203. R. L. Fleischer, "Solution Hardening by Tetragonal Distortions: Application to Irradiation Hardening in fcc Crystals," Acta. Met., 10, 835, 1962.
- 204. J. Friedel, Internal Stresses and Fatigue in Metals, p 242, Elsevier, 1959.
- 205. W. C. Leslie and R. J. Sober, "Yielding and Plastic Flow in a Polycrystalline "Interstitial-Free" Fe-0.15% Ti Alloy," Trans ASM, 60, 99, 1967.
- 206. H. D. Solomon, C. J. McMahon, Jr. and W. C. Leslie, "The Effect of Temperature on the Early Stages of Plastic Flow in Titanium-Scavenged Iron," Trans ASM, 62, 886, 1969.
- 207. Barry L. Mordike, "Low Temperature Deformation of Tantalum Base Alloys," Keynote Paper, Alloy Softening II Session, The Metallurgical Society Meeting, Detroit, Mich., 19 October, 1971.
- 208. A. A. Braithwaite, B. L. Mordike and K. D. Rogausch, "Solid Solution Hardening in Tantalum Alloys," Z. f. Metallkunde, 62, 595, 1971.

**Reproduced From
Best Available Copy**